THERMAL AND MECHANICAL ISOLATION OF OVENIZED MEMS RESONATOR

A DISSERTATION SUBMITTED TO THE
DEPARTMENT OF
MECHANICALENGINEERING
AND THE COMMITTEE ON GRADUATE STUDIES OF
STANFORD UNIVERSITY
IN PARTIAL FULFILLMENT OF
THE REQUIREMENTS FOR THE DEGREE OF
DOCTOR OF PHILOSOPHY

Chandra Mohan Jha

December 2008

I certify that I have read this dissertation and that, in my opinion, it is fully adequate, in scope and quality, as a dissertation for the degree of Doctor of Philosophy.

Prof. Thomas W. Kenny (Principal Advisor)
Department of Mechanical Engineering

I certify that I have read this dissertation and that, in my opinion, it is fully adequate in scope and quality as a dissertation for the degree of Doctor of Philosophy.

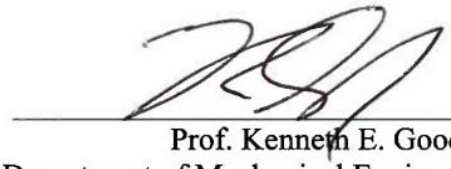

Prof. Kenneth E. Goodson
Department of Mechanical Engineering

I certify that I have read this dissertation and that, in my opinion, it is fully adequate in scope and quality as a dissertation for the degree of Doctor of Philosophy.

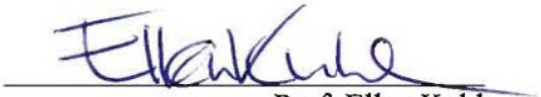

Prof. Ellen Kuhl
Department of Mechanical Engineering

Approved for the University Committee on Graduate Studies.

Abstract

Micromechanical silicon resonators are becoming an interesting and viable technology as a replacement for quartz crystals for timing and frequency reference applications. For high precision applications in industry and military, oven controlled resonators are used to compensate for the temperature dependence of resonator frequency. An oven controlled resonator requires a good temperature sensor and an efficient heater (oven). However, an external temperature sensor leads to thermal lag and the ovenization leads to power consumption.

This work presents a silicon micromechanical resonator based digital temperature sensing technique as well as an efficient local-thermal-isolation method. The micromechanical resonator based thermometry results into a lag-free temperature sensor for self temperature compensation suitable for high precision oven control of the resonator. The thermal isolation technique includes the design of an integrated heater with the micromechanical resonator such that the mechanical suspension, electrical heating and thermal isolation are provided in a single compact structure. This results in reducing the power consumption by more than 20x and the thermal time constant by more than 50x. Further reduction in power consumption requires analysis of the resonator structure to maintain its mechanical integrity. An improved thermally isolated design using topology optimization is described. The final design provides both the thermal isolation as well as the mechanical isolation with the overall reduction in power consumption of 40x. Furthermore, these methods are simple enough to implement it into any existing MEMS fabrication process.

To my sons Arvin and Tatsat

Acknowledgements

This thesis would not have been possible without the important contributions of so many people I came across during the course of my research work at Stanford. Their support and guidance not only helped me to complete my research but also transformed my life and made me who I am today. I would like to take this opportunity to acknowledge and thank them.

First and foremost, I would like to thank my advisor Prof. Tom Kenny for his invaluable support and guidance. He is a role model and a perfect mentor for me. I still remember my first meeting with him, after which I realized that I have to go a long way and I need a mentor like him. His constant support and encouragement made me capable enough to overcome many obstacles that came my way, even during tough times of my illness. I wish I can become a Professor and a Guide like him one day.

I would also like to thank my co-advisors Prof. Ken Goodson and Prof. Ellen Kuhl, who also accepted to become my reading committee members. Prof. Ken has been an inspiration for me to learn something new and in-depth in Heat Transfer. I was enrolled in two of his courses “Fundamentals of Heat Conduction” and “Micro Heat Transfer” both of which were among the most useful courses for me. Prof. Ellen has been an extremely supportive and encouraging Guide to me. Her advice and mentorship on “Topology Optimization” was very important and crucial for my research work. She has been an extremely motivating and collaborating advisor. I hope I can collaborate with her to do some path-breaking research sometime in future.

I would also like to thank Prof. Roger Howe and Dr. Rob Candler who have given guidance at different times of my graduate career at Stanford and took their precious

time to serve on my orals committee. I have also benefited from the guidance of John Vig, and I would like to thank him for that.

The most enriching experience of my research work was the collaboration and friendship of the members of the Kenny Research Group, past and present. I would like to thank all of them specially Dr. Matt Hopcroft who helped me throughout my research. As a senior Kenny Group member, he guided me with all aspects of the research lab when I joined the group. He helped me in the design, fabrication and the testing of the device. In fact, one of his resonator designs became very crucial for the completion of my research work. I had the great pleasure to work with extremely talented and brilliant people like Renata Melamud, Saurabh Chandorkar, Vipin Vitikkate, Kuanlin Chen, Jim Salvia, Hyungkyu Lee, Wes Smith, Violet Qu, Andrew Graham, Matt Messanna, Gaurav Bahl, Shasha Wang, Suhrid Bhat, Shingo Yoneoka, Jen Bower, Ginel Hill, Hyeun-su Kim, Kevin Lohner, Dan Soto, Yoonjin Won, Cathy, Mandy and Jim Cybulski, Evelyn Wang, and Holden Li, Michael Bartsch, Woo-tae Park, Matt Hopcroft, Bongsang Kim, Manu Agarwal, Harsh Mehta, and probably many more.

Finally, I would like to express my special regards for my family and friends for their continuous love and support. I wish to thank my parents, my brother, my sister and my wife Shikha for their unyielding love and support.

This work has been generously supported by DARPA HERMIT (ONR N66001-03-1-8942), Robert Bosch Corp. (RTC), AUDI, DRAPER LAB and the National Nanofabrication Users Network facilities funded by the NSF under award ECS-9731294, and NSF Instrumentation for Materials Research Program (DMR 9504099).

Table of Contents

List of Tables

List of Figures

List of Variables

k	Thermal conductivity, W m−1 K−1.
ε	Surface emissivity, $0 \leq \varepsilon \leq 1$.
σ	Stefan–Boltzmann constant,5.67×10−8Wm−2K−4.
ρ	Density, kg m−3.
C_p	Specific heat capacity at constant pressure, J kg−1 K−1.
R_e	Electrical resistance, Ω.
R_{th}	Thermal resistance, K W−1.
C	Specific heat per unit volume at constant volume, J m−3 K−1.
v	Velocity of the energy carrier, m s−1.
K_B	Boltzmann constant, 1.381 × 10−23 J K−1.
n_m	Molecular number density, m−3.
m	Molecular mass of the energy carrier, or lumped mass kg.
T	Temperature, K.
V'	Volume, m3.
V	Voltage, V.
C_{chip}	Thermal capacitance of chip, J K−1.
$C_{resonator}$	Thermal capacitance of resonator, J K−1.
A_c	Cross-sectional area, m2.
A_s	Surface area, m2.
q'	Rate of joule heat per unit volume, W m−3.
q	Rate of total heat generated, W.
l	Length, m.

E	Modulus of elasticity, N m−2.
I	Area moment of inertia, m4.
P	Axial force, N.
ml	Mass per unit length, kg m−1.
f_r,	Frequency, Hz.
b	Damping coefficient, N.s. m−1
k, k_1, k_2, k_3	Stiffness, N m−1
Q	Quality factor
ω_r	Natural frequency, rad s^{-1}
V_{bias}	Electrical bias voltage
V_{in}	Input ac stimulus voltage
C_{in}, C_{out}	Capacitance for input and output electrodes with the resonator beam
i_{out}	Output electric current
η_{in}, η_{out}	Electrostatic transduction factor
d, g	Gap between the electrodes and the resonator beam, m
R_x	Motional resistance, Ω
β	Mode constant
$\rho_{y_1 y_2}$	Cross correlation coefficient between two measurements y_1 and y_2
Γ_x	Acceleration sensitivity in x direction, ppm g^{-1}
a_x	Acceleration in x direction, g
f_0	Resonator frequency without acceleration, or carrier frequency, Hz
f_v	Frequency of external vibration, Hz
t	Time, s

u, u_1, u_2	Displacement, m
ε_{ij}	Linearized strain
K	Global stiffness matrix
K_e	Element stiffness matrix
E_e	Young's modulus of a discrete element (used for stiffness matrix)
$\rho(x)$	Density function
f, f_{ext}	Force, N
$\Lambda, \lambda^-, \lambda^+$	Lagrange multiplier
p	Penalty function
c	Compliance

Chapter 1

Introduction

1.1 Timekeeping

A resonator is used to create an oscillator which can be used for frequency reference or timekeeping. People have been making a constant effort to measure time as accurately as possible since several thousand years ago. Around 3100 BCE (Before the Common Era) Egyptians devised a 365 day calendar which seems to be one of the earliest years recorded in history [1] – [3].

1.1.1 Early Clocks

All clocks must have two basic components: a repetitive process or action which occurs at a regular interval of time, and a means of measuring or keeping track of the time interval. Sun Clocks in the form of Obelisks, Fig. 1.1, were built by Egyptians around 3500 BCE [1] – [3]. The moving shadows of Obelisk (slender, tapering, four-sided monument) formed a kind of sundial enabling people to partition the day into morning and afternoon. Water clocks were among the earliest timekeepers which didn't rely on celestial bodies. Greeks began using them around 325 BCE to determine hours at night [1] – [3]. These were stone vessels that allowed dripping water at a nearly constant rate from a small hole near the bottom.

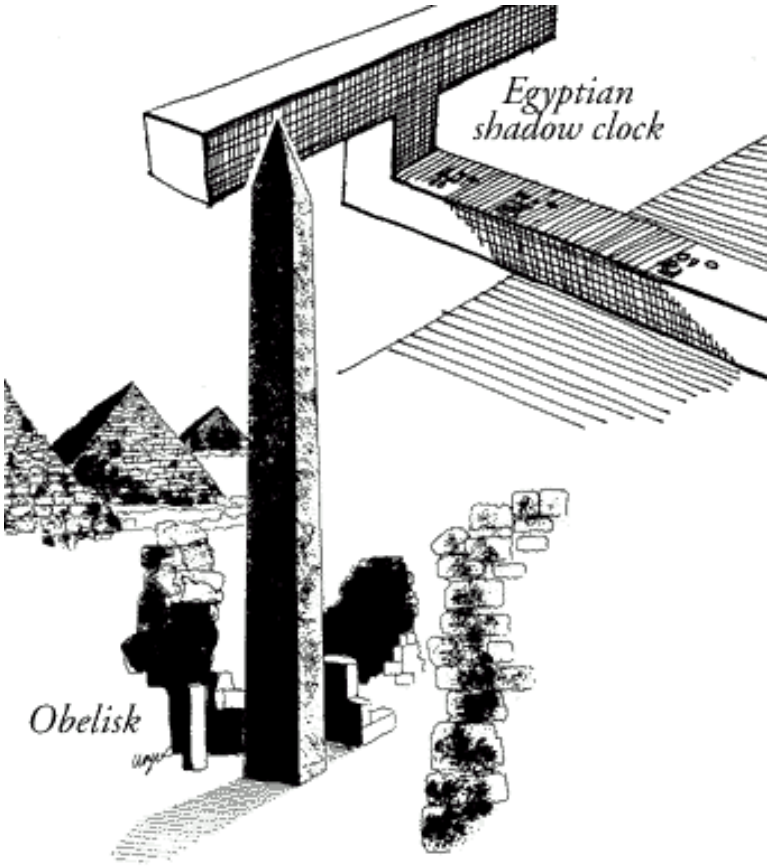

Fig. 1.1: Obelisk Sun Clock built as early as 3500 BCE by Egyptians

1.1.2 Accurate Mechanical Clock

In the quest for better year-round accuracy, sundials evolved from flat horizontal or vertical plates to more elaborate forms. For many centuries, simpler and pocket sundials were commonly used by the people. No major technological advancement happened until recently in human history. In 1656, Christiaan Huygens, a Dutch scientist, made the first mechanical pendulum clock which had an error of less than 1 minute a day [1] – [3], the first time such an accuracy had been achieved. In 1721, George Graham improved the pendulum clock's accuracy to 1 second per day by compensating for

changes in the pendulum's length due to temperature variations. Over the next centuries further refinements led to more and more accurate clocks.

1.1.3 Quartz Clocks

The quartz clocks, developed in 1920 and onward, improved the timekeeping performance far beyond that achieved earlier. A quartz clock is based on a quartz crystal resonator with an electronic oscillator (Fig. 1.2). The quartz crystal oscillator creates a signal with a frequency corresponding to the resonant frequency of the crystal resonator. The first quartz crystal oscillator was built by Walter G. Cady in 1921. In 1927 the first quartz clock was built by Warren Marrison and J.W. Horton at Bell Telephone Laboratories [4], [5]. The next several decades saw the development of quartz clocks as precision time standards, especially with regard to temperature stability. There are many acronyms of the temperature stable quartz oscillators currently used in the literature. Some of them are called TCXO, MCXO and OCXO. The TCXO stands for Temperature compensated crystal oscillator [6] in which the output signal from a temperature sensor is used to generate a correction voltage that is applied to a variable reactance in the crystal network. The reactance variations compensate for the crystal's frequency vs temperature characteristics. The temperature stability of a typical TCXO is in the order of 10^{-6} to 10^{-7} over a temperature range of -40°C to +80°C. The MCXO stands for Microcomputer compensated crystal oscillator [7] – [12] whose output frequency is modified by a dedicated microprocessor typically using either a phase-locked-loop or a digital frequency multiplier to adjust the output frequency in order to compensate for its temperature dependence. The temperature stability of a

typical MCXO is in the order of 10^{-7} to 10^{-8}. The OCXO stands for Oven controlled crystal oscillator [13] – [17] in which the output signal from a temperature sensor is used to control the temperature of the crystal resonator by keeping it inside an oven. The temperature stability of a typical OCXO is in the order of 10^{-8} to 10^{-9}. The OCXO has been shown to be the most temperature stable quartz oscillators and is commercially used for high end precision frequency reference and clocks (Fig. 1.2).

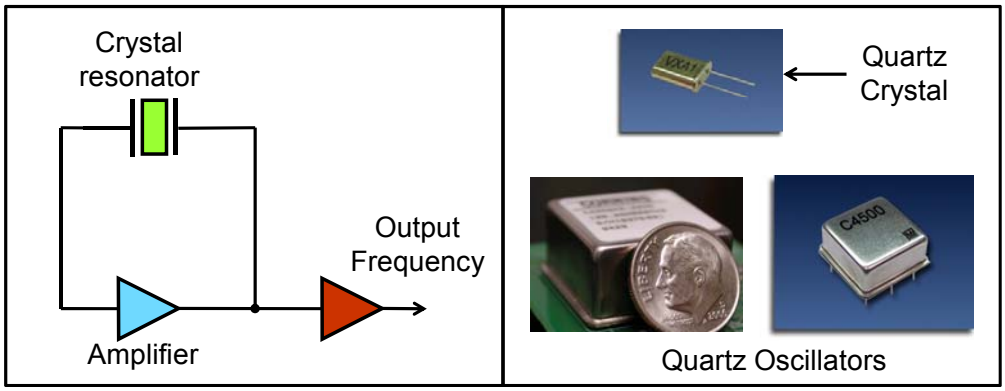

Fig. 1.2: Schematic and images of quartz crystal oscillators.

1.1.4 Atomic Clocks

The atomic clocks provide exceptionally high stable frequency output with an accuracy of better than 10^{-11} over the temperature range of -40°C to +80°C [18] – [21] and are used for critical applications like military, aerospace, research and space exploration and metrology. Owing to their high stability, the cost of the best atomic clocks can be several times higher than that of the best quartz clocks.

The principle of operation of the atomic clock is based on the energy state of the atom. When an atom changes energy from an excited state to a lower energy state, a photon is emitted. The photon frequency ν is given by Planck's law

$$\upsilon = \frac{E_2 - E_1}{h} \tag{1.1}$$

where E_2 and E_1 are the energies of the upper and lower states, respectively, and h is Planck's constant. The atomic clock is based on the above principle where the frequency is determined by the intrinsic properties of an atom. There are various types of atomic clocks. For detail understanding of atomic clocks and frequency standards, refer to [18] – [21].

1.2 Why Silicon MEMS Resonator?

MEMS stands for "Micro Electro Mechanical System". Silicon MEMS resonator has the potential to replace quartz crystal for timing and frequency reference application [22] – [30]. Beyond frequency references, MEMS resonators can also be used as a sensor [31] – [42], RF filters and mixers [43] – [44], and atomic force microscopy [45]. Sensors for mass (vapor, chemicals, protein, etc.) [31] – [35], pressure [36], [37], strain, force and acceleration [38] – [41], and temperature [42] are well reported in the literature.

Almost all electronic instruments and communication system use some kind of timer or frequency reference; and this multi-billion dollar oscillator market is currently dominated by quartz crystal. Silicon micromechanical resonator has several advantages over quartz resonator. Some of its advantages are related to its fabrication technology which leverages the IC fabrication technology allowing it to be CMOS compatible [46], [47], resulting into lower cost, smaller form factors, increased reliability and manufacturability, and single chip solutions. Previous research work has shown that the silicon micromechanical resonator has excellent long term stability of better than 1ppm [48] – [50] and a temperature stability of upto 10^{-7} [51], [52]. However, there are some challenges to overcome in terms of achieving temperature stability close to that of OCXO (10^{-9}).

One of the biggest advantages of MEMS resonator, not mentioned above, is its low power consumption and a good dynamic thermal response. As mentioned before, oven controlled oscillators provide better temperature stability due to feedback control of resonator temperature. However, the temperature control or ovenization of the resonator leads to power consumption. In case of quartz, that is OCXO, this power consumption can be huge and can go up to several watts [13] – [17] compared to sub-watt power consumption in MEMS resonator [53] – [56]. Another factor which is key to the performance of oven controlled oscillators is its dynamic thermal response, where MEMS resonator outweighs quartz crystal. The advantages of low power consumption and a good dynamic thermal response of MEMS resonator are simply due to its small size. It is possible to further reduce its power consumption and the dynamic thermal

response by better design and optimization. The thesis focuses on this aspect of the research work. Also, for oven controlled oscillators a temperature sensor with low thermal lag and high resolution is required. The OCXO uses a beat frequency based temperature sensor which allows the quartz crystal resonator to sense its own temperature thereby eliminating any thermal lag. One of the main reasons for OCXO to achieve high temperature stability is the realization of the beat frequency thermometry. This technique of temperature sensing was difficult to realize in MEMS resonator before. The thesis also demonstrates on silicon resonator based beat frequency thermometry.

1.3 Thesis Organization

The main contribution of this thesis is the silicon micromechanical resonator based beat frequency thermometry, thermal isolation of the resonator to reduce the power consumption for oven control oscillator, analysis of mechanical isolation of the resonator to understand the mechanical stability of the device, and the topology optimization of the resonator structure to increase both the thermal as well as the mechanical isolation simultaneously. The rest of this thesis is organized as follows:

Chapter 2 describes the modeling of the electrostatic MEMS resonator and the schematic of the micro-oven controlled oscillators, explaining the importance of a good thermometer and the thermal isolation.

Chapter 3 presents a beat frequency digital temperature sensing technique using a CMOS compatible encapsulated micromechanical resonator. A dual-resonator design is described that includes a pair of resonators with differential temperature compensations so that the difference between the two resonant frequencies is a sensitive function of temperature. We demonstrate a temperature resolution of approximately 0.008 °C for 1 s averaging time, which is better than that of the best CMOS temperature sensors available today.

Chapter 4 demonstrates an efficient local-thermal-isolation mechanism for a micro-oven controlled resonator, which can reduce the power requirement by 20x and the thermal time constant by 50x. In this method, the mechanical suspension of the resonator is modified to provide thermal isolation and include an integrated resistive heater. This combination provides mechanical suspension, electrical heating, and thermal isolation in a compact structure that requires low heating power and has a small thermal time constant.

Chapter 5 describes the analysis of the mechanical isolation of the silicon micromechanical resonator. The chapter presents an investigative study of mechanical robustness of the electrostatically coupled encapsulated DETF resonator. This study of mechanical isolation of the resonator is necessary in order to understand the limit of the thermal isolation.

Chapter 6 gives an analysis of topology optimization of the MEMS resonator structure to improve both the thermal and mechanical isolation simultaneously. A new design having 2x further reduction in power consumption and 10x improvement in the mechanical stiffness is described.

Chapter 7 is a conclusive summary of the work and the possible future direction.

Chapter 2

MEMS Resonator and Oven Control

2.1 Encapsulated Silicon Resonator

The encapsulated silicon micromechanical resonator uses the epi-seal process [57], [58] which provides a clean enclosure for silicon devices with a low pressure in the vacuum cavity and no contaminants which would affect the operation of the resonator after the encapsulation. The process uses silicon dioxide for the sacrificial material, epitaxial silicon for the structural layer, vapor-phase hydrofluoric acid to remove the silicon dioxide, and epitaxial silicon to seal the openings in the structural layer. A typical fabricated silicon resonator chip is shown in Fig. 2.1. The resonator is fabricated in the device layer which is supported by the silicon substrate and encapsulated by the top layer (Fig. 2.2). The resonator is in the vacuum cavity which has pressure as low as 1 Pa [57]. The chip is attached to a package using an adhesive and wire bonded to make electrical contacts (Fig. 2.1 and Fig. 2.2). The package is in-turn soldered to a printed circuit board (PCB) having oscillator circuit. Fig. 2.3 shows the schematic of 3D cross-section view of the chip. The 20μm thick device layer is separated by 2μm thick oxide layer from the substrate and the encapsulation layer. A typical double-ended tuning fork (DETF) type of resonator with input and output electrodes are etched in the device layer (Fig. 2.3).

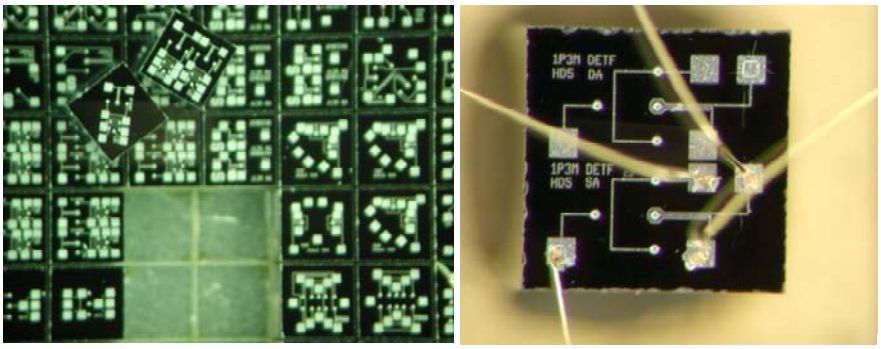

Fig. 2.1: Diced fabricated encapsulated resonator chips (left) and a wire-bonded chip to the package (right).

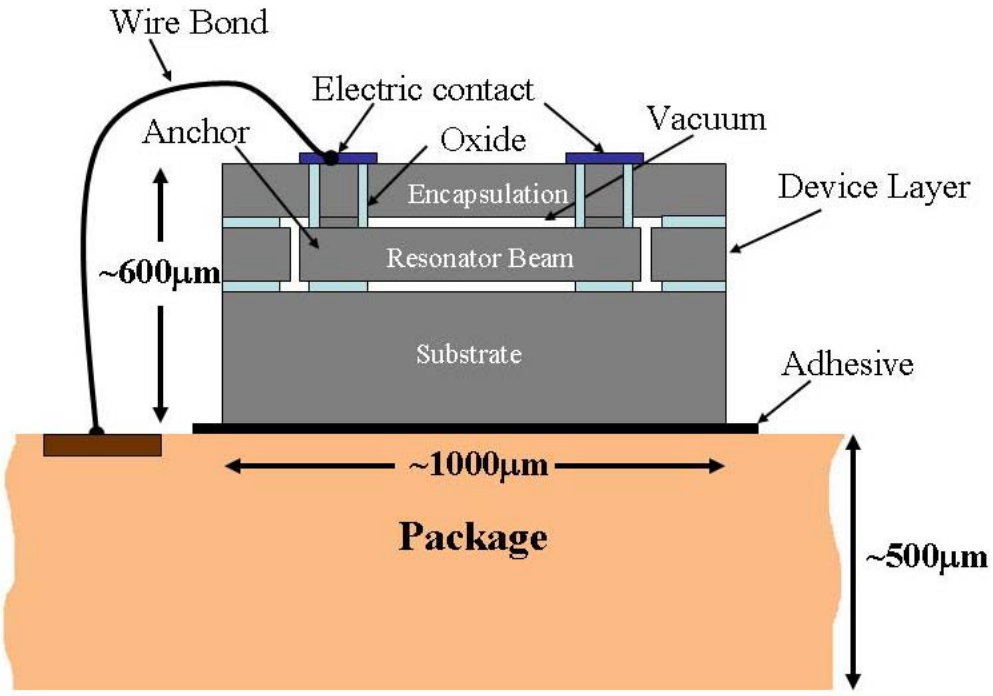

Fig. 2.2: A schematic of a typical encapsulated silicon MEMS resonator die (chip).

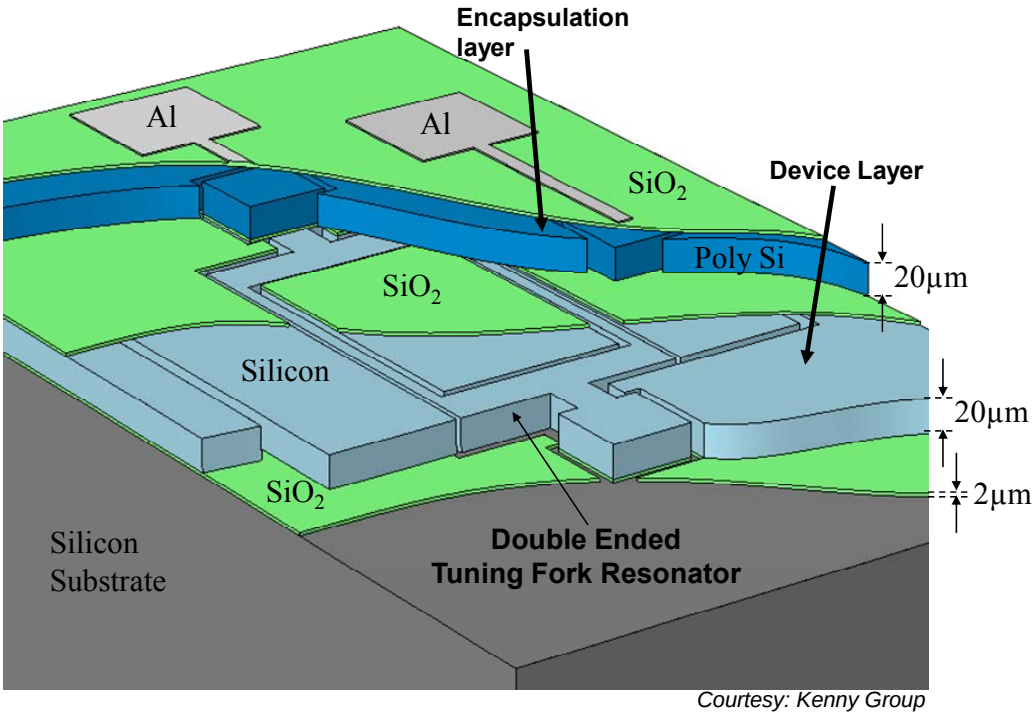

Fig. 2.3: A schematic of a 3D cross-section of the encapsulated silicon MEMS resonator die (chip).

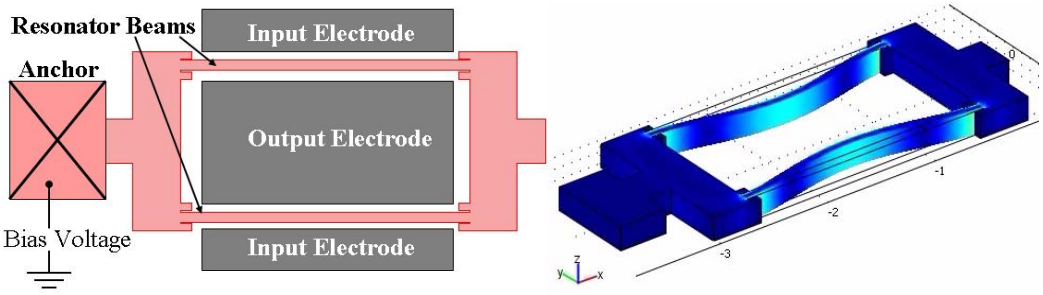

(a) (b)

Fig. 2.4: (a) A schematic of a double ended tuning fork (DETF) type silicon resonator. (b) Finite element simulation of the flexural mode of DETF resonator

The DETF resonator is designed for flexural-mode actuation, as shown in Fig. 2.4. The biased resonator beams are electrostatically actuated by providing an alternating stimulus signal to input electrode. The capacitive transduction between the beams and the input electrodes cause the resonator to vibrate. A resonance occurs when the frequency of the input stimulus signal becomes equal to the natural frequency of the flexural mode of the beam. The output signal is then amplified to measure the resonant frequency.

2.2 Linear Resonator Model

In this section we present a linear lumped model for the electrostatically actuated MEMS DETF resonator. An analysis using both mechanical and electrical model is presented here.

2.2.1 Mechanical Model

The lumped spring-mass-damper system is shown in Fig. 2.5. The basic 2nd order equation governing this system is given by

$$m\ddot{x} + b\dot{x} + kx = F_{act} \tag{2.1}$$

where x is the resonator displacement, m is the effective lumped mass, b is the damping in the system, k is the effective stiffness and F_{act} is the actuation force.

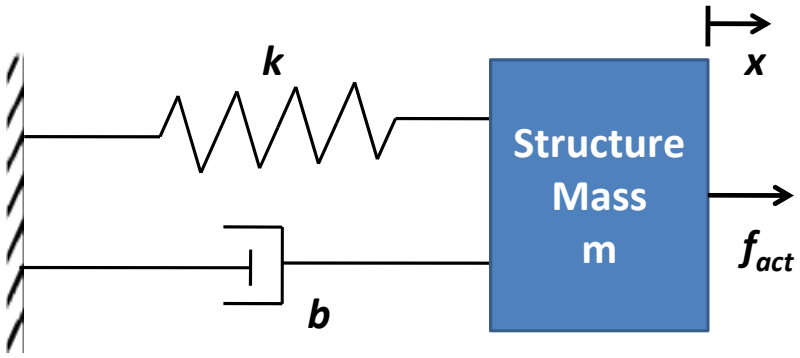

Fig. 2.5: Lumped 2nd order spring-mass-damper system for the DETF resonator.

The transfer function of the structure dynamics for the above lumped model is given as

$$H(j\omega) = \frac{X(jw)}{F_{act}(jw)} = \frac{1}{(\mathrm{j}w)^2\mathrm{m} + (\mathrm{j}w)b + k} \tag{2.2}$$

At resonance, in the absence of damping, the amplitude tends to infinity. Using equation (2.2), we get

$$(\mathrm{j}w)^2\mathrm{m} + (\mathrm{j}w)0 + k \;=\; 0 \tag{2.3}$$

resulting in

$$\omega = \sqrt{\frac{\mathrm{k}}{\mathrm{m}}} \;=\; \omega_r \; (natural\ frequency) \tag{2.4}$$

Similarly, in the presence of damping, we can find *damped natural frequency* and is given as

$$\omega_d = \sqrt{\frac{k}{m} - \left(\frac{b}{2m}\right)^2} = \sqrt{\frac{k}{m} - \left(\frac{\sqrt{km}}{2mQ}\right)^2} \qquad (2.5)$$

where, $Q = \frac{\sqrt{km}}{b}$ and is called Quality Factor

2.2.2 Electrostatic Transduction

A lumped electrical LCR model of the MEMS resonator is shown in Fig. 2.6. Here we will discuss about the method to actuate and sense the micro-mechanical resonator. The electrostatic transduction is used to actuate the resonator beams by applying AC input stimulus to the input electrode (Fig. 2.7). The principle of actuation and sense is the electrostatic attraction force that exists between a parallel plate capacitor. Fig. 2.8 shows an AC signal flow diagram for an electrostatically actuated and sensed MEMS resonator. The AC input voltage (V_{in}) applied on the input electrode is converted into the input force (F) due to electrical to mechanical capacitive transduction (η_{in}) as shown in Fig. 2.8. The force causes the oscillation of the resonator beam. When the frequency of the AC input voltage becomes equal to the natural frequency of the resonator beam, the beam starts resonating with maximum amplitude, resulting into charge modulation in the output electrode giving rise to output current (i_{out}) as shown in Fig. 2.8.

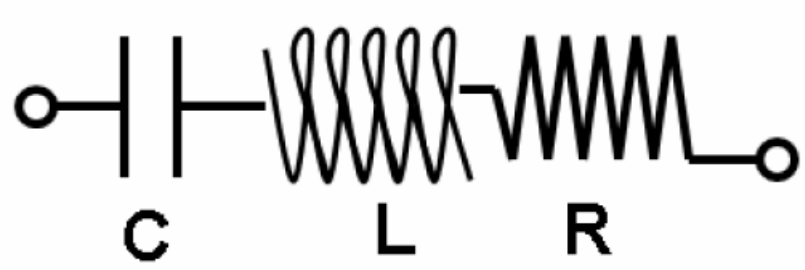

Fig. 2.6: Lumped series RLC tank resonator.

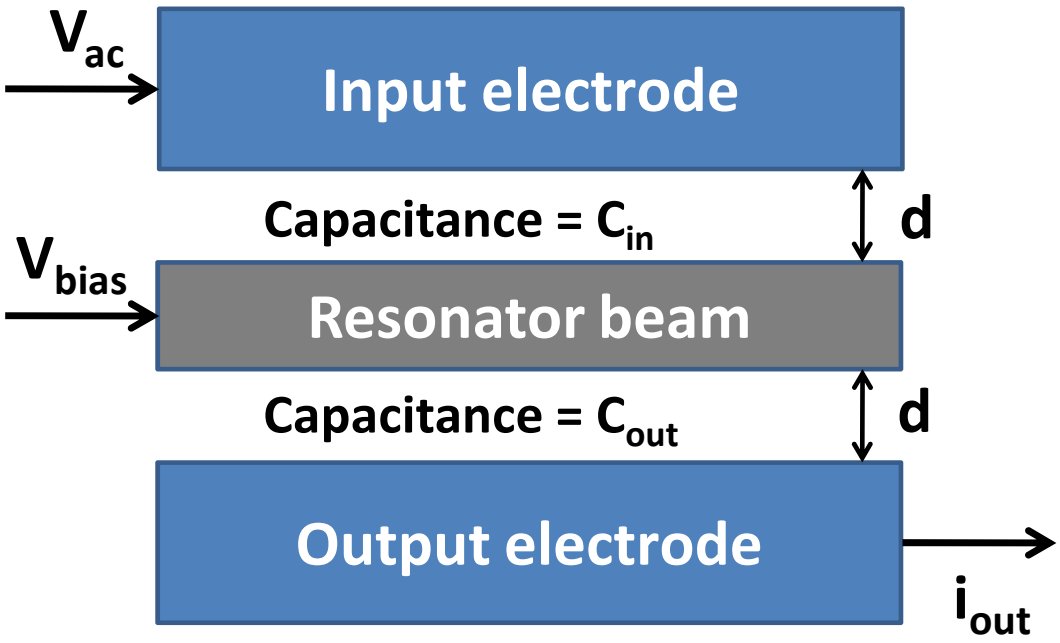

Fig. 2.7: Electrostatic transduction to actuate and sense the resonator.

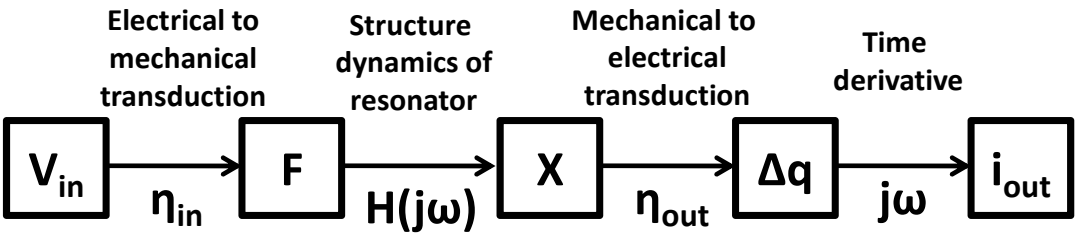

Fig. 2.8: Signal flow diagram of resonator actuation and sensing.

The transduction factor η_{in} is given as [59]

$$\eta_{\text{in}} = \frac{\partial F}{\partial V_{in}} \tag{2.6}$$

F is the actuation force which is given by

$$F \approx -(V_{bias} - V_{in})^2 \frac{C_{in}}{2d} \tag{2.7}$$

$$\therefore \quad \eta_{\text{in}} = \frac{\partial F}{\partial V_{in}} = (V_{bias} - V_{in}) \frac{C_{in}}{d} \tag{2.8}$$

$$\because \ |V_{in}| \ll V_{bias}\,, \qquad \eta_{in} = (V_{bias}) \frac{C_{in}}{d} \tag{2.9}$$

Similarly, for η_{out}, we get

$$\eta_{\text{out}} = (V_{bias})\frac{C_{out}}{d} = \frac{\partial q}{\partial x} \tag{2.10}$$

Here q represents the electric charge and ∂q represents the charge modulation on the output electrode. For symmetric design, we have $C_{in} = C_{out}$, and hence $\eta_{\text{in}} = \eta_{\text{out}}$.

The structure dynamics of the resonator called transfer function is mentioned in equation (2.2) and can be rewritten as

$$H(j\omega) = \frac{X(jw)}{F(jw)} = \frac{1}{(\text{j}w)^2\text{m} + (\text{j}w)b + k}$$

The trans-conductance of the signal flow, shown in Fig. 2.8, is given as [59]

$$\begin{aligned} Y(j\omega) = \frac{i_{out}(j\omega)}{V_{in}(j\omega)} &= \frac{i_{out}(j\omega)}{q(j\omega)} . \frac{q(j\omega)}{x(j\omega)} . \frac{x(j\omega)}{F(j\omega)} . \frac{F(j\omega)}{V_{in}(j\omega)} \\ &= (j\omega).\eta_{\text{out}}.H(j\omega).\eta_{\text{in}} \\ &= \frac{(j\omega).\eta_{\text{in}}.\eta_{\text{out}}}{(\text{j}w)^2\text{m} + (\text{j}w)b + k} \end{aligned} \tag{2.11}$$

At resonance, the above expression becomes

$$Y(j\omega) = \frac{i_{out}(j\omega)}{V_{in}(j\omega)} = \frac{\eta_{in}.\eta_{out}}{b} = \eta_{in}.\eta_{out}\frac{Q}{\sqrt{km}} = \frac{1}{R_x} \quad (2.12)$$

where R_x is called motional resistance.

The output current is dependent on the motional resistance which in-turn is dependent on the quality factor of the resonator, capacitance, gap between the electrodes and the beam, stiffness and mass of the resonator. It is desired to have high output current for better signal characteristics of the resonator frequency.

2.3 Temperature Stability

The DETF resonator described in the previous section is used in the oscillator circuit to generate continuous frequency signal (Fig. 2.9). However, this frequency changes with the temperature as shown in Fig. 2.10. The temperature dependence of the resonator frequency is referred as TCF, an abbreviation of Temperature Coefficient of Frequency. An uncompensated resonator exhibit a TCF of approximately -29 ppm/°C (Fig. 2.10).

The primary reason of such a high TCF of silicon resonator is the temperature dependence of its material characteristic. The change in Young's modulus of silicon with temperature, the TCE, is approximately -63 ppm/°C at normal operating temperatures [60] – [63].

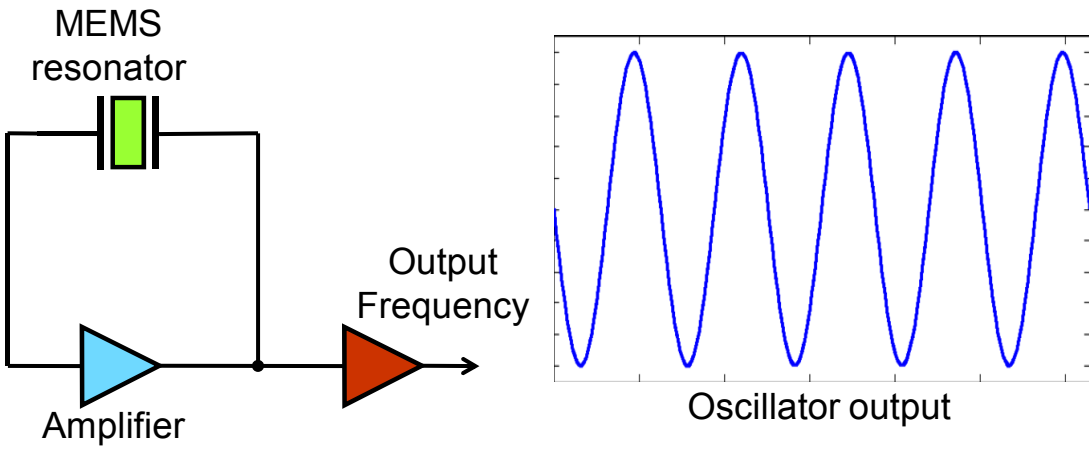

Fig. 2.9: A schematic of MEMS resonator used in oscillator circuit (left) and the output frequency signal from the oscillator (right).

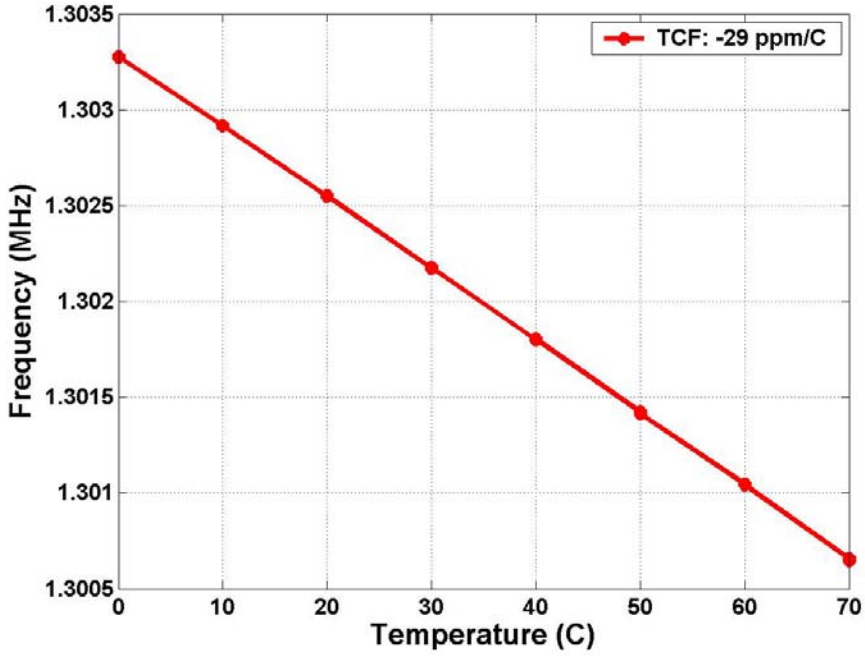

Fig. 2.10: Experimental data showing a frequency-temperature characteristic of a typical 1.3 MHz DETF resonator.

Silicon is a crystal with cubic symmetry, and its thermal expansion is the same in all directions. Therefore, even though the Young's modulus of silicon is not the same in all directions, the temperature dependent change in Young's modulus is the same in all directions.

The TCF of silicon resonator is related to its TCE [52], [64] and can be derived as shown below.

The frequency of a beam is given by

$$f_r = \frac{\beta^2}{2\pi L^2}\sqrt{\frac{EI}{\rho A}} = CE^{1/2} \tag{2.13}$$

where β is the mode constant, E is the Young's modulus and C is a constant. The derivative of equation (2.13) gives rise to

$$\frac{df_r}{dE} = \frac{1}{2}CE^{-1/2} \tag{2.14}$$

From equations (2.13) and (2.14), the TCF can be expressed in terms of TCE as

$$TCF = \frac{df_r}{f_0 dT} = \frac{1}{f_0}\frac{df_r}{dE}.\frac{dE}{dT} = \frac{1}{2}\frac{dE}{EdT} = \frac{TCE}{2} \tag{2.15}$$

From equation (2.15), the TCF of the silicon resonator can be estimated to be approximately -31 ppm/°C. However, there is a marginal effect of dimensional change on the TCF of the silicon resonator. The dimensions of the resonator change with the temperature due to thermal expansion. Silicon has an isotropic coefficient of thermal expansion (CTE, or α), at room temperature of approximately 2.6 ppm/°C [65] – [67], and that value increases with increasing temperature. The effect of α on the TCF of the resonator can be evaluated in the similar way as described for TCE and can be given as

$$TCF_{\alpha} = \frac{\alpha}{2} \tag{2.16}$$

The effect of thermal expansion on the resonator frequency is $\alpha/2$ and is approximately +1.3 ppm/°C. The final TCF of the resonator, taking both TCE and α into account, comes to approximately -30 ppm/°C, which is close to the experimental TCF measurement shown in Fig. 2.10.

2.4 Temperature Control of Resonator (Micro-Ovenization)

There are many ways to compensate for the temperature dependence of the silicon resonator. However, temperature-control of the resonator has the potential of providing one of the most stable silicon resonators similar to OCXO [13] – [17]. In this method, the temperature of the resonator is kept constant at a certain predefined set value by using a feedback control as shown in Fig. 2.11. The feedback control uses a thermometer to sense the temperature of the resonator and a heater to heat the resonator

in order to keep its temperature constant and as stable as possible. However, an external temperature sensor exhibit thermal lag due to a physical separation between the thermometer and the resonator. Similarly, the heater has to be close to the resonator and provide heating only to the resonator without losing much heat to the surrounding in order to have low power consumption and small thermal time constant.

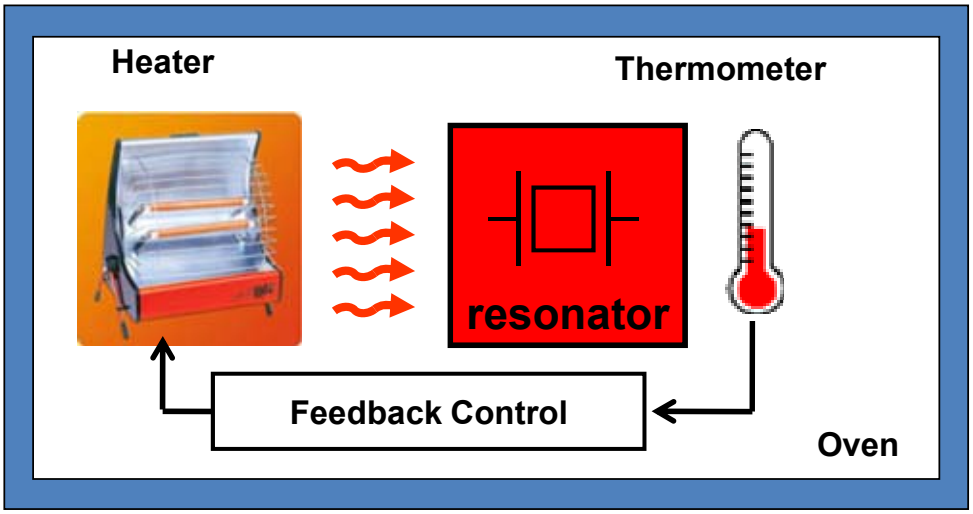

Fig. 2.11: Schematic of feedback control of the resonator using an external thermometer and a heater.

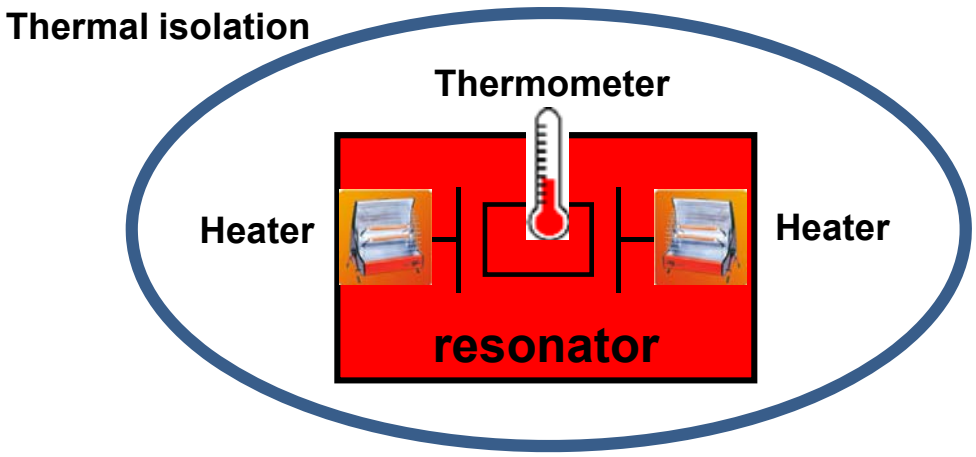

Fig. 2.12: Schematic of a resonator with thermometer and heater integral to it, with thermal isolation preventing heat loss to the surrounding.

To achieve a design having a thermometer with small thermal lag and a heater with low power consumption and small thermal time constant, the heater and the thermometer have to be integral to the resonator with thermal isolation preventing heat loss to the surrounding as shown schematically in Fig. 2.12. Chapter 3 and 4 describe techniques to achieve such a design.

Chapter 3

Beat Frequency Thermometry

A digital temperature sensing technique using a complementary metal oxide semiconductor (CMOS) compatible encapsulated micromechanical resonator is presented. This technique leverages our ability to select the temperature dependence of the resonant frequency for micromechanical silicon resonators by adjusting the relative thickness of a SiO_2 compensating layer. A dual-resonator design is described that includes a pair of resonators with differential temperature compensations so that the difference between the two resonant frequencies is a sensitive function of temperature. We demonstrate a temperature resolution of approximately 0.008 °C for 1 s averaging time, which is better than that of the best CMOS temperature sensors available today. At the same time, the beat frequency thermometry is highly effective in the temperature compensation of the resonator as it eliminates the thermal lag.

3.1 Introduction

The frequency of silicon resonators varies strongly with temperature [52], [64], [68]. This characteristic of a silicon resonator, which is disadvantageous in general, can be used to measure temperature. However, the biggest problem lies in measuring the temperature-dependent frequency without using any external frequency references. In

this work, we present a novel dual-resonator design with a composite Si–SiO_2 structure [69], [70], which provides a temperature-dependent signal and a reference for measuring the signal. This concept for digital thermometry relies on the application of the basic mechanics of resonator design, as well as the materials physics that provides different temperature coefficients of stiffness for silicon and SiO_2. In this design, we build a pair of resonators with different cross-sectional dimensions, but with similar frequencies, by scaling the lengths. After formation of an oxide compensation layer over all surfaces, we obtain a pair of resonators with similar frequencies but with different temperature coefficients of frequency. The difference frequency, called beat frequency, between these two references has a much higher sensitivity to temperature, and it can be "internally counted" using one of the resonators as a reference [71], [72]. Taken together, the physics of compensated micromechanical resonators and the ultra-stable resonator encapsulation process provides path toward a unique, CMOS-compatible digital temperature sensor with potential for much better performance than existing digital temperature sensors based on diode thermometers.

3.2 Beat Frequency Generation

The multiplication of the two oscillator signals at frequencies f_1 and f_2 yields signals at frequencies $f_1 + f_2$ and $f_1 - f_2$ as per Eq. (3.1). The difference frequency $f_1 - f_2$ is called the beat frequency and is obtained after discarding the higher frequency through the second order low-pass filter as shown in Fig. 3.1.

$$cos(2\pi f_1 t).cos(2\pi f_2 t) = \frac{1}{2}[cos\{2\pi(f_1 + f_2)t\} + cos\{2\pi(f_1 - f_2)t\}] \quad (3.1)$$

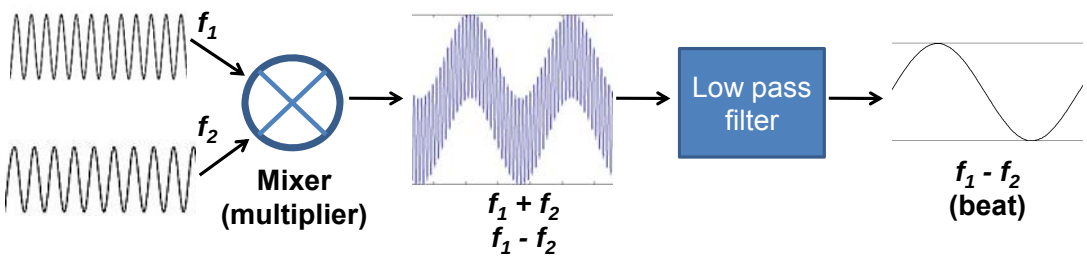

Fig. 3.1: Beat frequency generation technique

The temperature dependence of f_1, f_2, and f_{beat} can be expressed as

$$f_1(T) = f_1(T_0) + a_1\Delta T + b_1\Delta T^2 + \ldots \quad (3.2)$$

$$f_2(T) = f_2(T_0) + a_2\Delta T + b_2\Delta T^2 + \ldots \quad (3.3)$$

$$f_{beat}(T) = f_{beat}(T_0) + (a_1 - a_2)\Delta T + (b_1 - b_2)\Delta T^2 + \ldots \quad (3.4)$$

where a's and b's are constants representing temperature sensitivities of $f_1$and f_2 , T_0 is reference temperature, and $\Delta T = T - T_0$. The fractional change in beat frequency is given as

$$\frac{\Delta f_{beat}(T)}{f_{beat}(T_0)} = \frac{(a_1 - a_2)}{f_{beat}(T_0)}\Delta T + \frac{(b_1 - b_2)}{f_{beat}(T_0)}\Delta T^2 + \ldots \quad (3.5)$$

It has been observed from experiments that the higher order terms are much smaller than the first order term of Eq. (3.5) and can be ignored for simplification. Therefore, the fractional change in beat frequency after ignoring the higher order terms is given as

$$\frac{\Delta f_{beat}(T)}{f_{beat}(T_0)} = \frac{(a_1 - a_2)}{f_{beat}(T_0)}\Delta T = c_1 \Delta T \quad (3.6)$$

where c_1 is the first order TCf (ppm/°C) of the beat frequency.

The equation (3.6) shows that the temperature dependence (TCF) of beat frequency is directly proportional to the difference in TCF's of the frequencies f_1 and f_2. The TCF of the beat frequency c_1 increases with the increase in $(a_1 - a_2)$ and decrease in the absolute value of f_{beat}. To obtain a beat frequency with large temperature sensitivity, the difference in TCf of f_1 and f_2 should be as large as possible and at the same time the beat frequency should be as small as feasible. The fundamental requirement of the beat frequency thermometry is to have two different frequency sources with different temperature sensitivities.

3.3 Si-SiO_2 Composite Resonator

One way of realizing a resonator with different temperature sensitivity is to form a composite resonator. Our lab came up with a novel technique of forming a Si-SiO_2 composite resonator [70]. The temperature dependence of the silicon resonator frequency is mainly related to its material properties as shown in equation (2.15) and can be rewritten here as

$$TCF_{silicon\ resonator} \approx \frac{TCE_{silicon}}{2}$$

where $TCE_{silicon}$ stands for temperature coefficient of Young's modulus of silicon.

The $TCE_{silicon}$ is approximately -60 ppm/°C. In other words, Si becomes soft with the increase of temperature. On the other hand, if we take a look at the properties of SiO_2, it becomes hard with the increase of temperature (Fig. 3.2). By combining the material properties of both Si and SiO_2, it is possible to alter or reduce the $TCF_{silicon\ resonator}$ [70]. The Fig. 3.3 shows the SEM image of a fabricated composite resonator where the SiO_2 is thermally grown over the silicon. The resulting TCF of a composite resonator is shown in Fig. 3.4 which is almost passively compensated.

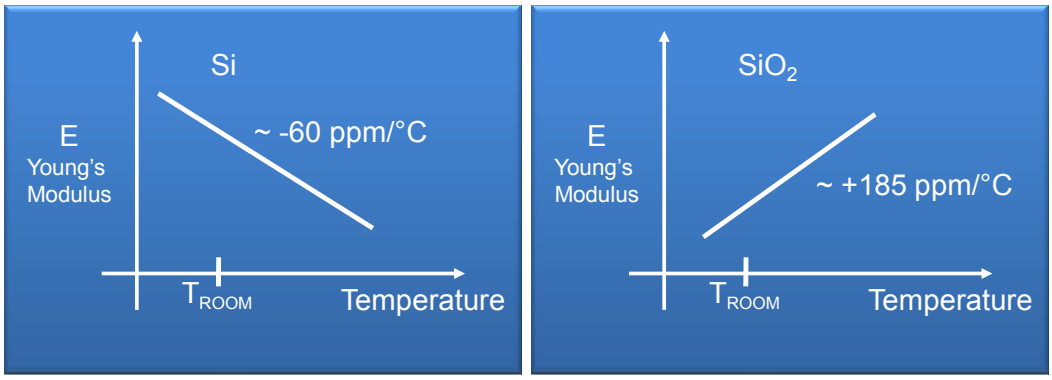

Fig. 3.2. Comparison of the temperature dependence of the Young's Modulus of Si and SiO_2.

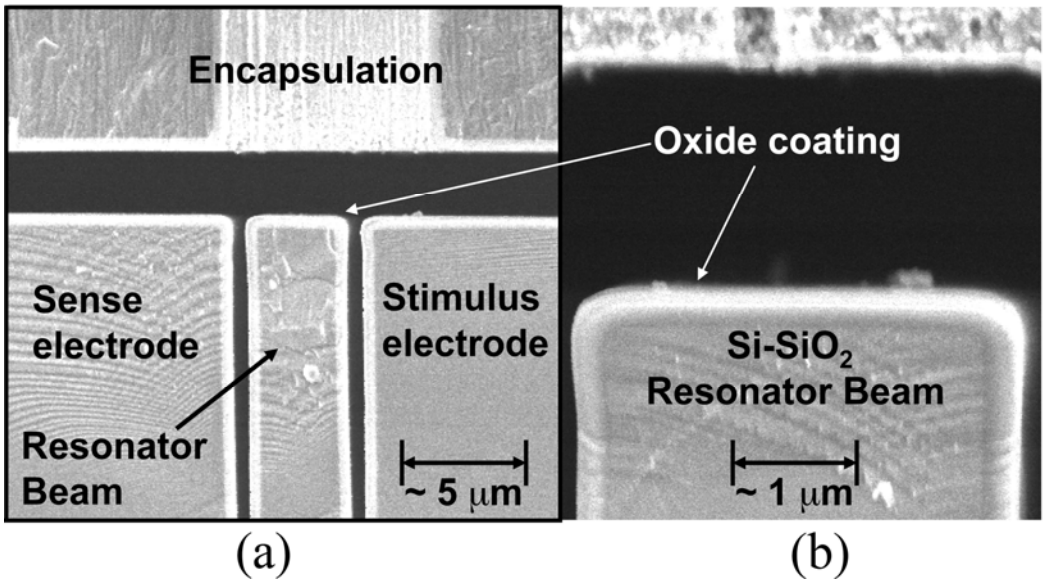

Fig. 3.3. (a) SEM image of a composite silicon resonator beam with the thermally grown SiO_2 layer. (b) Enlarged view.

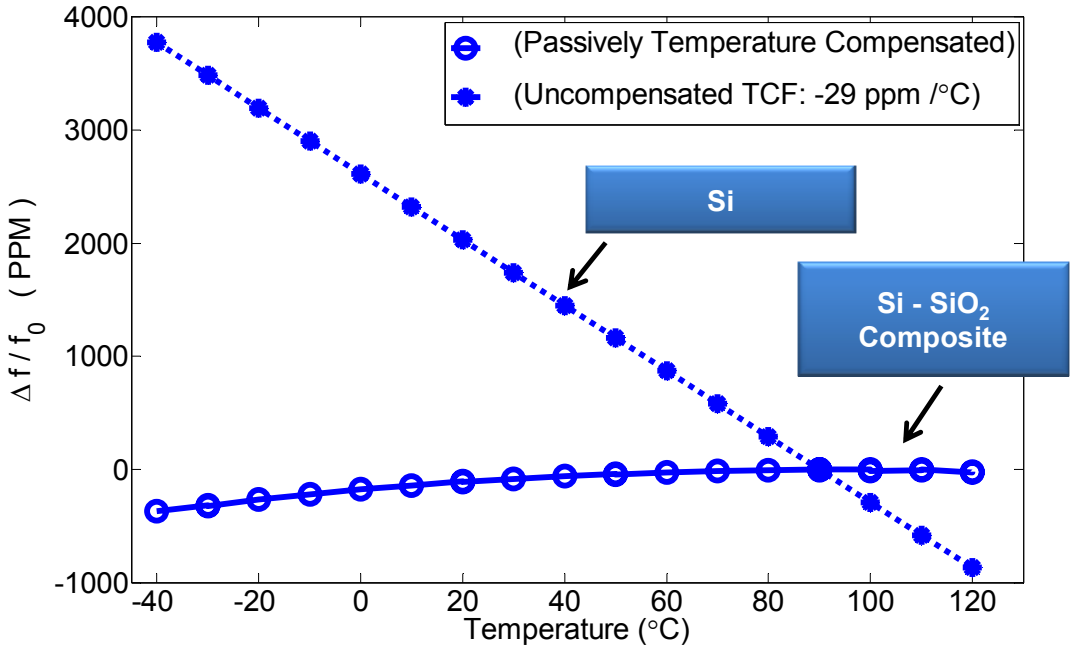

Fig. 3.4. Experimental data showing the comparison of TCF of bare silicon and the composite silicon.

3.4 Dual-Resonator Design

A candidate dual-resonator design having two mechanically coupled double-ended tuning fork (DETF) type resonators is shown in Fig. 3.5. These DETF resonators consist of composite resonator beams of silicon (Si) and silicon dioxide (SiO_2). The thickness of the thermally grown SiO_2 coating over the Si beam is approximately 0.33 μm for both resonators (Fig. 3.5). The silicon-to-oxide ratio of the beams for the two DETF structures is designed to achieve two different temperature coefficients of frequency (TCf), while keeping the two frequencies close together. These devices were fabricated using a CMOS-compatible wafer scale encapsulation process [57], [58]. A scanning electron microscopy view of the thermally grown SiO_2 coating over the Si beam [70] is shown in Fig. 3.3 and Fig. 3.6.

The beam cross-sections of the two resonators in the dual resonator design and the ratio of Si to SiO_2 thicknesses dictate the TCF of the two frequencies signal f_1 and f_2 (Fig. 3.7). The beam with 10μm thickness has less effect of 0.33μm thick SiO_2 and hence has higher TCF compared to the beam with 4μm thickness having 0.33μm thick SiO_2 as shown in Fig. 3.7.

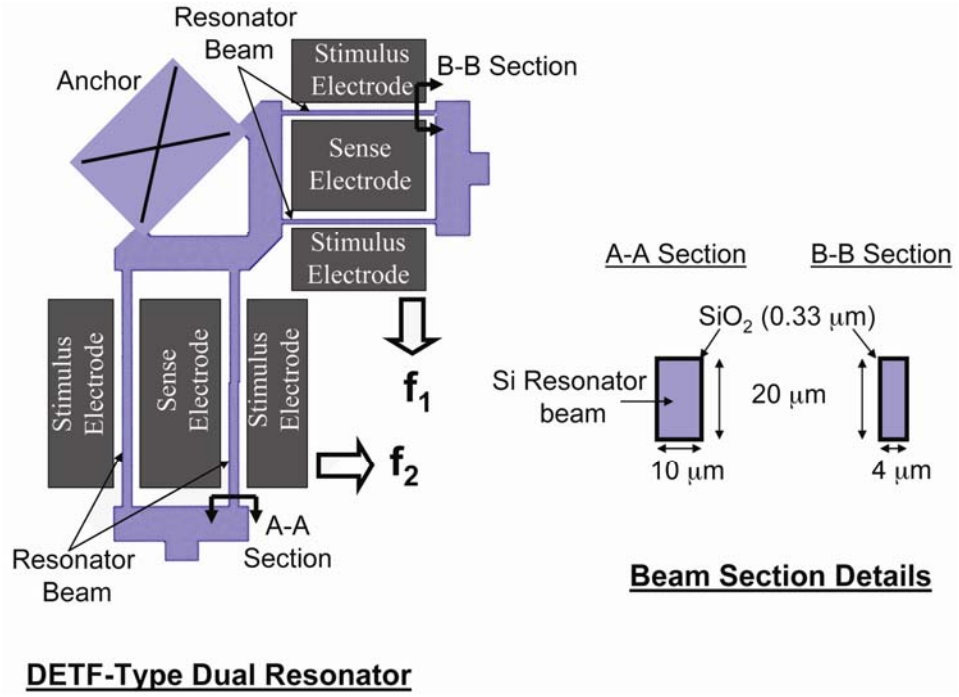

Fig. 3.5. Dual resonator design showing the two DETF resonators with different cross sections having the same SiO_2 thicknesses. Both the resonators are anchored at a common point to ensure uniform temperature across the entire structure of the dual resonator.

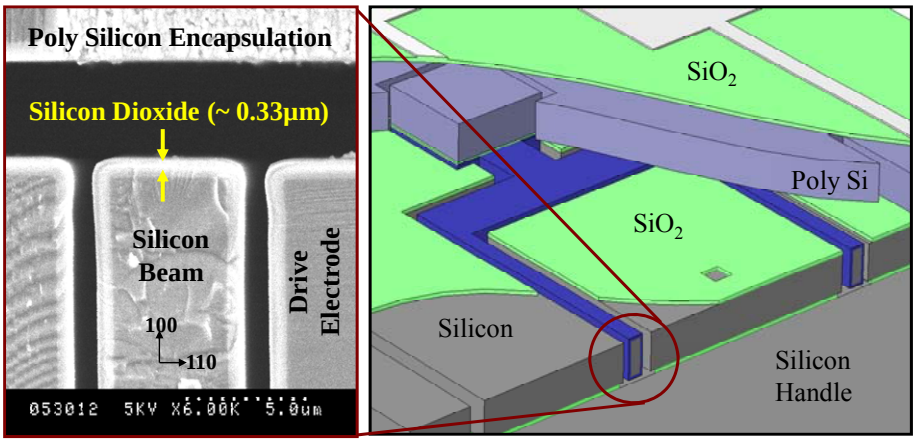

Fig. 3.6. SEM image of the composite resonator with 0.33μm SiO_2 coating over the Si beam.

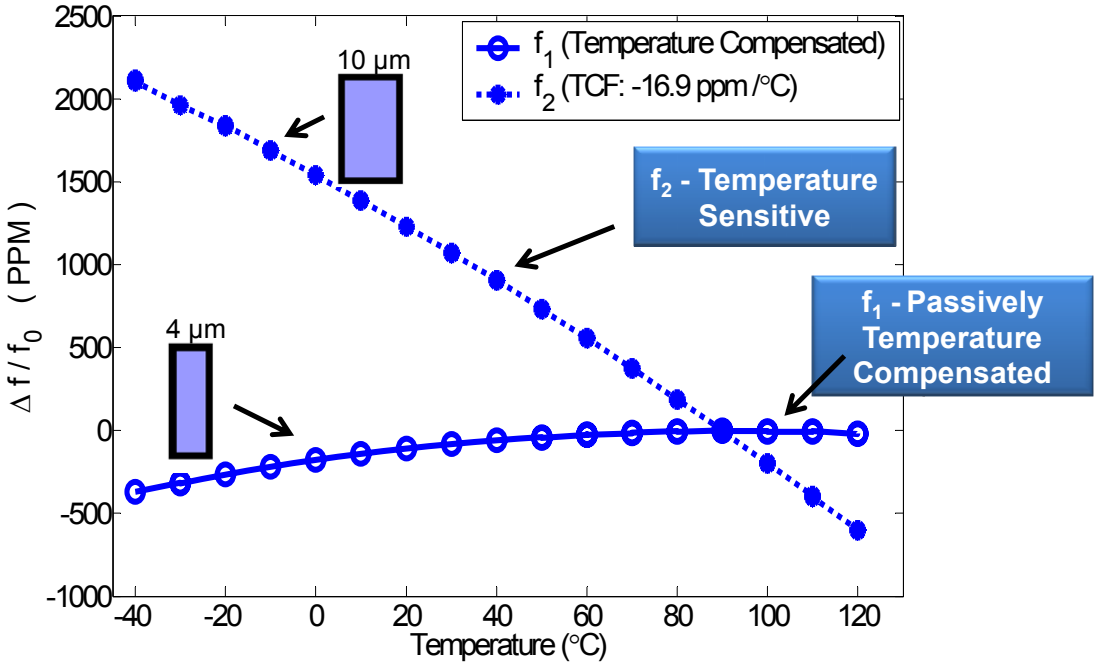

Fig. 3.7. Experimental data showing temperature dependence of f_1 and f_2 of the dual resonator.

The two reference frequencies, f_1 and f_2, from the dual resonator are mixed to form the difference frequency or beat frequency, f_{beat}, as shown in Fig. 3.8. There are, of course, many analog and digital methods for obtaining the beat frequency signal. In our experiment, the frequency mixing is performed using a four-quadrant analog multiplier AD734. The purpose of forming beat frequency is to generate a signal with higher temperature sensitivity.

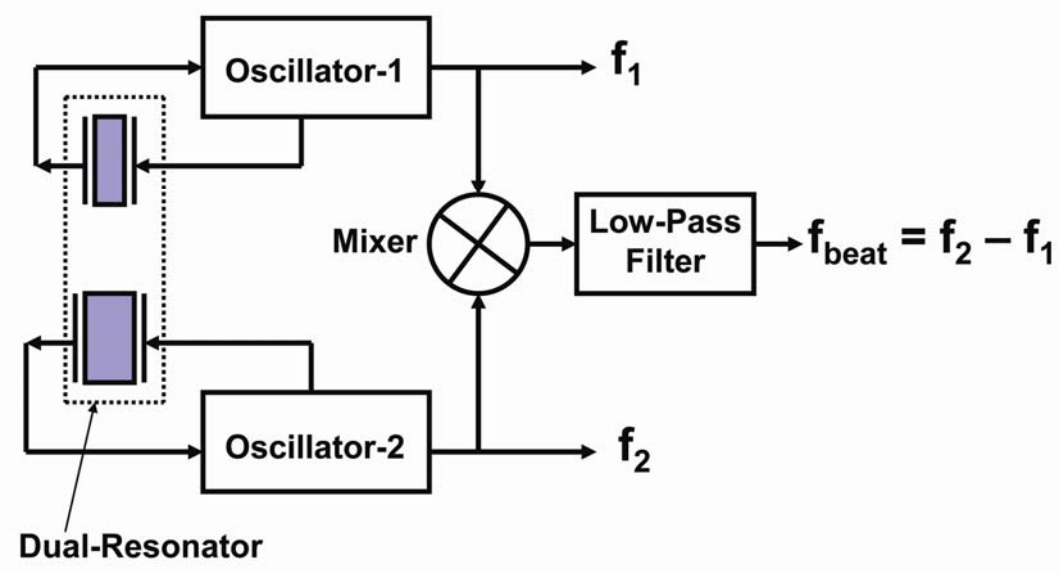

Fig. 3.8. Illustration of the beat frequency generation technique using dual resonator.

The fractional change in beat frequency can be obtained by re-writing the equation (3.5) once again as given below

$$\frac{\Delta f_{beat}(T)}{f_{beat}(T_0)} = \frac{(a_1 - a_2)}{f_{beat}(T_0)}\Delta T + \frac{(b_1 - b_2)}{f_{beat}(T_0)}\Delta T^2 + \ \ldots \qquad (3.7)$$

From the measured data of f_{beat} (Fig. 3.7), using quadratic curve fit, it is observed that the first order term of Eq. (3.7) is approximately 360 ppm as compared to 0.069 ppm for the second order term for the temperature range of −40 to 120 °C. Therefore, we ignore the higher order terms and re-write the equation (3.6) to find the fractional change in beat frequency as given below

$$\frac{\Delta f_{beat}(T)}{f_{beat}(T_0)} = \frac{(a_1 - a_2)}{f_{beat}(T_0)}\Delta T = c_1 \Delta T \quad (3.8)$$

The dual resonator described in this work produces reference frequencies f_1 and f_2 of approximately 1.37 and 1.45 MHz, respectively, resulting in a beat frequency f_{beat} of approximately 75 kHz. The resonator with frequency f_1 is passively temperature compensated to first order (Fig. 3.7), while the resonator with frequency f_2 has a larger TCf of −17 ppm/ °C. We obtain a pair of resonators with the same frequency but with different TCfs by scaling one design with respect to the other and growing the same thickness of oxide on both. Since the frequencies of the dual resonator are close together, the beat frequency is exceptionally sensitive to temperature changes, as per Eq. (3.8), and nearly linear, as shown in Fig. 3.9, with a TCf of approximately −360 ppm/ °C. The high sensitivity and the linearity of the beat frequencies have been verified on several devices as shown in Fig. 3.10.

3.5 Sensor Application

The dual resonator based beat frequency temperature sensor described above can be used both for the temperature compensation of the resonator as well as for the general purpose CMOS digital temperature sensor. For the temperature compensation, the beat frequency acts as a self-temperature sensor of the resonator, thereby avoiding any thermal lag associated with an external temperature sensor. Fig. 3.11 describes the significance of the beat frequency thermometry for sensing the resonator temperature compared to an external temperature sensor.

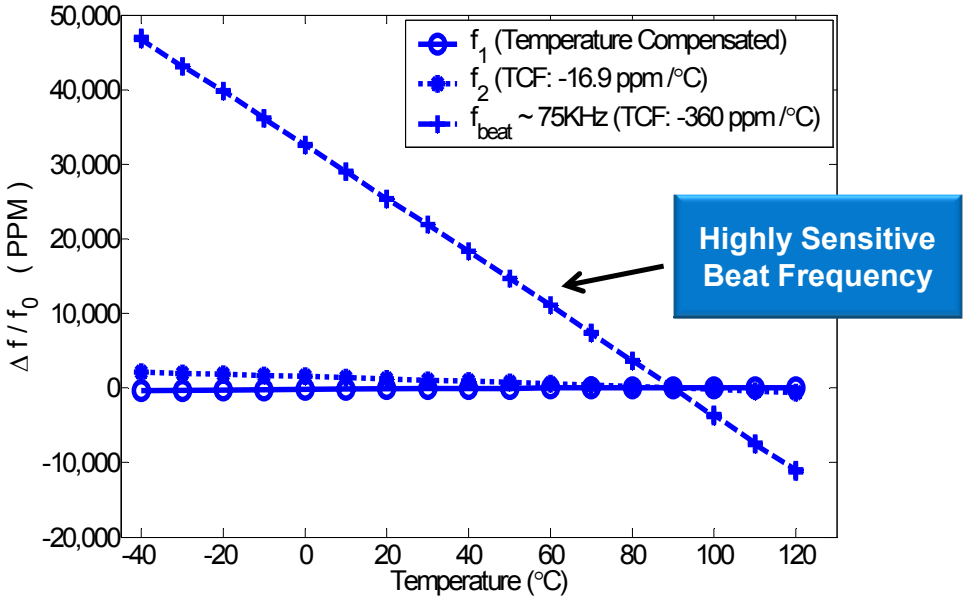

Fig. 3.9: Experimental data showing comparison of the temperature dependence of the beat frequency with that of the dual resonator frequencies.

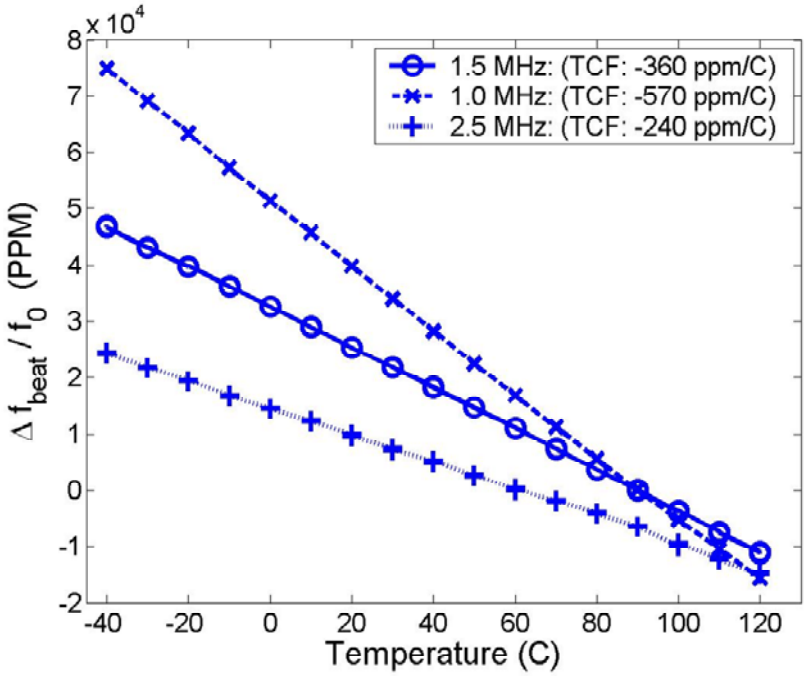

Fig. 3.10: Experimental data showing temperature dependence of f_{beat} for various designs having resonator frequencies in the range of 1.0MHz, 1.5MHz and 2.5MHz.

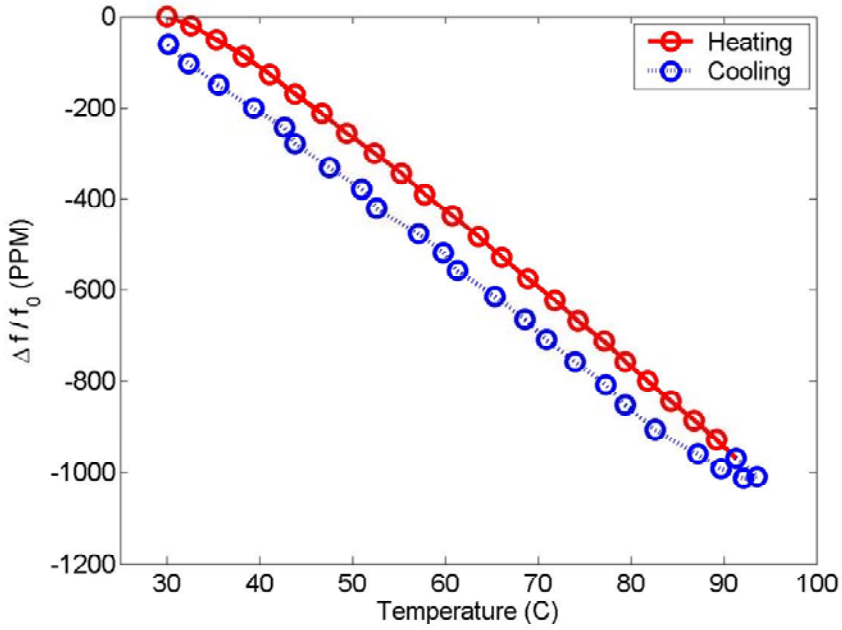

(a)

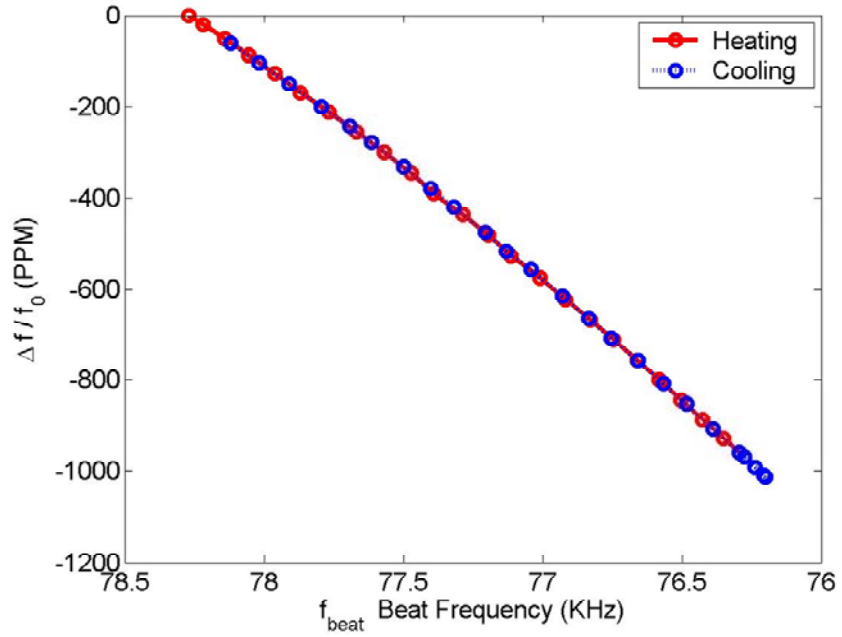

(b)

Fig. 3.11: Experimental data showing resonator f-T characteristic in rapid-temperature cycling (slew rate ~ 6°C /min) using (a) an external temperature sensor – Pt. RTD (b) beat frequency as a temperature sensor.

To measure the resonator *f-T* characteristic under two different conditions – (a) external temperature sensor and (b) beat frequency of the resonator as its own temperature sensor; a dual resonator device with a Pt. RTD temperature sensor was kept inside an oven. During a rapid temperature cycling (~ 6°C /min) from 30°C to 100°C to 30°C, a measurement of f versus T shows a large hysteresis (Fig. 3.11(a)) due to thermal lag between the external temperature sensor (Pt. RTD) and the resonator. The f versus f_{beat} characteristics shows no hysteresis (Fig. 3.11(b)) on the same scale, because there is no physical separation between the thermometer and the resonator.

To understand the efficacy of this micromechanical resonator based beat frequency thermometry as a general purpose digital temperature sensor, it is necessary to find the resolution of the sensor.

3.6 Sensor Resolution

To compute the resolution of the beat frequency temperature sensor it is important to be able to distinguish errors in temperature measurement from random variations in the true temperature of the measurement environment. The resolution of the beat frequency temperature sensor is measured using a correlation technique [73] – [75], because the expected resolution was below the stability of our measurement oven and beyond the performance of thermometers commonly available in the laboratory. We use this technique because it is the only approach that allows characterization of references that are more accurate than the common references available in our laboratory.

The beat frequencies of two different dual-resonator devices, with the same design, were simultaneously measured while operated side-by-side inside an oven. A schematic diagram representing the above scenario is shown in Fig. 3.12, where the input x(t) is the temperature inside the oven causing the same temperature effect in both devices. The output of the two devices $y_1(t)$ and $y_2(t)$ contains the inherent noises $n_1(t)$ and $n_2(t)$ of the sensors, respectively. By estimating the cross correlation between the two output measurements, the inherent noise can be extracted. The true resolution of the temperature sensor is limited by its inherent noise.

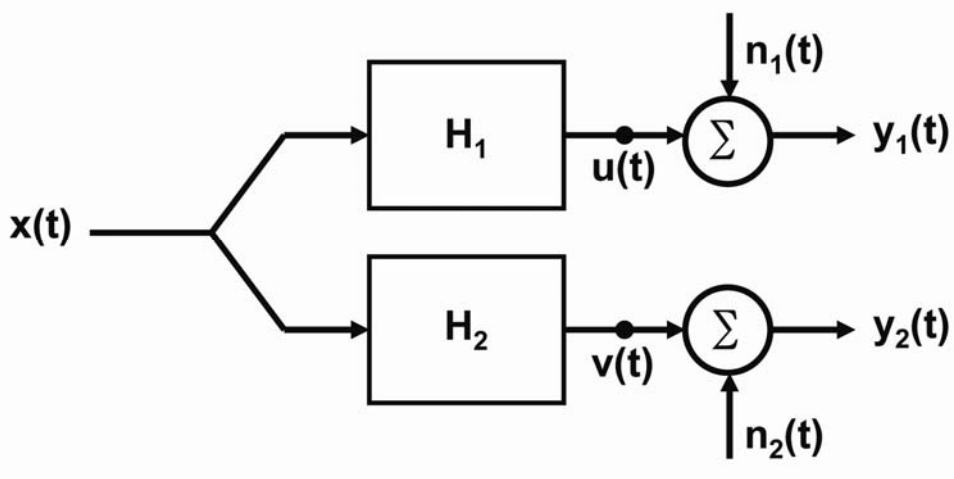

Fig. 3.12: Block diagram showing the modeling of correlation technique.

The inherent noise of the sensor is nothing but the variance of the noise n_1 ($C_{n_1n_1}$) or n_2 ($C_{n_2n_2}$). It is assumed that the noises of the two devices are uncorrelated, that is

$$C_{xn_1} = C_{un_1} = C_{xn_2} = C_{vn_2} = C_{n_1n_2} = 0 \tag{3.9}$$

From the Fig. 3.12, we can write [74], [75]

$$C_{y_1y_1} = C_{uu} + C_{n_1n_1} = |H_1|^2 C_{xx} + C_{n_1n_1} \tag{3.10}$$

$$C_{y_2y_2} = C_{uu} + C_{n_2n_2} = |H_2|^2 C_{xx} + C_{n_2n_2} \tag{3.11}$$

$$C_{y_1y_2} = C_{uv} = |H_1| * |H_2| C_{xx} \tag{3.12}$$

where $C_{y_1y_2}$ is the covariance between y_1 and y_2, $C_{y_1y_1}$ and $C_{y_2y_2}$ is the variance of y_1 and y_2 respectively. $|H_1|$ and $|H_2|$ are the transfer function, in this case TCF's, of the sensor 1 and 2 respectively. An important term, called correlation coefficient $\rho_{y_1y_2}$ between the two measurements $y_1(t)$ and $y_2(t)$, is given by [74], [75]

$$\rho_{y_1y_2} = \frac{C_{y_1y_2}}{\sqrt{C_{y_1y_1} C_{y_2y_2}}} \tag{3.13}$$

From equations (3.9) to (3.13), the intrinsic noise in device 1 can be derived as

$$C_{n_1n_1} = C_{y_1y_1} \left[1 - \rho_{y_1y_2} \frac{|H_1|^2}{H_1 * H_1} \sqrt{\frac{C_{y_2y_2}}{C_{y_1y_1}}} \right] \tag{3.14}$$

For the dual resonator, the second term in the bracket in equation (3.14) results into approximately $\rho_{y_1 y_2}$ and hence the noise variance can be simplified as

$$C_{n_1 n_1} \approx C_{y_1 y_1}[1 - \rho_{y_1 y_2}] \tag{3.15}$$

In terms of deviation, equation (3.15) becomes

$$\sigma_{n_1 n_1} = \sigma_{y_1 y_1}\sqrt{[1 - \rho_{y_1 y_2}]} \tag{3.16}$$

where $\sigma_{y_1 y_1}$ is the deviation in the output signal of device 1 and $\rho_{y_1 y_2}$ is the correlation coefficient between the measured signals of the two devices. Measurements of f_{beat} of both devices were taken over a period of 10 hours. As can be seen in Fig. 3.13, both signals are tracking the small variations in the temperature inside the oven (~ 0.3 °C), and that most of the variations in the individual signals are present in both sensors.

Since the resonator based oscillators can have various types of noise other than white noise, an IEEE recommended Allan deviation [76] has been used to calculate the deviation in the measurements. The classical standard deviation for such measurements depends on the number of data points and hence may not converge [76]. However, if the oscillator exhibits only white noise then the Allan deviation and the classical standard deviation will give the same result.

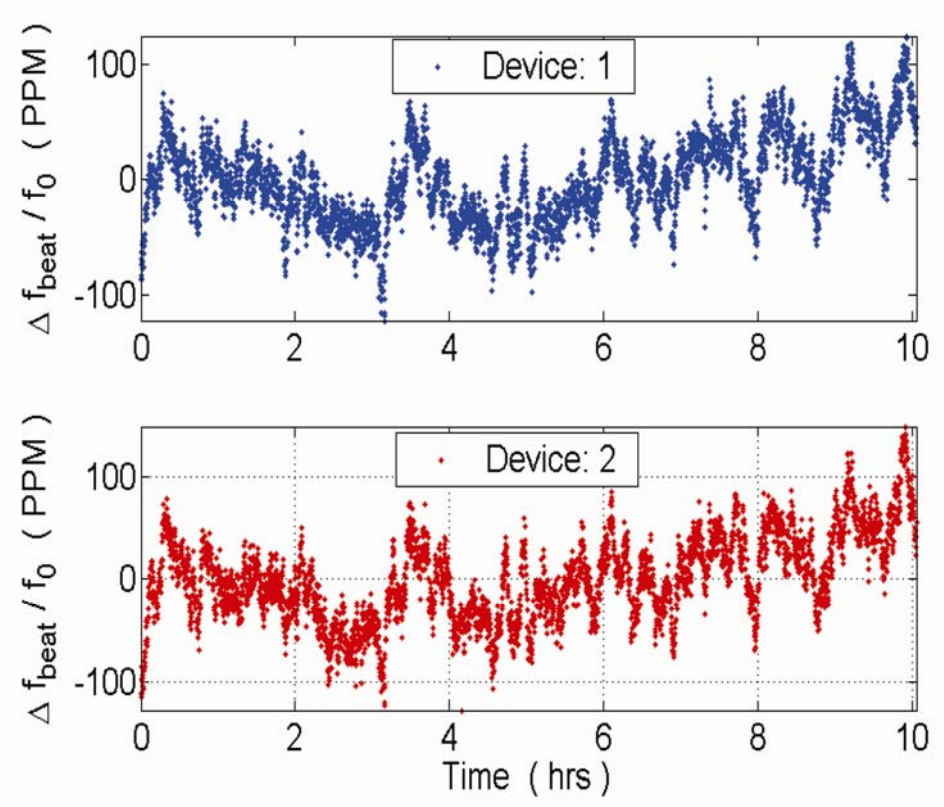

Fig. 3.13: Measurement of the beat frequencies of the two different dual-resonator devices at a nominally constant temperature. Both devices were kept inside an oven side-side and the oven was maintained at a nominally constant temperature of 60°C.

The Allan deviation, for an averaging time τ of one second, can be estimated as

$$\sigma_y(\tau) = \sqrt{\frac{1}{2(N-1)}\sum(y_{i+1} - y_i)^2} \tag{3.17}$$

where y_i are the discrete frequency measurements averaged over time τ.

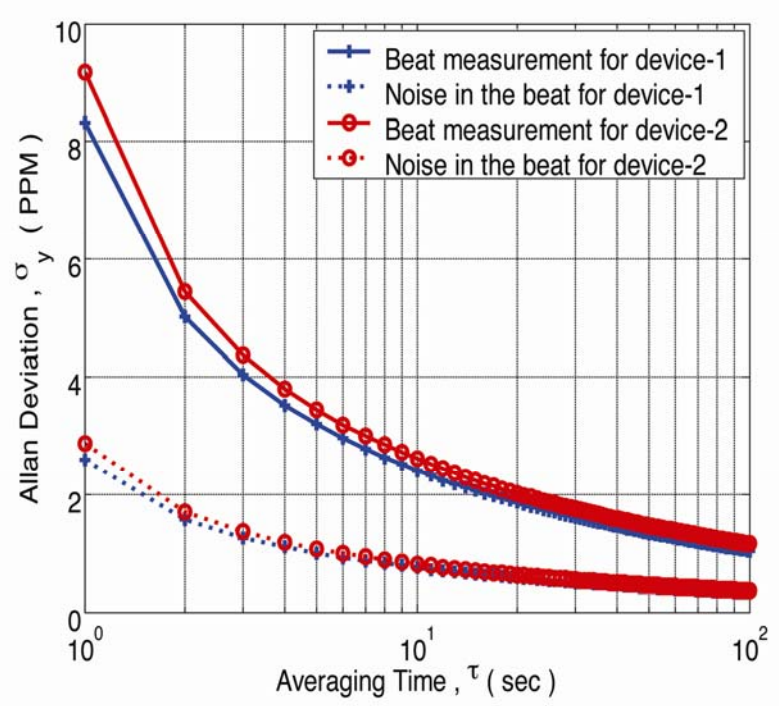

Fig. 3.14: Evaluation of the Allan deviation of the measured beat frequency data and its noise.

Ignoring the dead time between the two consecutive measurements, the Allan deviation for multiple τ can be evaluated by simply averaging the consecutive frequency data, as shown in Fig. 3.14. The correlation coefficient of the two beat frequencies is calculated to be 0.90. From Eq. (3.16) we can compute the noise component of the beat frequency as a function of the averaging time τ, as shown in Fig. 3.14. By knowing the sensitivity of the beat frequency and its noise component, the resolution of the dual-resonator beat frequency thermometer can be evaluated and is illustrated in Table I. From these measurements, we find that the resolution of the beat frequency thermometer is 0.008°C for a 1 s averaging time and as low as 0.0023 °C for a 10 s averaging time.

Table 3.1: Allan deviation and resolution of the beat frequency measurements.

	f_{beat} (KHz)	TCf_{beat} (ppm)	σ_y for the noise (ppm)		Resolution (°C)	
			τ = 1s	τ = 10s	τ = 1s	τ = 10s
Device-1	**75**	**360**	**2.9**	**0.81**	**0.0081**	**0.0023**
Device-2	**62**	**330**	**2.6**	**0.75**	**0.0079**	**0.0023**

It should be mentioned here that the analysis described above only estimates the resolution of the beat frequency thermometry and not its accuracy. There is a difference between the accuracy and the resolution of a sensor. The accuracy of the sensor is the difference between the measured value and the true value. An accurate sensor gives the output value which is very close to the true value. However, the resolution of a sensor is the minimum deviation that can be measured by the sensor. For example, the above beat frequency temperature sensor can measure temperature deviation of as low as 0.008°C for a 1 s averaging time. If we increase the averaging time to 10 s, the sensor noise tends to cancel out and it is possible to measure the deviation of 0.002°C.

3.7 Conclusions

A temperature sensor with such resolution can be exploited for various in-chip applications. However, one of the most important applications is the temperature compensation of the micromechanical resonator to achieve sub-ppm frequency stability. The temperature compensation is done by sensing the temperature of the resonator and

then stabilizing the frequency by using feedback control logic. Since the dual-resonator beat frequency thermometry is inherent to the resonator, this technique of temperature sensing is ideal for the temperature compensation of micromechanical resonators. Similar techniques have been used in the past to achieve the frequency stability of the order of 10^{-9} in the quartz resonators.

Significant improvements in the performance of this sensor are possible by designing high-frequency low phase noise dual resonators, resulting in a sensor resolution of better than 0.001 °C, which would enable significant improvements in temperature compensation of a very wide spectrum of analog and digital systems. It is also possible to enhance the temperature sensitivity of the beat frequency by more closely matching the initial frequencies of the two resonators. In the example demonstrated here, the mismatch between frequencies is of the order of 6% and arises from fabrication uncertainties in our process. A more stable process executed in a CMOS manufacturing line can be expected to achieve frequency matching to better than 1%, resulting in a very high temperature sensitive beat frequency, leading to improved performance of the sensor in measuring the smallest change in temperature above its resolution.

Now that we have found the technique for a lag-free thermometry, we need to come up with a method for an efficient thermal isolation of the resonator. Next chapter describes an in-built heater based thermal isolation technique.

Chapter 4

Thermal Isolation of MEMS Resonator

This chapter presents an in-chip thermal-isolation technique for a micro-ovenized microelectromechanical-system resonator using a single DETF resonator. Resonators with a micro-oven can be used for high precision feedback control of temperature to compensate for the temperature dependence of resonator frequency over a wide temperature range. However, ovenization requires power consumption for heating, and the thermal time constant must be minimized for effective temperature control. We demonstrate an efficient local-thermal-isolation mechanism, which can reduce the power requirement to a few milliwatts and the thermal time constant to a few milliseconds. In this method, the mechanical suspension of the resonator is modified to provide thermal isolation and include an integrated resistive heater. This combination provides mechanical suspension, electrical heating, and thermal isolation in a compact structure that requires low heating power and has a small thermal time constant. A power consumption of approximately 12 mW for a 125 °C temperature rise and a thermal time constant ranging from 7 to 10 ms is reported here, which is approximately 20x and 50x, respectively, lower than the un-isolated MEMS resonator and several orders of magnitude lower than that of the commercially available ovenized quartz resonators. A CMOS-compatible wafer-scale encapsulation process is used to fabricate this device, and the thermal-isolation design is achieved without any modification to the existing resonator fabrication process.

4.1 Introduction

Currently, oven-controlled quartz resonators are used to generate high-precision frequency references suitable for high-end industry and military standards [13] – [17]. As explained in chapter 2, in this method the resonator is held at a fixed temperature to compensate for the temperature dependence of the resonator frequency. The extent to which the resonator is heated depends on the difference between the set point and the ambient temperature. For an ovenized resonator that is required to operate within a temperature range of −40 ℃ to 85 ℃, the heating has to cover a range of 125 ℃. Due to the large volume of a conventional quartz-crystal oscillators, which can be up to 1000 mm^3 [17], the power consumption for heating can be as much as 10 W with a warm-up time of approximately 30 min [17], [18], [77], where a warm-up time is defined as the time required for an oscillator to reach a pre-defined frequency stability. MEMS technology offers miniaturization to submillimeter scales, which can provide substantial power reduction [22], [53] – [55], through a micro-oven design.

A micro-oven, in general, constitutes a heater for joule heating and thermal isolation for reducing heat loss. Micro-oven designs for MEMS devices have been reported before with few milliwatts of power consumption and a time constant in milliseconds [53] – [55]. In these designs, a MEMS structure is suspended on a microplatform. The microplatform is thermally isolated from the substrate and contains separate heater and sense resistors. Although promising, these designs have limitations in terms of lack of mechanical stiffness, large thermal mass, and complex fabrication processes. This work

describes a miniature thermal-isolation design, which achieves a small thermal time constant with low power consumption. The designs illustrated here are compatible with our previously published "epi-seal" wafer-scale encapsulation process [57] – [58]; and all its advantages, such as low leak rate, no requirement for a getter, long-term stability [48], and low-cost manufacturing, are maintained. Designs for thermal isolation with various heating methods will be discussed and compared, before presenting the experimental results of the miniature local-thermal-isolation design.

4.2 Designs for Thermal Isolation

In this section, first we will discuss about the case with an external heater where the entire chip gets heated up, and then we will focus on the local thermal isolation with the comparison between two.

4.2.1 Heating Entire Chip for Temperature Control

Thermal isolation of the ovenized device from the surroundings is required to prevent heat loss during temperature control. It is therefore essential to thermally isolate the heater from the ambient but, at the same time, have minimum heat loss between the heater and the resonator. Hence, it is highly desirable to place the heater as close to the resonator as possible. An added constraint is to achieve this thermal isolation without modifying the existing fabrication process of the resonator. A double-ended tuning-fork (DETF)-type single resonator, encapsulated within a silicon die (chip), is used here (Fig. 4.1).

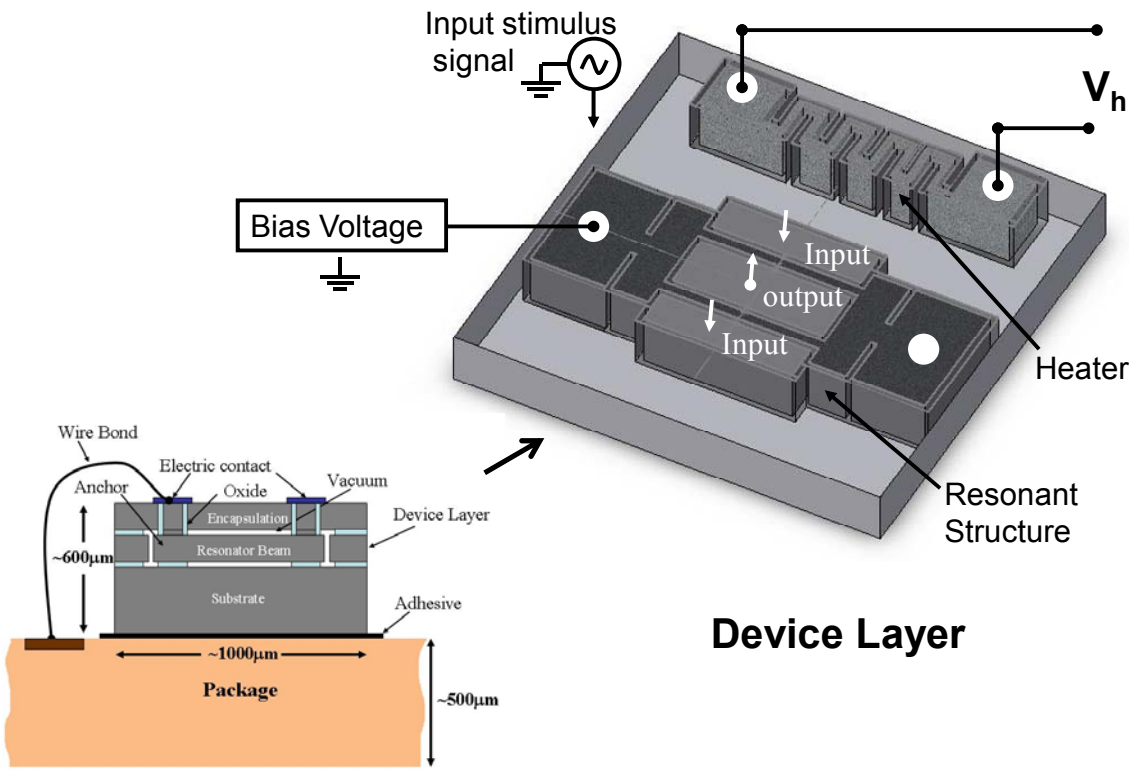

Fig. 4.1: Schematic of a typical MEMS resonator chip attached to a package with adhesive.

The chip is attached to the package using an adhesive and wire-bonded to make electrical contacts. Heating resistors are placed in the device layer (Fig. 4.1) in the vicinity of the resonant structure. The DETF is designed for flexural-mode actuation, as shown in Fig. 4.2. The biased resonator beams are electrostatically actuated by providing an alternating stimulus signal to input electrode. The capacitive transduction between the beams and the input electrodes cause the resonator to vibrate. A resonance occurs when the frequency of the input stimulus signal becomes equal to the natural frequency of the flexural mode of the beam. The output signal is then amplified to measure the resonant frequency.

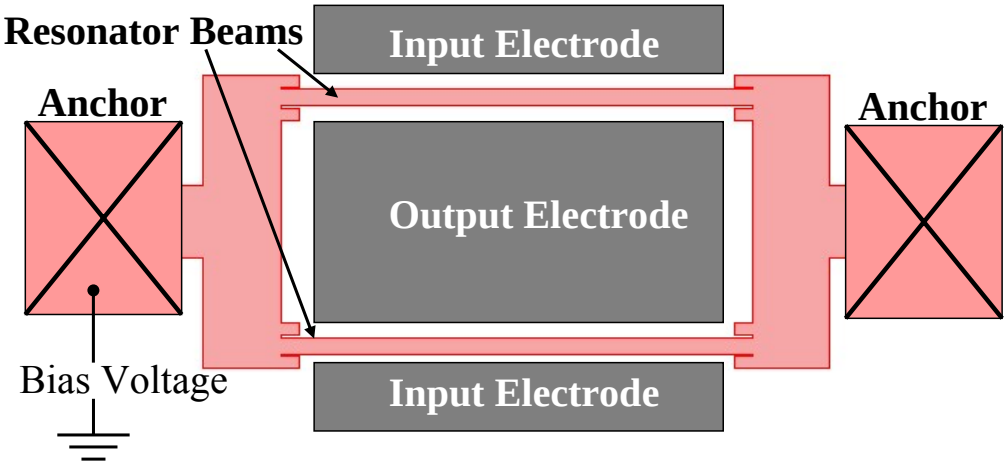

(a)

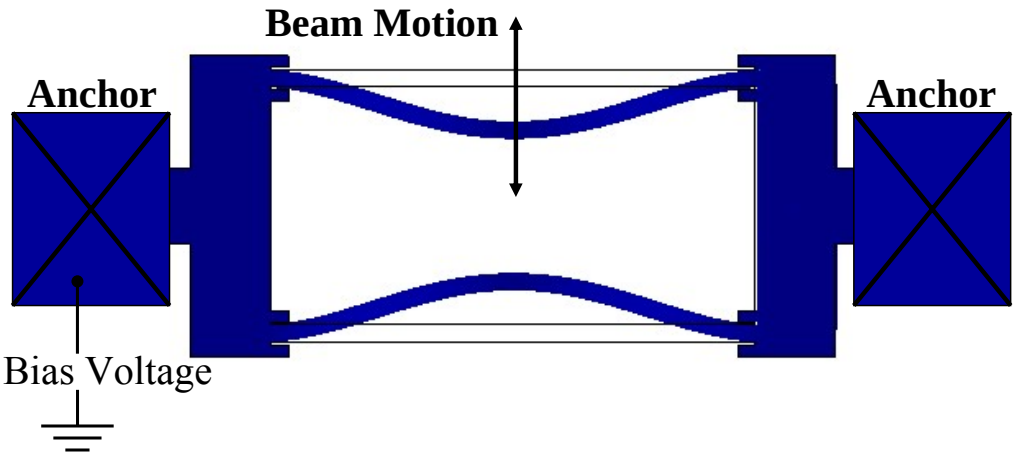

(b)

Fig. 4.2: (a) Top view schematic of a standard un-isolated DETF-type resonant structure showing input and output electrodes. (b) FEM simulation of flexural-vibration mode of a DETF (exaggerated view).

The power consumption and the thermal time constant can be estimated by using a simple 1-D lumped-parameter thermal model [78], [79]. The expression for conductive thermal resistance is given by

$$R_{th} = \frac{l}{kA_c} \tag{4.1}$$

where k is the thermal conductivity, l is the length, and A_c is the area of cross-section.

Thermal capacitance can be evaluated as

$$C_{th} = \rho V' c_p \tag{4.2}$$

where ρ is the density, V' is the volume, and c_p is the specific heat capacity at constant pressure.

Radiative and convective thermal loss can be found by

$$R_{rad} = \frac{1}{h_{rad}A_s}$$

$$R_{conv} = \frac{1}{h_{conv}A_s} \tag{4.3}$$

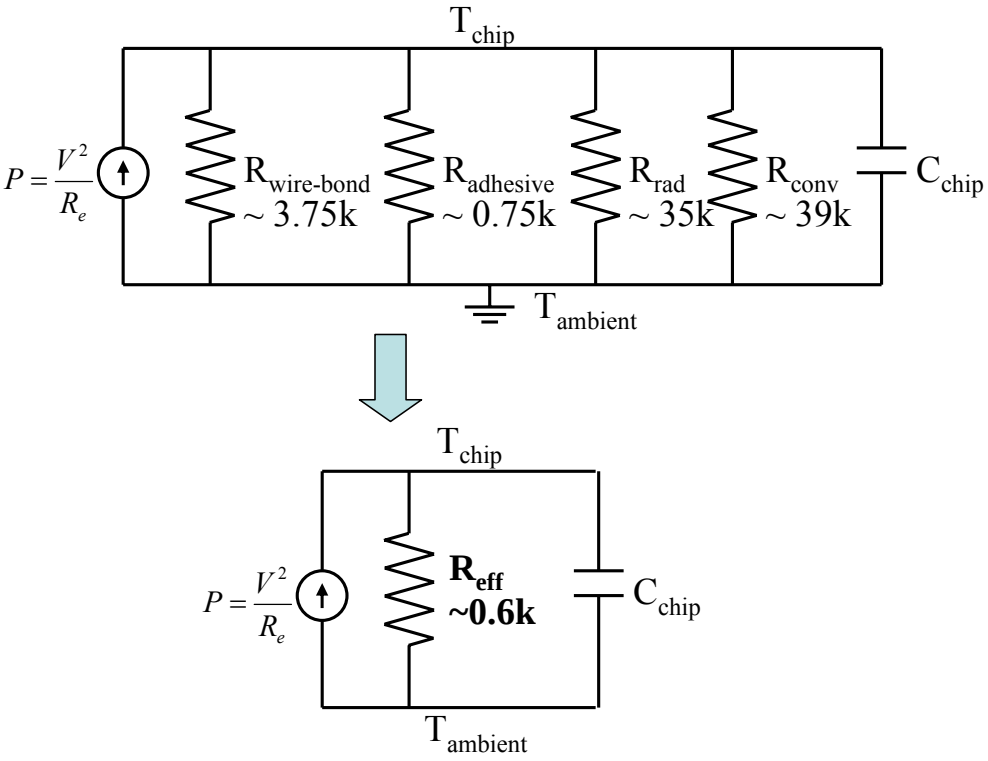

Fig. 4.3: Thermal equivalent circuit. Package is assumed to be at ambient temperature. Unit of thermal resistances shown above in Kelvin per Watt.

where $h_{rad} = \epsilon\sigma(T_s + T_{surr})(T_s^2 + T_{surr}^2)$ is the linearized radiation-heat-transfer coefficient [78]. T_s is the surface temperature, and T_{surr} is the surrounding temperature. The h_{conv} is the convective-heat-transfer coefficient, and A_s is the surface area. Fig. 4.3 shows the equivalent thermal-resistance circuit, where P is the input power. Approximate values for the material constants are taken from the literature [60], [80] – [82].

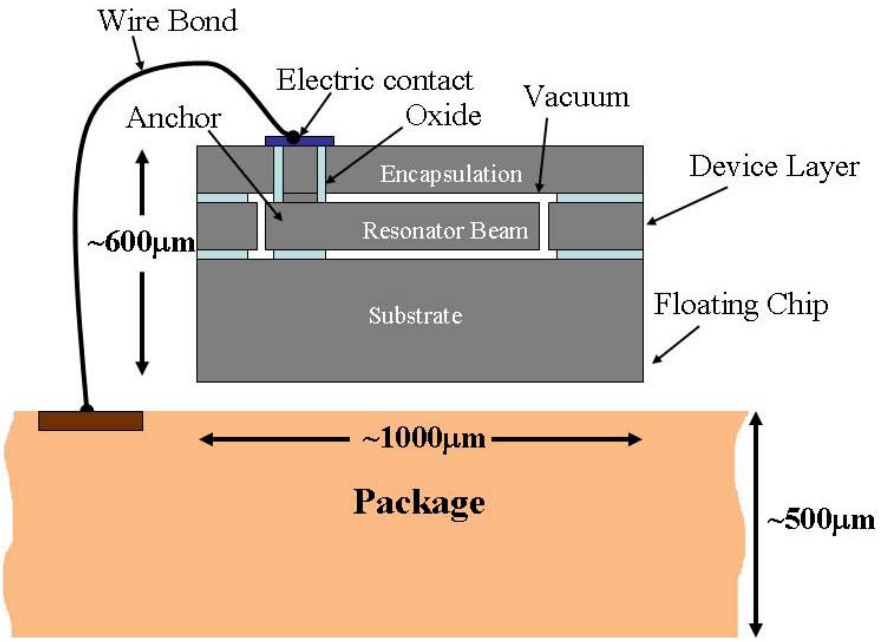

Fig. 4.4: Floating chip without any adhesive at the bottom to increase the thermal resistance.

In this design configuration of the MEMS chip, the thermal resistance calculated for the device layer and the chip (~20 K/W) is very small as compared to that of wire bond and adhesive. It is therefore assumed that the entire chip, including the resonator, is approximately at a constant temperature. It is also assumed that the package acts as a heat sink, and hence, its temperature is the same as the ambient temperature. The total effective thermal isolation R_{eff} is estimated to be approximately 600 K/W. The power required to achieve a ΔT rise in temperature of the resonator can be found by

$$P = \frac{V^2}{R_e} = \frac{\Delta T}{R_{eff}} \tag{4.4}$$

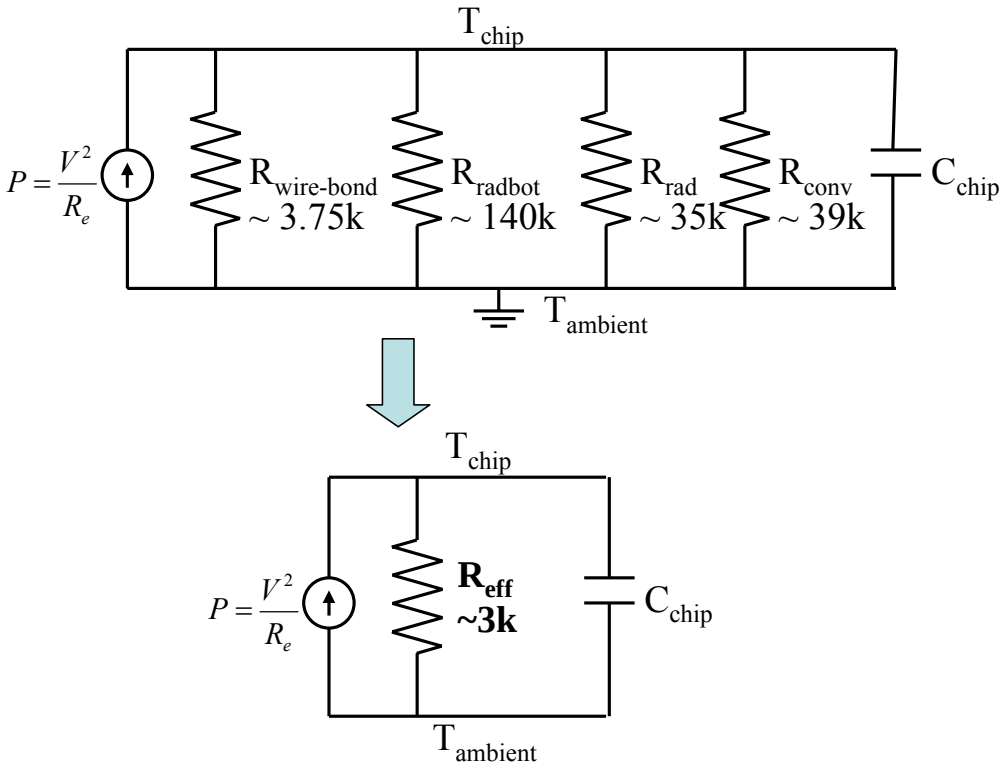

Fig. 4.5: Thermal equivalent circuit when there is radiative heat loss from the bottom of the chip R_{radbot} in the absence of the adhesive. Unit of thermal resistances shown above is in Kelvin per Watt.

To obtain ΔT of 125 $^{\circ}C$, the input power is approximately 200 mW. The thermal time constant can be estimated by equation (4.5) and is approximately 500 ms.

$$\tau = R_{eff} C_{th} \tag{4.5}$$

One method to improve thermal isolation is to release the chip from the package by removing the adhesive and keep it floating in air (Fig. 4.4), thus reducing the heat loss

from the substrate to the package. The chip, in this case, is supported from the top by six wire bonds. The equivalent thermal circuit for the released device is shown in Fig. 4.5, and the total effective thermal isolation is estimated to be approximately 3000 K/W—an improvement by a factor of five.

This method of improving thermal resistance is effective but not robust and may lead to packaging problems. Furthermore, since the heat transfer from the heater to the resonator takes place in the device layer, the device layer gets heated which leads to unwanted heating up of the entire chip because of the lack of thermal isolation between the device layer and the substrate. The thermal mass of a typical resonator chip is approximately 1200 times larger than that of a single DETF, and hence, heating of the entire chip leads to longer thermal time constant and more heat loss resulting in increased input power.

4.2.2 Heating Resonator Alone With Local Thermal Isolation

Therefore, it is desired to have an alternative technique to increase the heating efficiency by heating only the resonator and simultaneously providing large thermal isolation between the resonator and its immediate vicinity in the device layer. This calls for a local heat delivery and thermal-isolation mechanism. This can be achieved by designing a resonator coupled with an in-built heater and restricting the heat loss to the

ends of the heaters. The in-built heater, in this configuration, serves the dual purpose of heating as well as thermally isolating the DETF. To design a resonator for good thermal isolation, it is necessary to study various heat-loss mechanisms in the structure. The resonator is encapsulated, and the atmosphere inside the encapsulation consists mainly of hydrogen gas at a low pressure of approximately 1 Pa [57]. The three modes of heat transfer considered here are as follows:

1) Convection due to hydrogen molecules in the cavity;

2) Radiation from the resonator;

3) Conduction through the silicon beams of the in-built heater.

Convection due to hydrogen molecules can be analyzed by using microscopic-particle-based kinetic theory of heat diffusion [83]. Thermal conductivity of molecular-energy carriers can be evaluated as

$$k_h = \frac{1}{3} C v \Lambda \tag{4.6}$$

$$where, \quad C = \frac{3}{2} k_B n_M$$

$$v = \sqrt{\frac{8 k_B T}{\pi m}}$$

C is the specific heat at constant volume per unit volume, υ is the velocity of the energy carrier, k_B is the Boltzmann constant, n_M is the molecular number density, T is the temperature, and m is the molecular mass of the energy carrier.

It is assumed that the mean free path Λ is equal to the gap width of the cavity (1.5 μm) because of low pressure. The thermal conductivity due to the hydrogen molecules k_h is estimated to be around 1×10^{-6} W/m/K at room temperature, resulting in an effective thermal resistance of the order of 1×10^{7} K/W and, hence, can be assumed that the heat loss due to molecular conduction is negligible as compared to other modes.

The thermal resistance due to radiation for a DETF structure, assumed to be at a maximum heating temperature of 425 K, is estimated to be approximately 1×10^{6} K/W. Hence, for simplification, it is also assumed that the heat loss due to radiation is relatively small and can be neglected.

It is, therefore, the conductive heat transfer through the silicon beams which is the dominant heat-loss mechanism in this encapsulated MEMS resonator. If a current-carrying resistive heater of constant cross section is analyzed, the temperature profile along the length of the heater, in the absence of convection and radiation heat loss, is given by (4.7) [78], [79] and shown in Fig. 4.6.

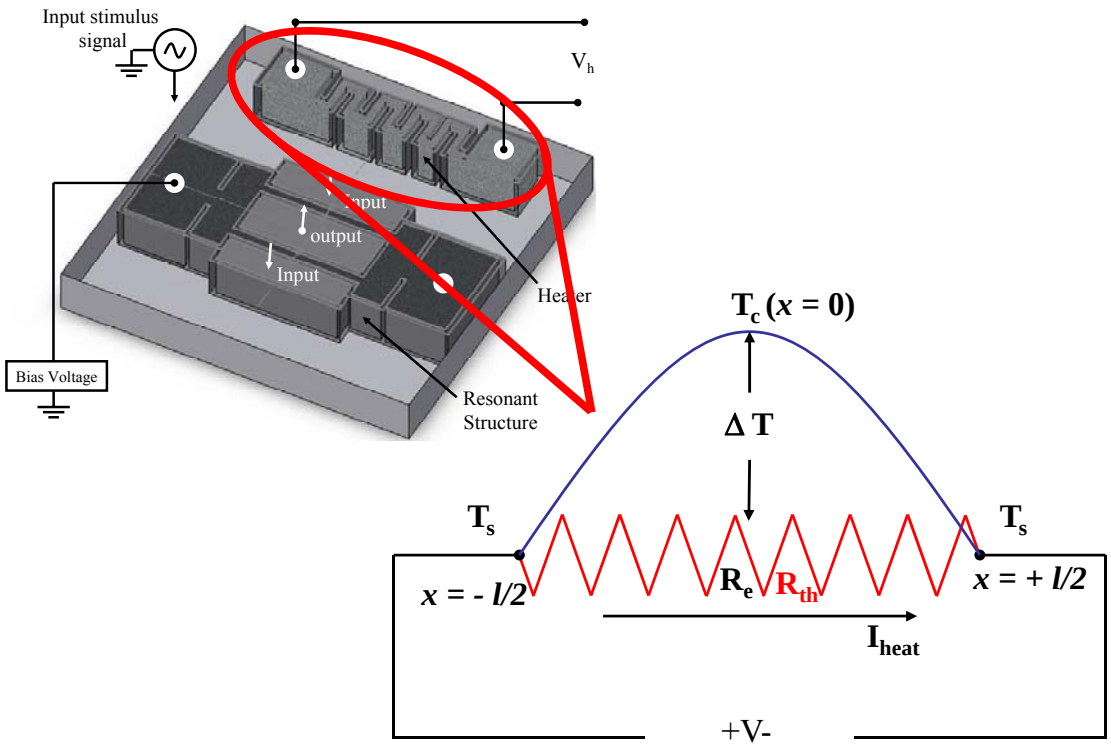

(a)

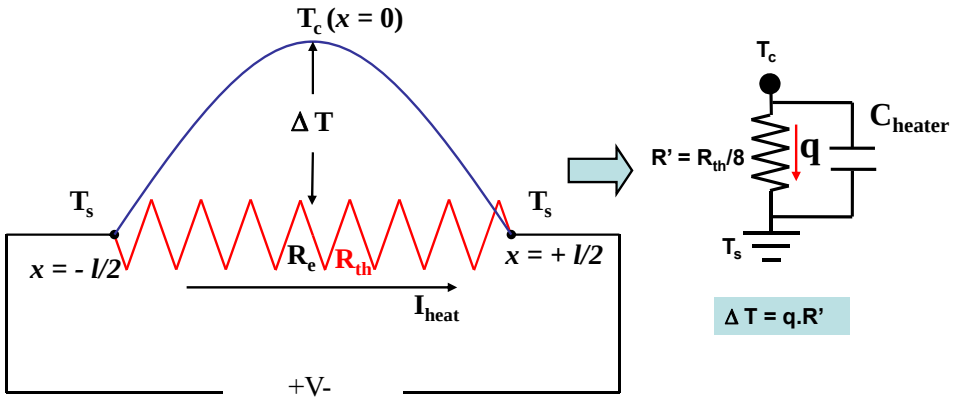

(b)

Fig. 4.6: (a) Temperature profile along the length of a current-carrying resistive heater having thermal resistance of R_{th} and electrical resistance of R_e. (b) The continuous temperature profile and its approximate equivalent lumped model.

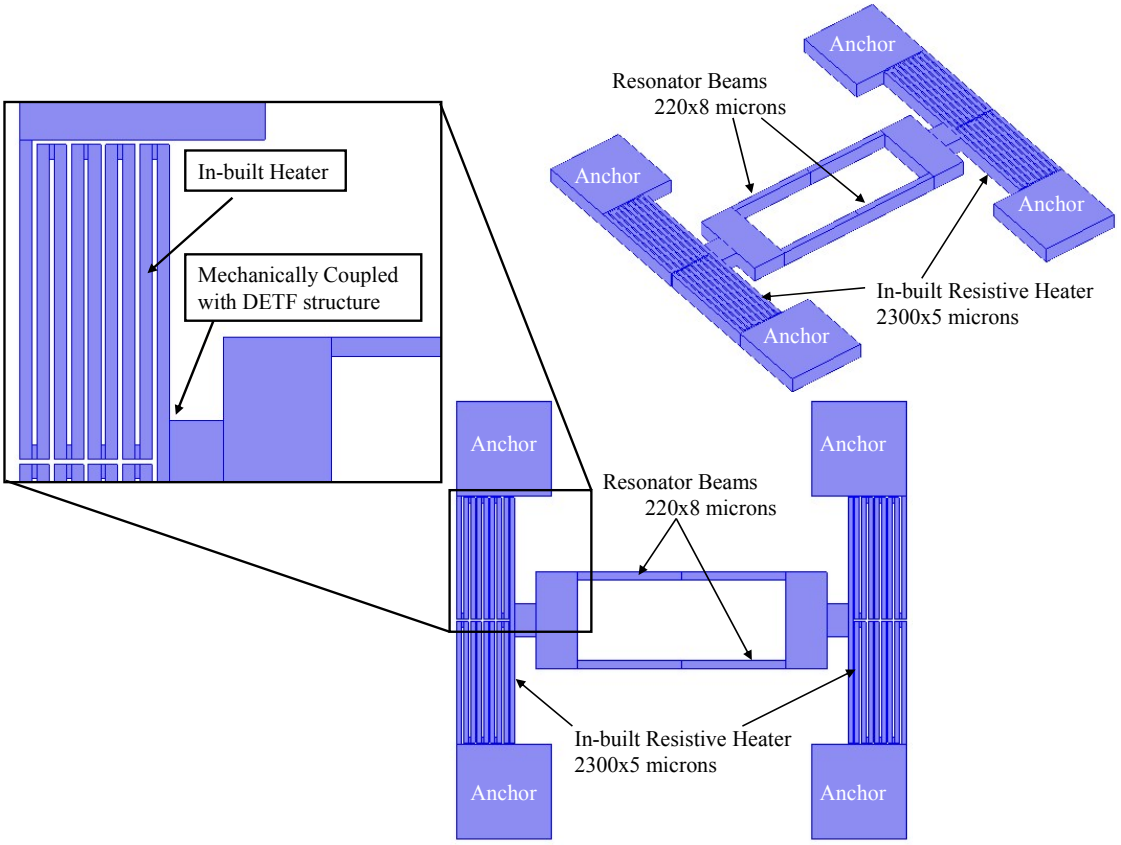

Fig. 4.7: Resonator design with local thermal isolation. The heater is in-built to the DETF such that the resonant structure is attached at the center of the heater. The entire structure is released except at the four anchors.

$$T_x = \left(\frac{q'l^2}{8k}\right)\left(1 - \frac{4x^2}{l^2}\right) + T_s \qquad (4.7)$$

where x varies from $-l/2$ to $+l/2$, and T_s is the end surface temperature of the heater (Fig. 4.6). The maximum temperature occurs at the center of the heater (at $x = 0$) and is given by

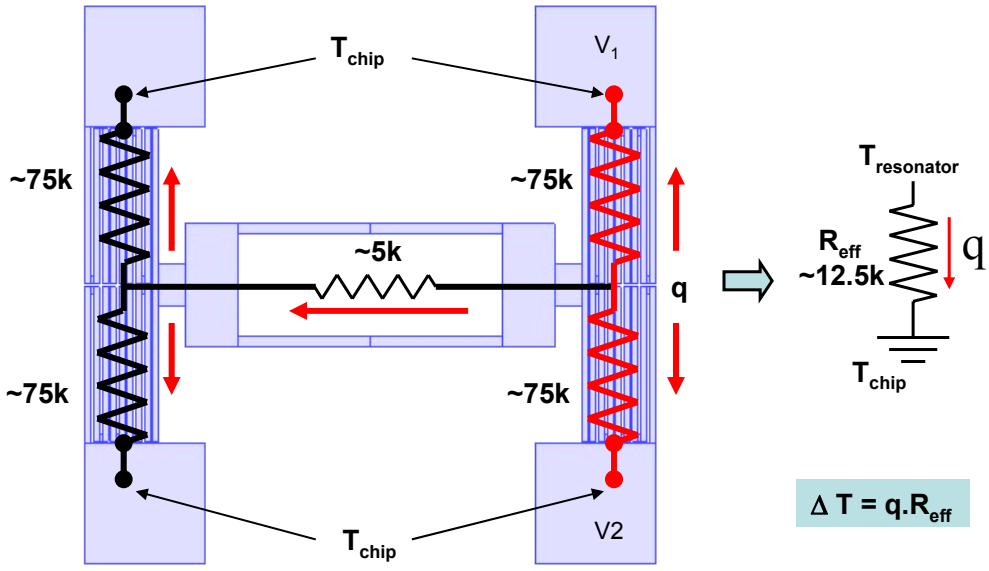

Fig. 4.8: One dimensional resistor network to estimate the total effective thermal resistance of the in-built heater. Equation (4.10) is used for the estimation of effective thermal resistance R_{eff}.

$$T_c = \left(\frac{q'l^2}{8k}\right) + T_s \tag{4.8}$$

The expression for the rise in temperature at the center of the heater, with respect to its end surface, can be written as

$$\Delta T = T_c - T_s = \left(\frac{q'l^2}{8k}\right) = \left(\frac{V^2}{R_e}\right)\left(\frac{R_{th}}{8}\right) = qR' \tag{4.9}$$

$$where\ q' = \frac{q}{lA} = \left(\frac{V^2}{R_e}\right)\left(\frac{1}{lA}\right)$$

From the equation (4.9), we can establish an equivalence between a current carrying beam having thermal resistance of R_{th} and heat generation of q with a lumped model having thermal resistance of $R^{'}$ and heat flow of q for the same rise in temperature, where $R^{'}$ is eight times smaller than R_{th}. This suggests that the heating efficiency can be maximized if the resonator is attached at the center of the heater and that, in order to achieve the maximum temperature rise at the center of the heater for a given input power, the thermal resistance of the heater should be as large as possible.

However, the micro-ovenized resonator design is suspended from both ends by in-built resistors (Fig. 4.7 and 4.8), so the expression for the temperature of the resonator due to heating power applied to one end of the resonator must take into account the heat loss through the other end of the resonator. Using the equivalent thermal resistance from equation (4.9), we can estimate the resonator temperature by considering the second resistor in parallel with the heater resistor (Fig. 4.8). In this case, an approximate expression for the rise in temperature at the center of the heater, with respect to its end surface, can be written as

$$\Delta T \sim \left(\frac{V^2}{R_e}\right)\left(\frac{1}{\frac{1}{(R_{th}/8)}+\frac{1}{(R_{th}/4)}}\right) = \left(\frac{V^2}{R_e}\right)\left(\frac{R_{th}}{12}\right) = qR_{eff} \qquad (4.10)$$

From the equation (4.10), for a resonator with a heating resistor with internal heat generation of q at one end and an insulating resistor with no heat generation at the other end, both having thermal resistance of R_{th}, we can establish an equivalent lumped element model with a thermal resistance of R_{eff} and heat flow of q for the same rise in temperature, where R_{eff} is 12 times smaller than R_{th}. This relationship allows us to easily predict the resonator temperature for a given heating power, although the prediction is not exact because the temperature distribution on the heater is modified by the heat flow across the resonator.

Finite-element simulations (Fig. 4.10) and measurements indicate that equation (4.10) overestimates the resonator temperature by about 20%.

The layout of the thermally isolated DETF with two in-built heaters is shown in Figs. 4.7 and 4.8. The cross section of each heater beam is 5 by 20 μm, and its total length is approximately 2300 μm. The resonator is attached at the center of the heater for maximum heating. The entire structure is released except at the four anchors which act as mechanical supports at the bottom and provide electrical contacts at the top. The anchors are electrically insulated by silicon dioxide (see Fig. 1(a)). The thermal resistance of the in-built heater R_{th} is approximately 150 000 K/W. Fig. 4.8 shows an equivalent lumped-capacitance model of the DETF with in-built heater. The effective thermal resistance R_{eff} of the micro-ovenized structure is calculated using equation (4.10) and is evaluated to be approximately 12 500 K/W, which is significantly larger

than the un-isolated designs. The thermal isolation of the resonator also leads to a reduced thermal time constant, because the effective thermal mass comprises only the mass of the DETF and the in-built resistors, as opposed to the entire silicon die described in the previous section. This means that there will be rapid heating and cooling of the resonator over and above the slower thermal response of the chip. A 1-D equivalent thermal-circuit model of the in-built heater is shown in Fig. 4.9. As with temperature, it is difficult to calculate the thermal time constant of the resonator precisely by a simple lumped-element model because of the complex temperature profile through the device, but we can make an estimate using the effective resistance of the heaters and the total thermal capacitance of the heaters and the resonator, as shown in equation (4.11) and (4.12).

$$\tau = R_{eff}\,(C_{resonator} + C_{heaters}) \tag{4.11}$$

$$\tau_{\text{chip}} \approx R_{eff\_ext}\,C_{chip} \tag{4.12}$$

Table 4.1: Power consumption and time-constant comparison

Design	Power required for 125 °C temperature increase	Estimated Thermal Time Constant
Bonded chip[1]	~ 200 mW	~ 500 ms
Suspended chip	~ 42 mW	~ 3000 ms
In-built heater	~ 12 mW	~15 ms

[1]Conventional Design

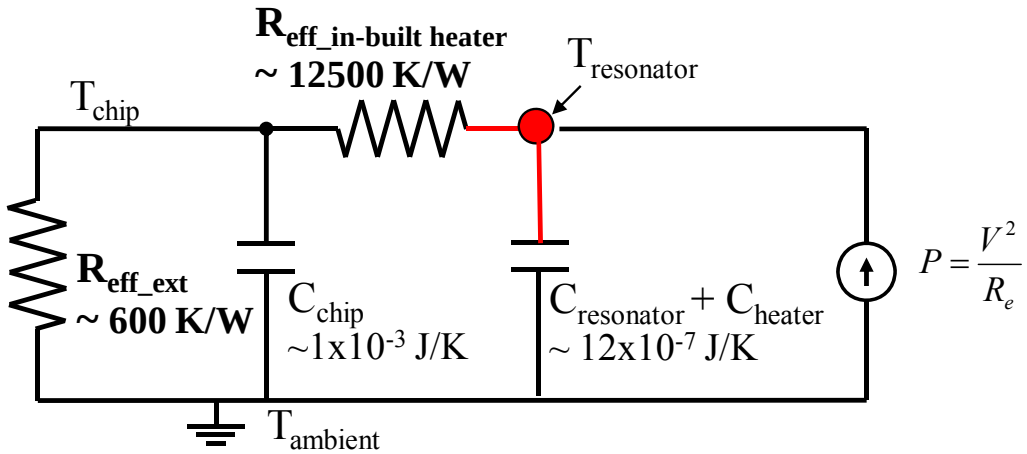

Fig. 4.9: Equivalent thermal circuit schematic for the resonator with in-built heater.

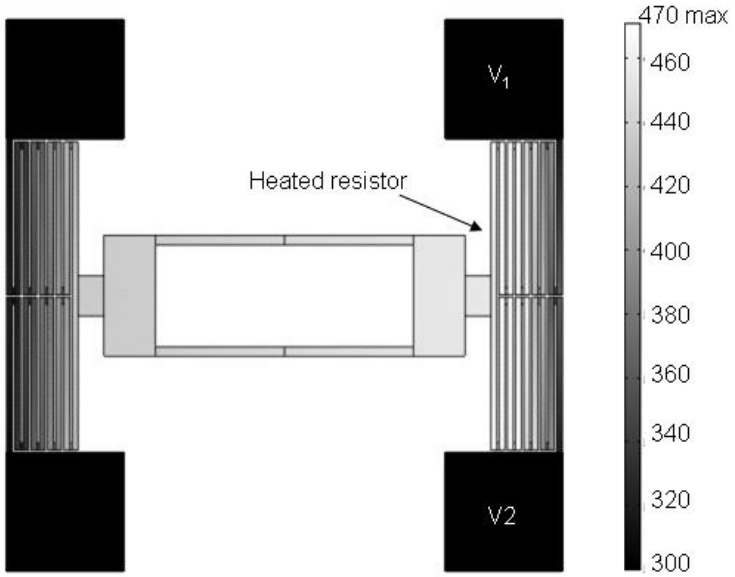

Fig. 4.10: Finite-element simulation of the thermally isolated DETF resonator showing the temperature distribution in Kelvin for a heating voltage of 6 V, which corresponds to 14 mW of heating power.

For the thermally isolated DETF, τ is estimated to be approximately 15 ms. The actual dynamic behavior of the device is characterized by multiple time constants from the nonheated resistor, the silicon die, and the resonator. Finite-element simulations indicate that the temperature change of the resonator itself may be up to 50% slower than the heaters.

A finite-element simulation was done to examine the temperature distribution along the length of the in-built heater and the DETF, as shown in Fig. 4.10. From the simulation, a power consumption of approximately 12 mW was required for a temperature increase of 125 °C. The time constant and heating power consumption of the three designs are compared in Table 4.1. Clearly, the in-built heater can be very effective, both in terms of reducing power consumption and dynamic thermal response.

4.3 Fabrication

One of the biggest advantages of this technique is with respect to fabrication. A CMOS compatible "epi-seal" encapsulation process [57], [58] is used to fabricate this device. The structure of the fabricated device is shown in Fig. 4.11. The device layer is insulated from the encapsulation layer by a thin sacrificial oxide, and openings for electrical contacts are made through the encapsulation layer over the anchors. Since the in-built heaters are in the device layer with the resonator, no changes to the fabrication process are required to create the thermally isolated DETF.

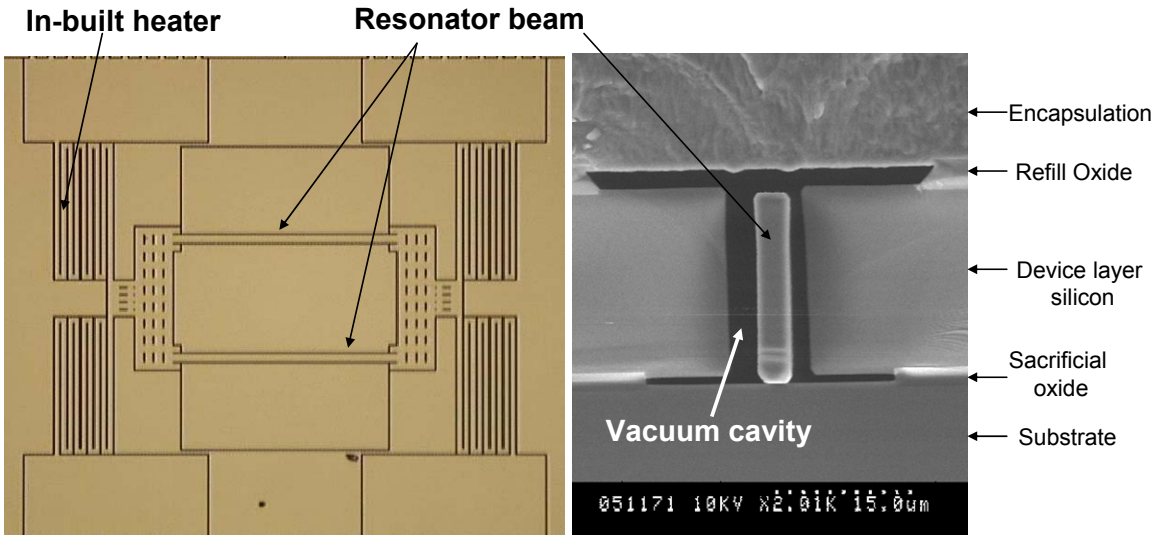

Fig. 4.11: (a) Optical image of the top view of the fabricated device before the deposition of the encapsulation layer. (b) SEM cross section of a resonator beam after the deposition of the encapsulation layer.

This process ensures a vacuum inside the encapsulation with a pressure of < 1 Pa. Long term (~1 year) stability of this vacuum condition has also been verified [48]. An optical image and a SEM cross section of encapsulated MEMS resonator with in-built heater is shown in Fig. 4.11.

4.4 Experimental Results

Resonators with 1.3-MHz frequency and a mechanical Q of approximately 10^4 were used for the experiment. Since silicon resonator frequency varies nearly linearly with temperature, frequency was used as a measure of temperature for this work. However, resonator frequency is also sensitive to bias voltage and axial strain. The bias voltage induces capacitive nonlinearity, which causes the effective stiffness of the resonator beam to decrease [84], reducing the resonator frequency. It is necessary to ensure that the bias voltage is not affected by the heating current. Fig. 4.12 shows the device layer schematic with circuit diagram of the resonator having in-built heater. Voltages V_1 and V_2 are applied, such that the potential difference between them acts as a joule heating voltage V_h across the in-built heater as shown in equation (4.13).

$$V_1 = V_b + \frac{V_h}{2}$$

$$V_2 = V_b - \frac{V_h}{2} \tag{4.13}$$

.

where, V_b is the effective bias voltage experienced by the resonator and V_h is the heating voltage applied across the heater.

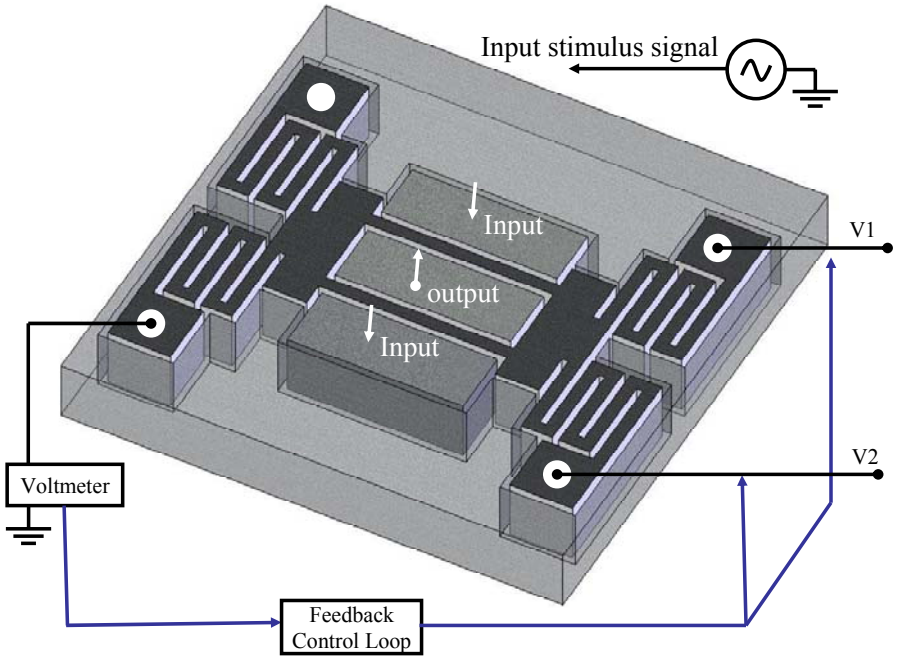

Fig. 4.12: Isometric view of device layer schematic showing the DETF with the in-built heater. A stimulus signal is applied to the input electrode. Heating voltages V1 and V2 are controlled using a feedback control loop to maintain a constant bias for the resonator.

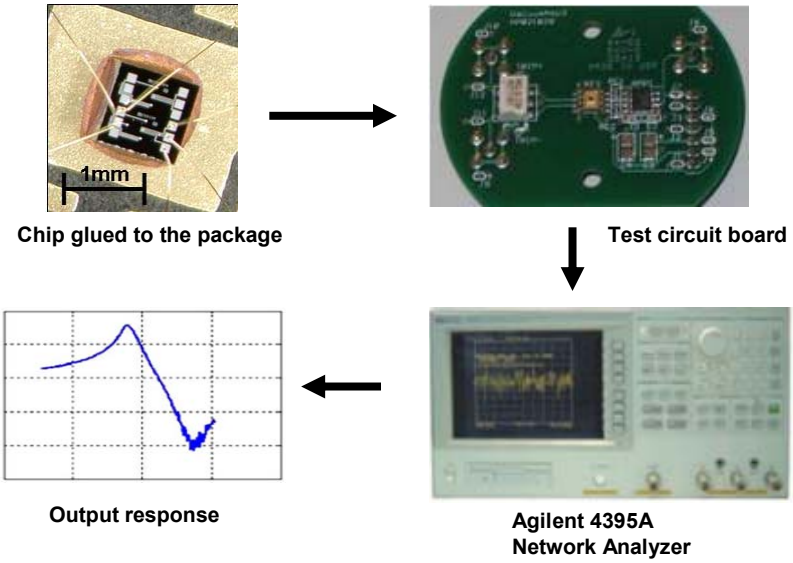

Fig. 4.13: Schematic of the test setup for frequency measurement.

Ideally, the resonator should see a constant bias voltage, because the portions of the in-built heaters, before and after the resonator, are nominally identical, but fabrication uncertainties result in asymmetry of the heaters that cause the bias voltage to change with the heating voltage. To remove the effect of this change in bias, a feedback-control loop was implemented to maintain a constant bias voltage on the resonator irrespective of the variable heating voltage (Fig. 4.12). The bias-control circuit had a compliance of 1.0 mV, which is equivalent to a < 0.1 ppm change in frequency. A schematic of the experimental test setup is shown in Fig. 4.13, and the results of the measurement are shown in Fig. 4.14.

4.4.1 Power Consumption

The DETF was heated using the in-built heater, and its frequency was measured as a function of input power. As shown in Fig. 4.14, the frequency decreases with the increase in input power as the temperature rises. The temperature rise was evaluated using the calibration data of frequency versus oven temperature (Fig. 4.15). It has been observed that there is a rise in temperature of approximately 125 °C with total power consumption of around 12 mW.

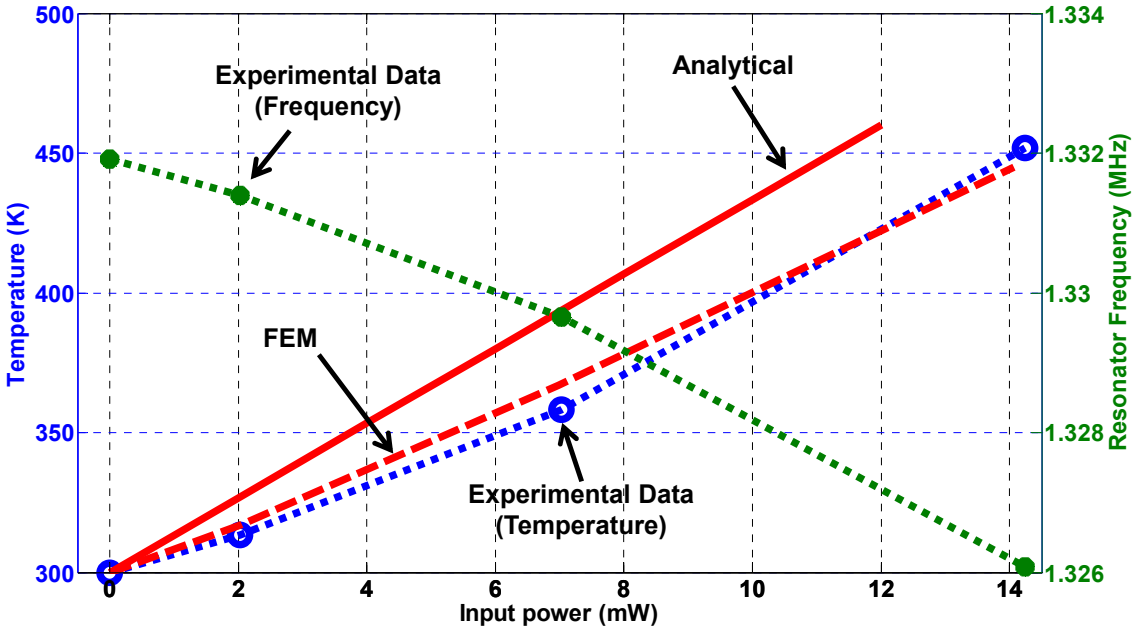

Fig. 4.14: Experimental data showing variation of resonator frequency due to joule heating of the in-built heater. The decrease in frequency (right y-axis) corresponds to a temperature rise (left y-axis) with increasing input power. Experimental results are compared with theoretical estimates. The analytical expression (10) estimates the temperature at the center of the in-built heater, while the FEM results are for the temperature at the center of the resonator.

The experimental output is observed to be slightly nonlinear as compared to the simulation results. This can be attributed to the fact that the material properties, including thermal conductivity and electrical resistivity of silicon, vary with temperature but were considered constant for the calculation.

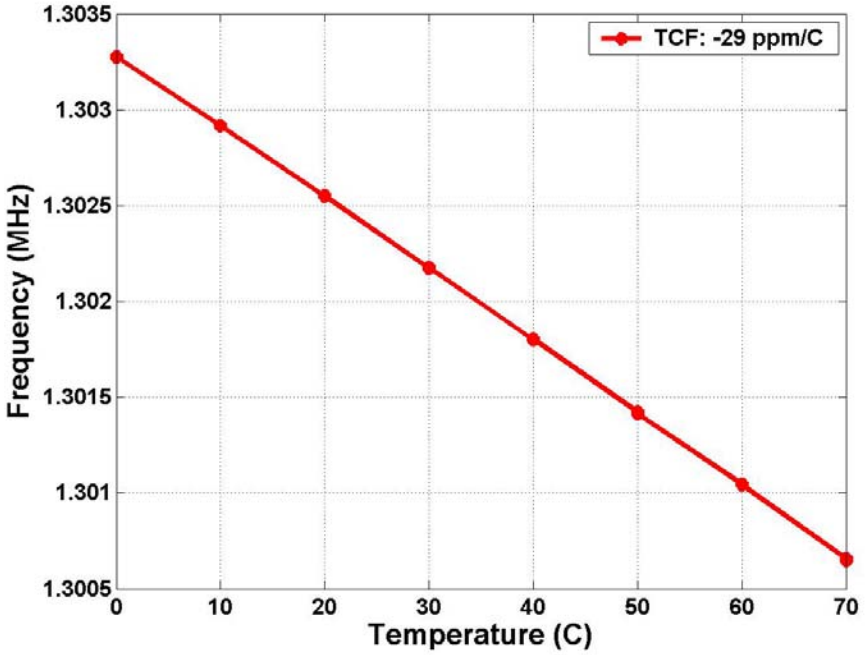

Fig. 4.15: Experimental data showing frequency – temperature characterization of the resonator with in-built heater. The resonator was kept inside an oven and the oven temperature was varied to find out the TCF of the resonator under no joule heating. The TCF of this resonator corresponds to that of a stress free single anchored resonator.

It should be mentioned that the stress due to differential thermal expansion of the device layer, the chip, and the package can create compressive axial strain on the DETF, leading to a shift in frequency. The natural frequency of the resonator beam in the presence of compressive axial force can be found using the following expression [85]:

$$f = \frac{(4.73)^2}{2\pi l^2}\left(1 + \frac{Pl^2}{EI\pi^2}\right)^{\frac{1}{2}}\left(\frac{EI}{m}\right)^{\frac{1}{2}} \tag{4.14}$$

The stiffness of the in-built heater is approximately 10 000X smaller than the resonator beams, and the resulting frequency error due to differential thermal expansion of the heater is estimated to be within 0.5% of the total change in frequency due to a temperature increase of 150 °C. Since the error is not large and we are interested in the approximate estimation of the power consumption, we ignore this error. The resonator was calibrated in a thermal chamber by measuring its frequency at different ambient temperatures with no power applied to the in-built heaters. The measured temperature coefficient of frequency was found to be nearly linear and equal to −29 ppm/°C (Fig. 4.15), which is approximately the same as that of a stress-free single-anchor silicon resonator [52], [64].

It is also necessary to check the influence of the in-built heater suspension on the mechanical quality factor (Q) of the resonator. Since the heater suspension is on both sides of the DETF, there is a linear temperature gradient across the length of the resonator beam. This gradient in temperature affects the Q. It has been shown [86] that the Q for a resonator with a linear temperature gradient and average temperature T_A will be slightly higher than the Q of a resonator with no temperature gradient and uniform temperature T_A. However, the temperature gradient has a minimal effect on the frequency–temperature calibration of the resonator.

4.4.2 Thermal Time Constant

The thermal time constant of the micro-ovenized resonator is an important parameter for temperature control. The thermal response was evaluated using a transient electrical-resistance measurement. A voltage pulse was applied to the heater, which caused its resistance to increase as it heated up. After the pulse ended, the heater resistance decreased as it cooled. A wheatstone bridge was used to measure the change in heater resistance during this cycle (Fig. 4.16). For the measurement, a heating pulse of 4.5 V was used, and the voltage was maintained at 0.5 V during the cooling period in order to observe the change in voltage during cooling.

The measured time constants of several resonators varied between 7 and 10 ms. A typical measurement is shown in Fig. 4.16. We expect the measurement to understate the time constant, because the measurement indicates the average temperature of the heater, not the temperature of the resonator itself. It is to be noted that the thermal capacitance of the DETF is approximately equal to that of an in-built heater, and so, there is potential in further reducing the thermal time constant in future designs by reducing the thermal mass of the resonator itself.

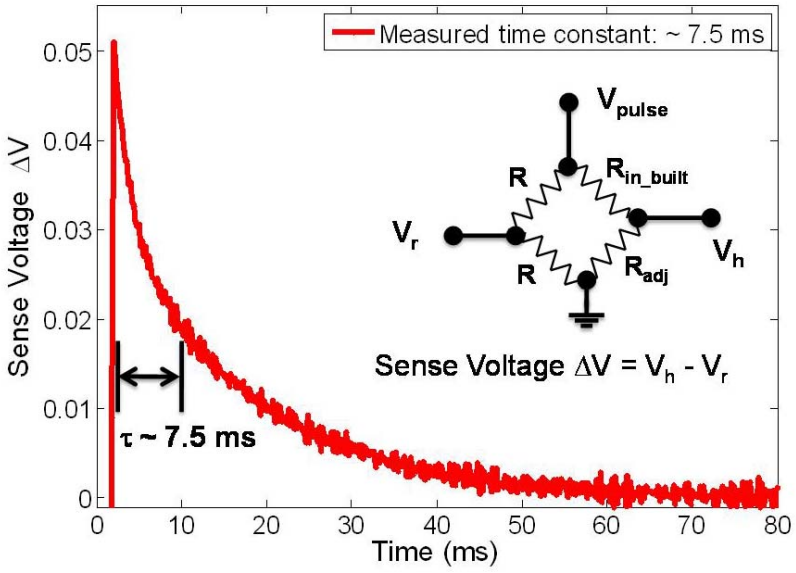

Fig. 4.16: Dynamic thermal response of the micro-ovenized resonator. (Inset) The in-built heater formed one leg of a wheatstone bridge. The measured voltage output from the bridge represents the change in heater resistance as the heater cools down following a heating pulse.

4.4.3 Impact Resistance of Mechanical Suspension

The thermal resistance of the resistive heater directly depends on the length of the beam and is inversely proportional to its cross-sectional area. Design of a large thermal resistance is limited by the reduction of mechanical stiffness of the structure. However, miniaturization allows a stiffer design of the heater having relatively higher thermal resistance. To investigate the stiffness of the thermally isolated DETF structure, a drop test was carried out. The chip was soldered to an oscillator circuit board, which was rigidly bolted to a heating chuck (Fig. 4.17) maintained at a constant temperature of 70 °C.

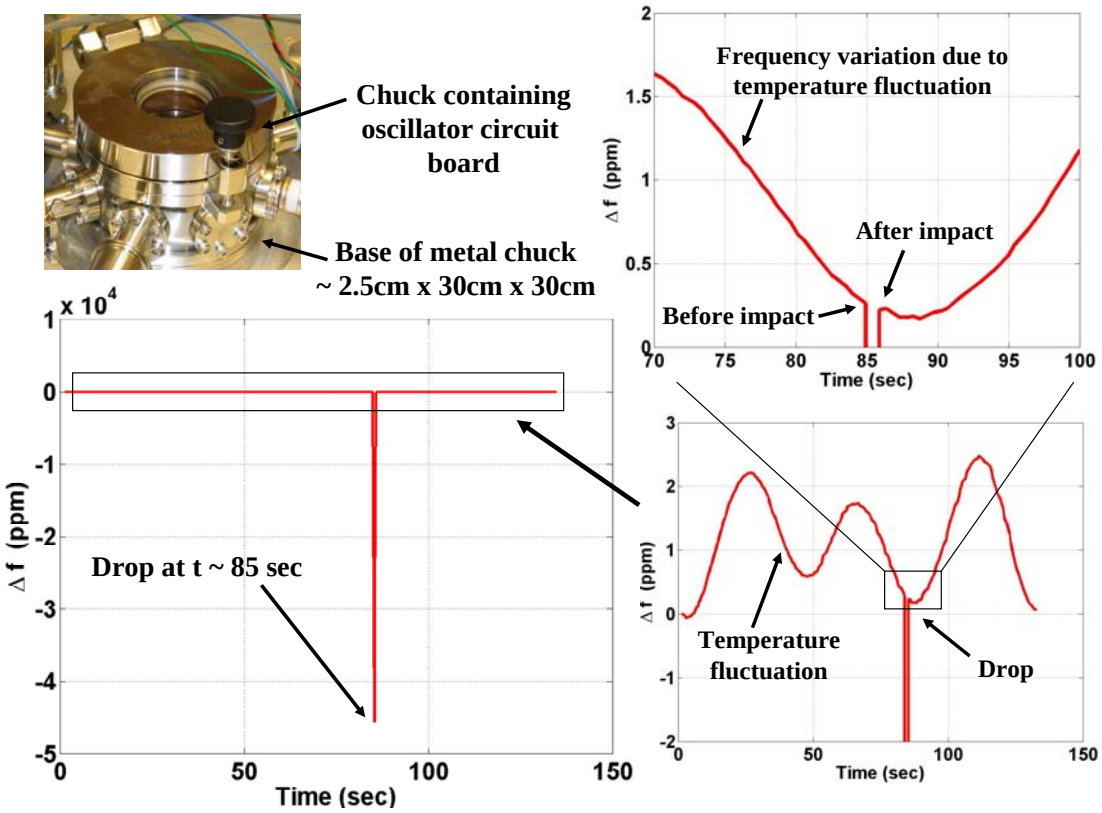

Fig. 4.17: Drop test resulted in a temporary change in frequency at the time of drop.

The chuck was dropped from a height of 1.0 cm onto a rigid platform, and the response of the resonator frequency was measured, as shown in Fig. 4.17. At the time of the impact, the oscillator frequency changed by approximately −45 000 ppm. The resonator immediately returned to normal operation. The change in frequency before and after the impact is within the noise of the frequency fluctuation of the uncompensated resonator due to small variation in the chuck temperature, as shown in Fig. 4.17. Furthermore, the resonators survived the 5000-rpm rotation (up to ~1400 g of acceleration) during the photoresist spin-coating steps of the fabrication process. The spin duration was approximately 1 min and was repeated six to eight times during the fabrication.

4.5 Conclusions and Next Steps

An efficient heat delivery and thermal-isolation mechanism for a MEMS resonator has been demonstrated, with 20x reduction in power consumption and 50x reduction in thermal time constant compared to that of the standard un-isolated DETF resonator. The in-built heater-based thermal-isolation technique serves a dual purpose of localized heating and local thermal isolation, thereby providing maximum heating with minimized input power.

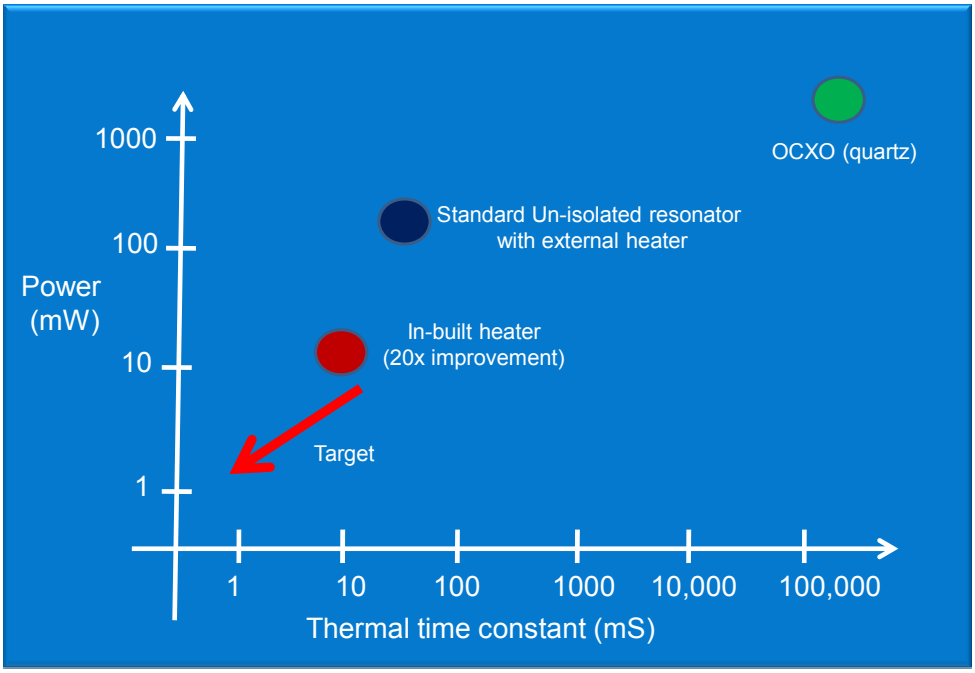

Fig. 4.18: Comparative regime map showing the power consumption and thermal time constant of in-built heater resonator, standard resonator and quartz OCXO.

At the same time, the device has high impact resistance because of its miniature design. Compared to the commercially used quartz crystals (1–10 W and around 30 min warm-up time), this technique has demonstrated orders of- magnitude improvement in power dissipation and dynamic thermal response with a potential for further improvement. A comparative regime map is shown in Fig. 4.18. Furthermore, this method is simple enough to implement it into any existing MEMS fabrication process. The described design of micro-oven is highly suitable for temperature stabilization of micromechanical resonators and for very precise control of frequency (< 1.0 ppm) over a temperature span of 125°C.

It is possible to further reduce the power consumption by increasing the thermal resistance of the in-built heater. The thermal resistance of a single-crystal silicon heater, with known thermal conductivity, is dependent on the length and the cross-section of the heater geometry as given below

$$R_{th} \propto \frac{l}{A_c} \tag{4.15}$$

The thermal resistance of the heater can be increased either by increasing its length or by decreasing its cross-section area. The cross-section area is limited by the fabrication constraints and hence difficult to reduce beyond a certain point. The only parameter to play with, is the length of the heater.

However, it is difficult to increase the length of the heater structure arbitrarily as it is related to the stiffness of the structure as given below

$$K \propto \frac{1}{l} \tag{4.16}$$

The stiffness of the structure should be large enough to keep the device mechanically robust and reliable.

From equations (4.15) and (4.16), it can be interpreted that it is difficult to increase the thermal resistance of the heater without first studying the mechanical stiffness of the device and its effect on the performance of the device. In other words, the DETF resonator needs to be not only thermally isolated but also mechanically isolated.

Chapter 5

Mechanical Isolation of MEMS Resonator

This chapter presents an investigative study of mechanical robustness or isolation of the electrostatically coupled encapsulated silicon DETF micromechanical resonator. This study of mechanical isolation of the resonator is necessary to understand the limit of the thermal isolation. The external vibration and acceleration from the environment affects the performance of the resonator. The chapter describes the acceleration sensitivity and the resulting vibration-induced phase noise of a standard as well as thermally isolated resonator. The thermally isolated resonator described in the previous chapter is renamed as a spring mounted resonator in this chapter for better clarity. External vibrations can produce phase noise in micromechanical resonators by generating time-varying stress in the resonant beams. However, the spring mounted design can reduce this induced axial stress. Measurements and simulations show that the acceleration sensitivity and the vibration-induced phase noise of this device can be reduced 1000x smaller than that of the previously published silicon micromechanical resonator and 10x smaller than the commercially used high end SC (stress compensated)-cut quartz resonator. The chapter also describes the analysis of vibration isolation. The vibration isolation discussed at the end of the chapter is different from the acceleration dependent vibration-induced phase noise. The vibration isolation primarily focuses on the magnification of the effect of the external vibration due to the lateral resonance of the entire DETF resonator structure.

5.1 Introduction

The frequency of a silicon resonator is dependent on many parameters including external environmental accelerations and vibrations. Many applications require the resonator to operate stably in the face of ambient vibrations (e.g. frequency reference in a car or helicopter). The acceleration effects in frequency sources assumed importance at least since the advent of missile and satellite applications [87] – [92], Doppler radars [93], [94], and other systems requiring extremely low noise [95], [96]. Time-dependent acceleration, i.e., vibration, can cause a large increase in the noise level of an oscillator. In fact, in frequency sources operating on mobile platforms, the vibration-induced phase noise is usually greater than all other noise sources combined [87]. It is therefore desirable for the resonator to have minimum sensitivity to these disturbances.

The chapter is segmented into two major sections. The first section describes the causes and effects of acceleration sensitivity and the resulting vibration-induced phase noise of the silicon resonator. There are two effects discussed here on the performance of the resonator due to the external acceleration and vibrations. First is the induced stress on the resonator beams and the second is the change in the electrostatic capacitance between the resonator beams and the electrodes due to the change in the gap by the external vibration. Both phenomenon can lead to phase noise in the output frequency of the resonator and hence are important for the analysis. The second section explains the concept of vibration isolation by studying the lateral resonance of the structure.

5.2 Acceleration Sensitivity

5.2.1 Acceleration Effects and Vibration Induced Phase Noise

The "acceleration sensitivity" of a resonator is an important figure of merit and has been widely studied for quartz crystal resonators [87], [97], [98]. A resonator under a steady external acceleration has a slightly different resonant frequency than the same resonator experiencing zero acceleration. The magnitude of the acceleration-induced frequency shift is proportional to the magnitude of the acceleration, the direction of the acceleration and also on the acceleration sensitivity of the resonator [87], [97], [99] (Fig. 5.1).

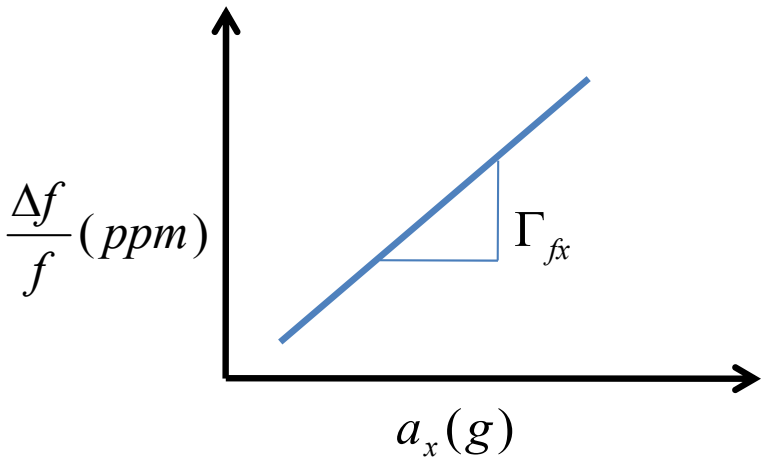

Fig. 5.1: A typical plot showing the effect of acceleration in x-direction on the change in resonator frequency. The slope of the curve is acceleration sensitivity in x-direction (Γ_x)

Therefore, the frequency during acceleration can be written as

$$f_a = f_0(1 + \boldsymbol{\Gamma}.\boldsymbol{a}) = f_0\left(1 + \Gamma_x a_x + \Gamma_y a_y + \Gamma_z a_z\right) \tag{5.1}$$

where f_a is frequency of the resonator experiencing acceleration $\boldsymbol{a}$, f_0 is the frequency with no acceleration (often referred to as the "carrier frequency"), and $\boldsymbol{\Gamma}$ is the acceleration sensitivity. The normalized frequency shift due to acceleration is given by equation (5.2).

$$\frac{\Delta f}{f_0} = \boldsymbol{\Gamma}.\boldsymbol{a} = \left(\Gamma_x a_x + \Gamma_y a_y + \Gamma_z a_z\right) \tag{5.2}$$

Time-dependent acceleration (Fig. 5.2 and Fig. 5.3), i.e. vibration, can cause vibration induced phase noise. The time dependent frequency variation of the resonator due to a sinusoidal external vibration at f_v can be determined by

$$f_a = f_0(1 + \boldsymbol{\Gamma}.\boldsymbol{a}(\boldsymbol{t})) = f_0(1 + (\boldsymbol{\Gamma}.\boldsymbol{a_0})cos(2\pi f_v t)) \tag{5.3}$$

where $\boldsymbol{a_0}$ is the peak acceleration in g, f_v is the frequency in Hz, and t is time in seconds. Using (5.2), this can be rewritten as shown in equation (5.4)

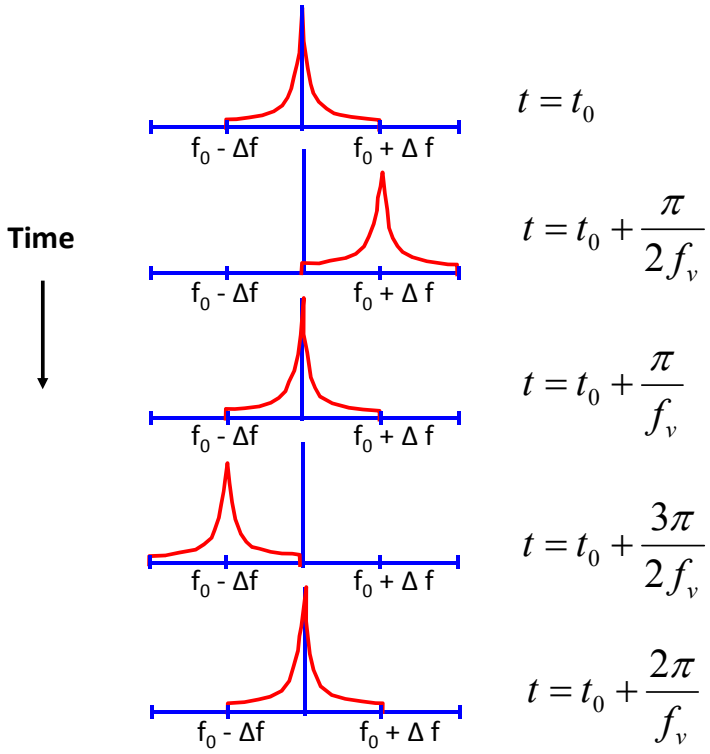

Fig. 5.2: Instantaneous carrier frequency for several instants during one cycle of vibration.

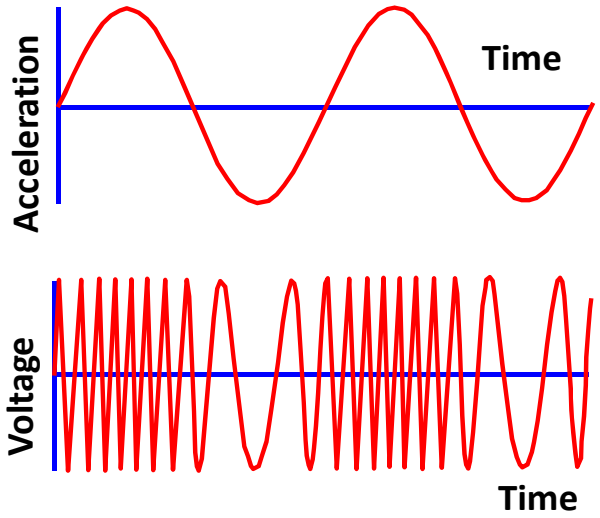

Fig. 5.3: Time dependent acceleration (top) and resulting oscillator output showing frequency modulation (bottom).

$$f_a = f_0 + \Delta f cos(2\pi f_v t) \tag{5.4}$$

where Δf, given from the equation (5.2), is the peak frequency shift due to the acceleration $\boldsymbol{a_0}$.

The output voltage of the micromechanical resonator based oscillator is given as

$$V(t) = V_0 cos\big(\phi(t)\big) \tag{5.5}$$

where the phase $\phi(t)$ is given as the time integral of the frequency.

Using (5.4), it can be written as

$$\phi(t) = 2\pi \int f(t)dt = 2\pi f_0 t + \frac{\Delta f}{f_v}\sin(2\pi f_v t) \tag{5.6}$$

Using equation (5.6) in (5.5), the output voltage due to time-dependent acceleration induced frequency shift (Fig. 5.3) is given as

$$V(t) = V_0 cos\left(2\pi f_0 t + \frac{\Delta f}{f_v}\sin(2\pi f_v t)\right) \tag{5.7}$$

The above expression is a frequency-modulated signal containing phase noise. It can be expanded in an infinite series of Bessel function [87], [97], [98] resulting in

$$V(t) = V_0[J_0(\beta)\cos(2\pi f_0 t) + J_1(\beta)\cos(2\pi(f_0 + f_v)\,t) + J_1(\beta)\cos(2\pi(f_0 - f_v)\,t) + J_2(\beta)\cos(2\pi(f_0 + 2f_v)\,t) + J_2(\beta)\cos(2\pi(f_0 - 2f_v)\,t) + \ldots] \quad (5.8)$$

$$where \quad \beta = \frac{\Delta f}{f_v} = \frac{\boldsymbol{\Gamma}.\boldsymbol{a_0} f_0}{f_v}$$

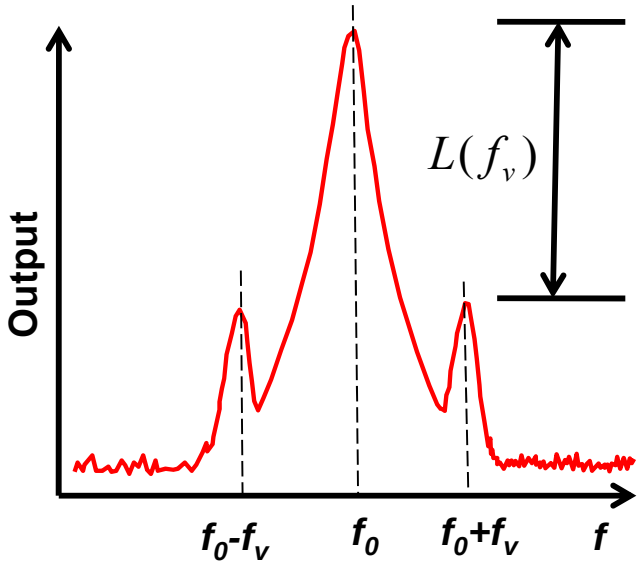

Fig. 5.4: Vibration induced sidebands and carrier resulting from sinusoidal acceleration at frequency f_v.

The parameter β in equation (5.8) is known as the modulation index [87], [97]. The first term in equation (5.8) represents the original signal at carrier frequency. The other terms are vibration-induced sidebands at frequencies $f_0 + f_v$, $f_0 - f_v$, $f_0 + 2f_v$, $f_0 - 2f_v$, etc. Most of the power is in the carrier, a small amount is in the first spectral line pair, and the higher order spectral lines are negligible. For a small modulation index, $\beta < 0.1$, the relative strength of vibration induced phase noise with respect to the carrier f_0 in the first spectral line pair is shown in Fig. 5.4 and is given by [87], [97], [99], [100]

$$\mathcal{L}(f_0 \pm f_v) = 20log\left(\frac{f_0\,\boldsymbol{\Gamma}.\boldsymbol{a_0}}{2f_v}\right) \quad [dBc] \tag{5.9}$$

5.2.2 Model for Axial Stress in the Resonator Beams

The principal mechanism that causes the acceleration sensitivity is the axial stress experienced by the resonator beams. This section describes an analysis of the axial stress in the beams of the resonator. The axial stress in the spring mounted double ended tuning fork (DETF) type resonator is compared with that of our previously published basic single anchored DETF resonator as shown in Fig. 5.5.

There are two modes of vibration associated with the resonator discussed in this chapter. One is the tuning fork vibration mode which is stimulated by the input electrode and another one is the lateral mode vibration which is stimulated by the external vibration.

The "tuning fork vibrational mode" for the single-anchored and spring supported resonators is near 1.3 MHz. The spring-supported resonator has a lateral mode consisting of the entire resonator vibrating relative to the spring supports at 45 KHz. The single-anchored resonator has a similar mode consisting of the free mass vibrating relative to the anchor at 145 KHz, where the beams are acting as the spring for this mode.

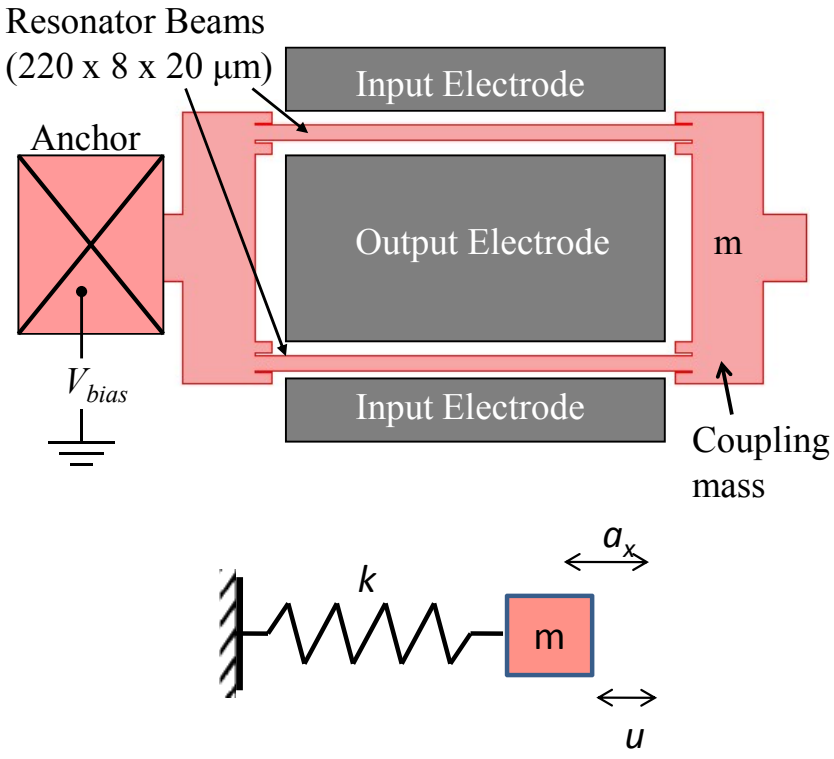

(a)

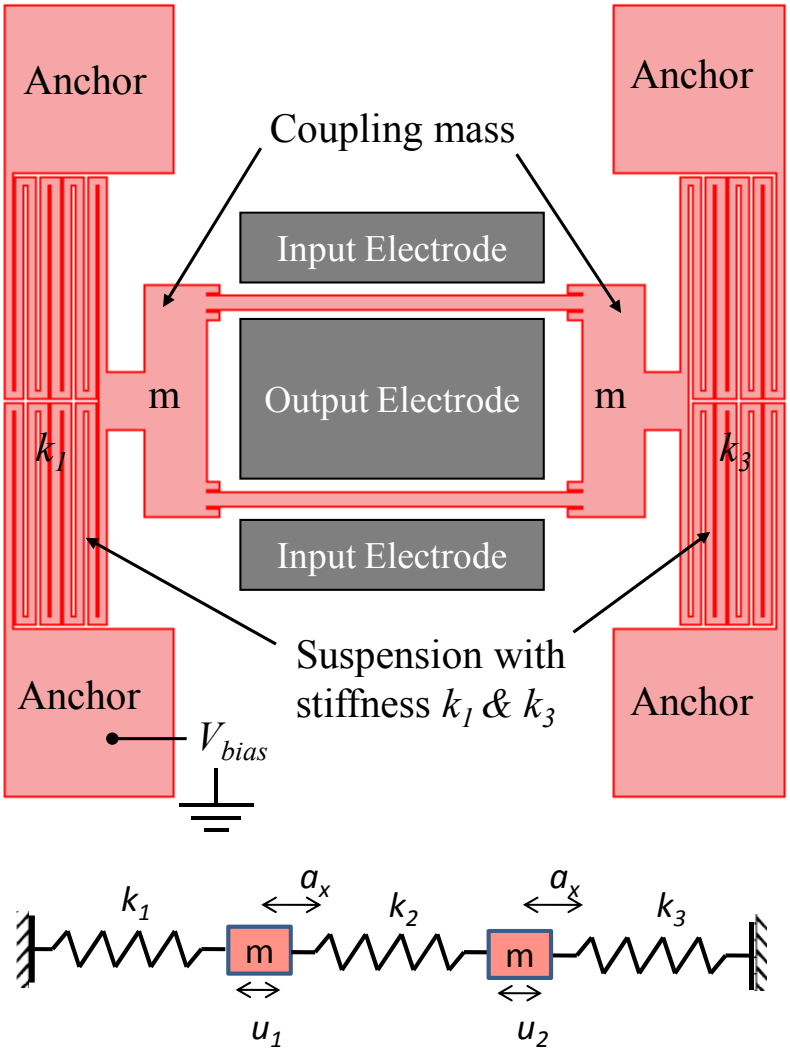

(b)

Fig. 5.5: (a) The schematic of the basic single anchored DETF resonator. The effect of the external acceleration a_x is modeled by a spring mass system, where m is the coupling mass, k is the stiffness of the resonator beam and u is the displacement due to inertia force generated by the external acceleration a_x. (b) The schematic of a spring supported DETF resonator showing serpentine type resistive silicon suspension on both sides of the resonator with stiffness k_1 and k_3. The stiffness of the resonator beam, in this case, is represented by k_2.

The external vibration or the acceleration causes an axial force on the resonator beam. The dependence of resonator frequency on axial load P is given by [85]

$$f = \frac{\lambda^2}{2\pi l^2}\left(1 + \frac{Pl^2}{EI\pi^2}\right)^{\frac{1}{2}}\left(\frac{EI}{m}\right)^{\frac{1}{2}}, \qquad \lambda = 4.73 \tag{5.10}$$

where λ is a dimensionless parameter which is a function of the boundary conditions applied to the beam and is equal to 4.73 for a free-free or clamped-clamped beam, l is the length of the beam, E is the modulus of elasticity, I is the area moment of inertia of the beam about neutral axis, and m is the mass per unit length of the beam.

The axial load P experienced by the resonator beam can be estimated with the help of a static analysis using a lumped spring mass model as shown in Fig. 5.5. The axial load due to external acceleration a_x for the basic DETF structure is given by

$$P_{standard} = ku = ma_x \tag{5.11}$$

where m is the lumped mass (coupling mass + half the mass of the beams) and k is the stiffness of the resonator beam. The mass of the beam is included in the calculation of the lumped mass to account for the effect of the distributed mass of the beam on the axial load. From the equations (5.10) and (5.11), the change in frequency Δf is estimated to be approximately 0.01 Hz for 1g of acceleration resulting in the acceleration sensitivity Γ_x of approximately 6.5 ppb/g from the equation (5.2).

For the spring supported DETF structure, the axial load experienced by the resonator beam is given by

$$P_{spring-supported} = k_2(u_2 - u_1) = ma_x\left(\frac{k_3 - k_1}{k_1 + \frac{k_1 k_3}{k_2} + k_3}\right) \tag{5.12}$$

where k_2 is the stiffness of the resonator beam and $k_1\ and\ k_3$ are the stiffnesses of the mechanical suspension on both sides of the resonator. As can be seen from (5.12), if k_3 is equal to k_1, i.e., the left and right support are equally stiff, then the axial load experienced by the resonator beam tends to zero. It should be mentioned that this lumped model is effective only when $k_2 \gg k_3, k_1$ and it can be assumed that the inertia effect of the distributed mass of the resonator beam are negligible. In case of $k_2 \ll k_3, k_1$, the mass of the resonator beam needs to be accounted for and should not be neglected. For this design $k_2 \approx 10{,}000k_1$. Since the design of the spring mounted DETF resonator is symmetric (Fig. 5.5(b)), it can be assumed that $k_1 \approx k_3$, resulting in an acceleration insensitive resonator. However, if we account for the variations in the process parameters of our fabrication process, the difference in $k_1 and\ k_3$ can be as high as 5% resulting in the acceleration sensitivity of upto 0.1ppb/g. For a simplified theoretical analysis here, we will stick to the assumption of a symmetric design and ignore the error due to fabrication.

The above analysis is based on a simple lumped model and does not capture the effect of the distributed mass of the resonator beams. To investigate this, a finite element

simulation is performed for both basic and spring mounted structure assuming the design of the spring supported resonator to be symmetric. We first perform a plane stress static analysis with a body load (force per unit volume) corresponding to the applied external acceleration to find out the resultant stress in the resonator beams (Fig. 5.6).

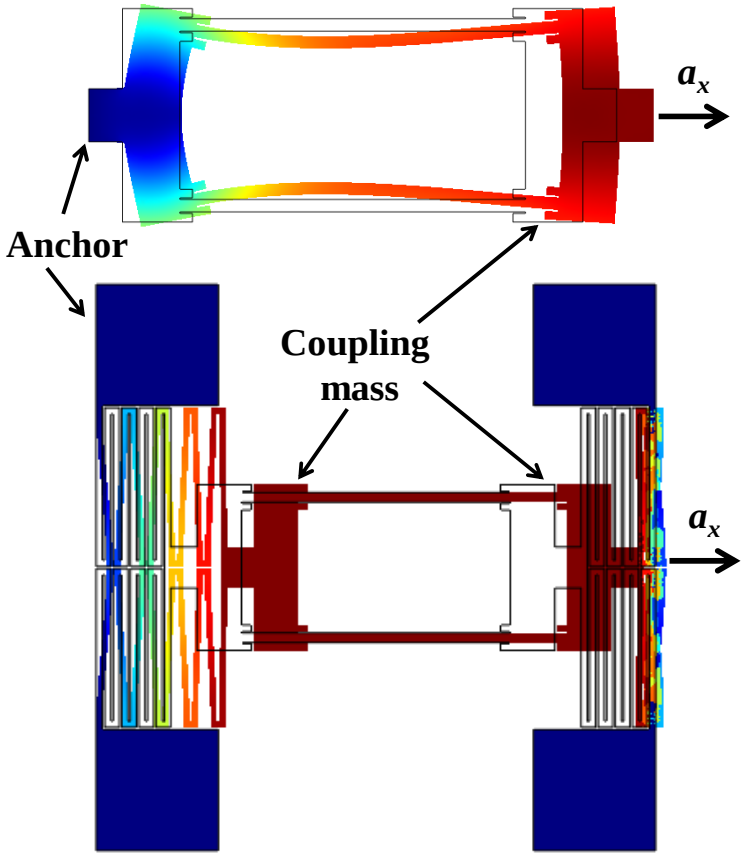

Fig. 5.6: Finite element simulation of the standard resonator (top) and the spring mounted resonator (bottom) for acceleration in the x direction a_x. The result shows the deformation of the resonator due to the body load generated by the acceleration. The deformation shown above is exaggerated.

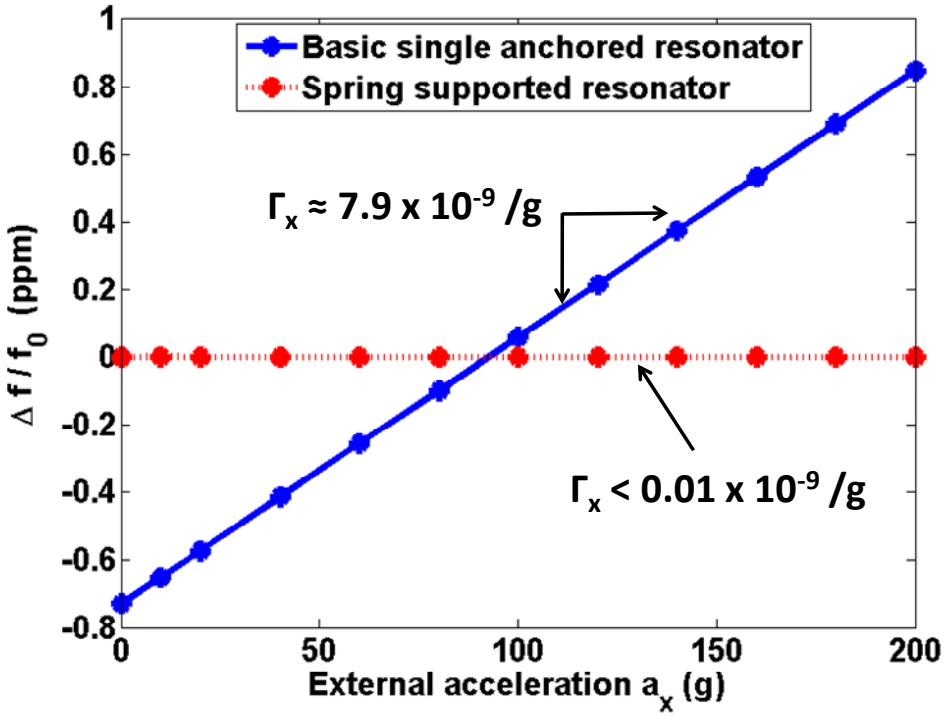

Fig. 5.7: Finite element simulation showing the change in frequency with respect to the acceleration for basic resonator as well as for spring supported resonator.

Then, we carry out an eigenfrequency analysis of the same resonant structure under the pre-stressed condition. The resulting eigenfrequency corresponds to the frequency of the resonator beam under axial stress. Fig. 5.7 shows the plot of change in frequency with respect to the magnitude of the external acceleration. The slope of the curve, which is the acceleration sensitivity Γ_x, is approximately 7.9 ppb/g for the basic DETF resonator. However, for the spring mounted DETF resonator the acceleration sensitivity is found to be less than 0.01 ppb/g, which is in compliance with the analytical result for the symmetric spring supported design. Further analysis and FEM simulations confirm that there is no first order sensitivity to acceleration in the *y* and *z* directions.

5.2.3 Experimental Results

For the experimental measurement, a dynamic vibration method was used. One device each from the spring mounted DETF resonator and the basic DETF resonator were tested for collecting experimental data. The device attached on the PCB was mounted on a shaker (Fig. 5.8) and subjected to a sinusoidal vibration in x direction at frequencies 80 Hz, 150 Hz, and 220 Hz with accelerations ranging from 0 to 30g.

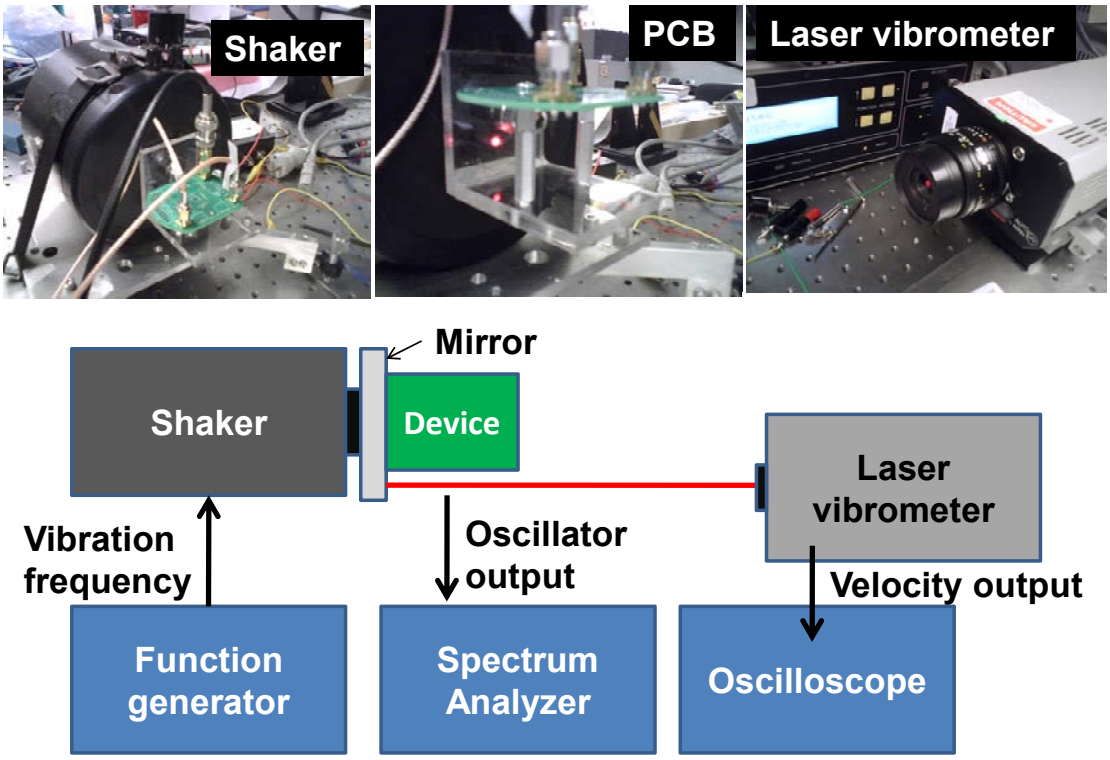

Fig. 5.8: Schematic of dynamic vibration experimental setup. The resonator device attached in a package is soldered into the PCB which in turn is mounted on the shaker. The shaker is actuated using a frequency generator and the amplitude of the shaker vibration is measured by laser vibrometer. The oscillator output is measured using a spectrum analyzer.

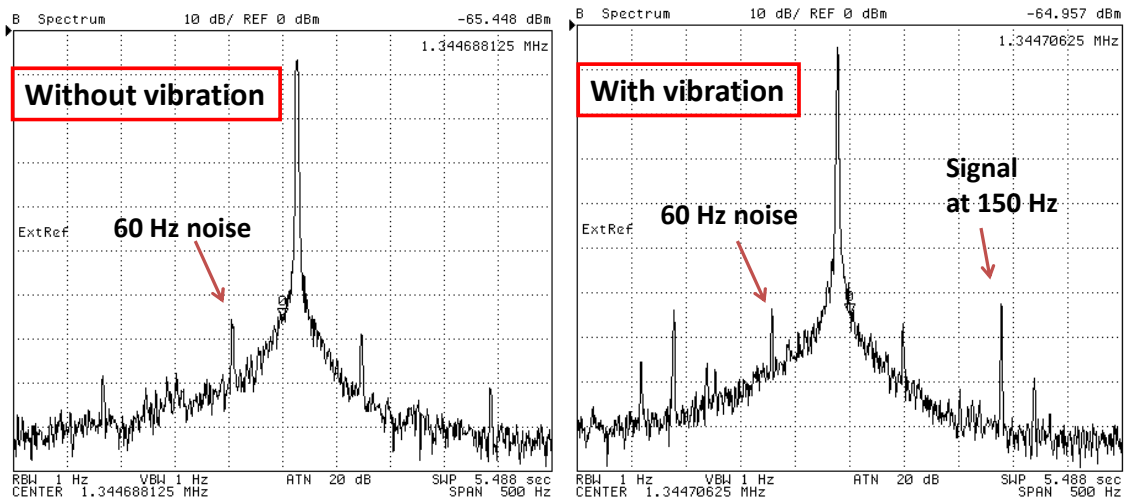

Fig. 5.9: Experimental result showing the effect of vibration on a basic single anchored DETF resonator. The sinusoidal vibration was applied in x-direction at 150 Hz with 30g acceleration. The presence of external vibration causes sidebands at 150 Hz in the above spectrum.

A typical measurement result for 30 g acceleration at 150 Hz is shown in Figs. 5.9 and 5.10. The amplitude of the acceleration is measured by using a laser vibrometer. The presence of sinusoidal vibration at 150 Hz causes sidebands in the basic single anchored DETF resonator (Fig. 5.9) at an offset of 150 Hz from the carrier frequency f_0. However, the sidebands in the spring mounted DETF resonator for the same frequencies and the acceleration range are buried into the noise (Fig. 5.10). The relative strength of vibration induced phase noise (sidebands) with respect to the carrier frequency f_0 , $\mathcal{L}(f_0 \pm f_v)$, for the basic DETF resonator is measured to be -57dBc which is close to the estimated value of -54 dBc; and for the spring mounted DETF resonator the measured value is less than -85 dBc whereas the theoretically estimated value is approximately -110 dBc.

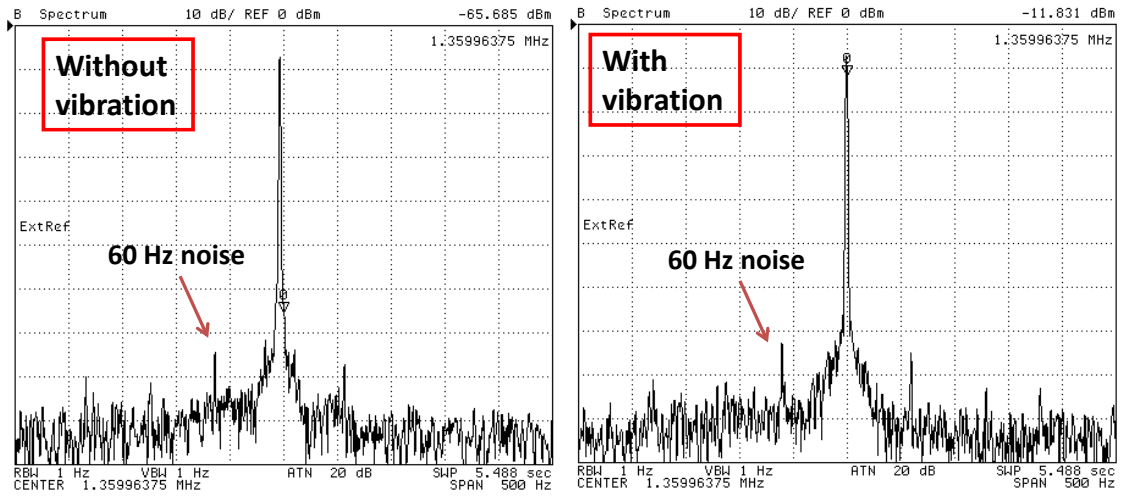

Fig. 5.10: Experimental result showing the effect of vibration on a spring supported DETF resonator. The sinusoidal vibration was applied in x-direction at 150 Hz with 30g acceleration. The presence of external vibration causes no visible sidebands in the above spectrum. In other words, the sidebands are buried in the noise.

It should be mentioned that the actual acceleration sensed by the resonator structure might be slightly different from the measured acceleration due to the damping and vibration associated with the natural frequency of the fixture on which the PCB was mounted. However, the related errors are assumed to be small as the measured result correlates well with the analytical and simulated result. Measurements were also done in y and z directions for upto 30g and no sidebands were observed [99]. As predicted by the analytical model and the finite element simulations, and also supported by the previous publication [100], we conclude that there is only a weak sensitivity to acceleration in the y and z directions [99].

5.2.4. Deformation Acceleration Sensitivity

Deformation acceleration sensitivity Γ_u, (Fig. 5.11) is defined as

$$\Delta u = \Gamma_u . a = \Gamma_{ux} a_x + \Gamma_{uy} a_y + \Gamma_{uz} a_z \quad (5.13)$$

where a is the acceleration vector. The deformation acceleration sensitivity assumes importance in our process because of the capacitive transduction between the resonator beams and the electrodes.

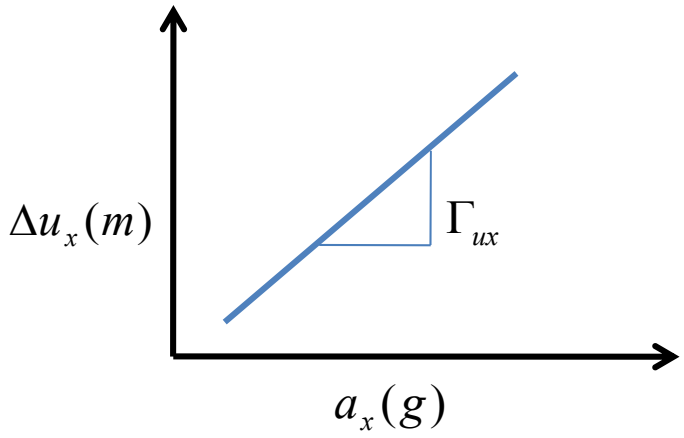

Fig. 5.11: A typical plot showing the effect of acceleration in a particular direction on the deformation of the resonator beam. The slope of the curve is acceleration sensitivity in that particular direction.

Any substantial deformation of the resonator structure due to external acceleration leads to change in capacitive force which in turn can lead to either snapping of the resonator beams to the electrodes or change in resonator frequency. In this section we will analyze both effects.

A voltage controlled parallel-plate electrostatic capacitor exhibits an important behavior called pull-in. In order to explain it, we consider the stability of the equilibrium that must exist between the electrostatic force pulling the plates toward each other and the spring force of the parallel plate acting as a restoring force. Stability analysis involves perturbing the position slightly and asking whether or not the net force tends to return to the equilibrium position.

The capacitive force at voltage V and gap g, using a sign convention that assigns a positive sign for forces that increases the gap, is [101]

$$F_{net} = \frac{-\varepsilon A V^2}{2g^2} + k(g_o - g) \tag{5.14}$$

where g_o is the gap at zero volts and zero spring extension, ε is the permittivity of the material between the gap (vacuum in this case), k is the spring constant of the parallel plate. At a point of equilibrium, F_{net} is zero. If we now ask how F_{net} varies with a small perturbation of the gap to $g + \delta g$, we can write

$$\delta F_{net} = \left.\frac{\partial F_{net}}{\partial g}\right|_V \delta g \tag{5.15}$$

If δF_{net} is positive for positive δg, then g is an unstable equilibrium point, because a small increase δg creates a force tending to increase it further. If δF_{net} is negative, then g is a stable equilibrium point.

We can evaluate δF_{net} using

$$\delta F_{net} = \left(\frac{\varepsilon A V^2}{g^3} - k\right) \delta g \tag{5.16}$$

In order for g to be stable equilibrium, the expression in parenthesis must be negative, which means that

$$k > \frac{\varepsilon A V^2}{g^3} \tag{5.17}$$

Clearly, at equilibrium (pull-in voltage) there are two equations that must be satisfied: the original requirement that $F_{net} = 0$, and the new requirement that

$$k = \frac{\varepsilon A V^2}{g^3} \tag{5.18}$$

From equations (5.14) and (5.18), it can be shown that the pull-in occurs at

$$g_{PI} = \frac{2}{3} g_o \tag{5.19}$$

This means, if the deflection of the resonator beam is more than one-third of the original gap (g_o), then the beam will snap to the electrode, leading to the failure of the device. The above analysis of pull-in gap will be the basis for the design of the resonator structure for the deformation acceleration sensitivity (Γ_u). For example, for a gap size of 1.5μm between the resonator beam and the electrodes, any force due to external acceleration causing beam deformation more than 0.5μm will lead to the failure of the device because of the pull-in.

We estimated the deformation acceleration sensitivity by using a finite element simulation, where we applied a body load on the resonator DETF structure and measured the maximum deflection corresponding to all x, y and z direction, similar to the one shown in Fig. 5.6. The resulting sensitivity for the basic DETF resonator in y and z direction is found to be

$$\Gamma_{uy} \approx 1.3 \text{ x } 10^{-11} \frac{m}{g}$$

$$\Gamma_{uz} \approx 1.5 \text{ x } 10^{-11} \frac{m}{g} \tag{5.20}$$

For the spring mounted resonator, the dominant component of the sensitivity is in x-direction and is found to be

$$\Gamma_{ux} \approx 1.5 \text{ x } 10^{-10} \frac{m}{g} \tag{5.21}$$

The other components of the sensitivities for both the basic and the spring mounted resonators are negligible and hence not mentioned above. As can be seen from equations (5.20) and (5.21), the most dominant component of the sensitivity for the spring mounted resonator is ten times worse than that of the basic resonator. This means that the spring mounted resonator is more susceptible to mechanical damage due to external acceleration.

It would be interesting to know the change in frequency of the resonator due to the external vibration of the resonator structure which causes variation of the capacitive gap between the beam and the electrodes. It is assumed here that the vibration amplitude is less than pull-in gap. The primary reason for the change of frequency due to gap change is the electrostatic softening of the beam [59]. The resonator frequency as a function of the gap is given by equation (5.22).

$$\omega = \sqrt{\frac{k - \frac{\eta_1^2}{C_{in}} - \frac{\eta_2^2}{C_{out}}}{m}} \tag{5.22}$$

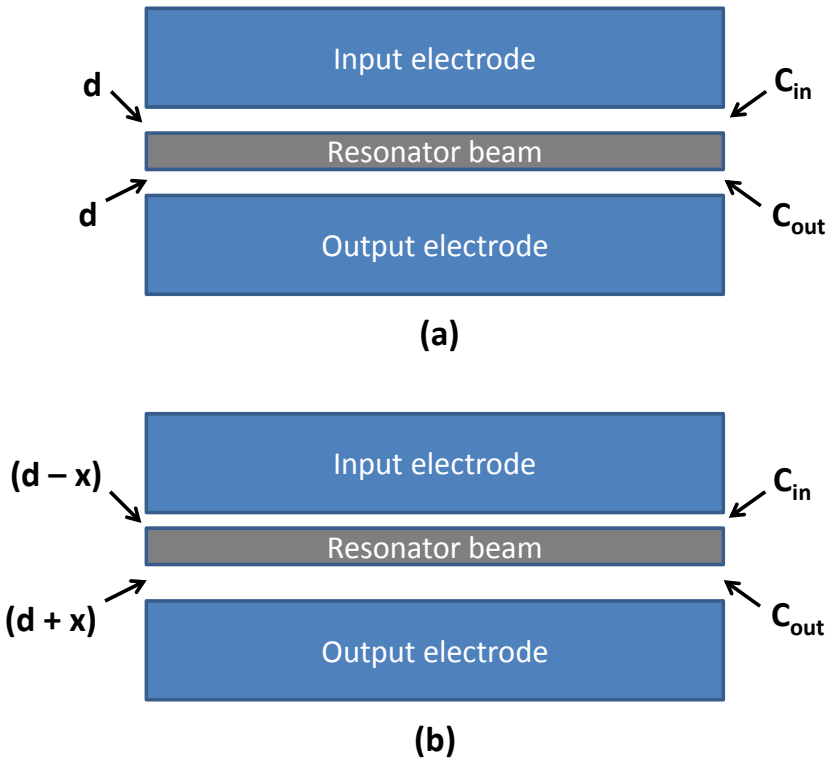

Fig. 5.12: (a) Schematic showing a symmetric gap of d between the resonator beam and the electrodes. (b) The resonator beam is shifted towards one electrode by x due to external force. For simplicity, it is assumed that the beam shift is uniform across its length.

where, $\eta_1 = \frac{C_{in} V_{bias}}{d}$ $\eta_2 = \frac{C_{out} V_{bias}}{d}$

The parameters C_{in} and C_{out} are the capacitance between the beam and the input and the output electrodes respectively (Fig. 5.12). V_{bias} is the bias voltage applied to the resonator and the gap is represented by d. We consider two cases as shown in Fig. 5.12 – (a) symmetric gap between the resonator beam and the electrodes, (b) non-symmetric

gap due to a shift in the resonator beams. We estimated the resonator frequency for both the cases using equation (5.22) and found that for 1g acceleration, that is 1.5 x 10^{-10} m deformation in the spring supported resonator, the change in frequency is approximately 1 x 10^{-13}. This is several orders of magnitude lower than the affect due to axial stress, which correlates well with the experimental result described in the previous section where the change in frequency in the y – direction is buried in the noise and hence not visible. Hence we conclude that the deformation due to external acceleration does not lead to any significant change in frequency of the resonator. However, large deformation due to sudden impact may lead to the failure of the device due to pull-in effect.

5.3 Vibration Isolation

The spring mounted resonator design reduces the effect of the external vibration on the resonator frequency. However, it increases the compliance of the resonator structure resulting in larger deformation for the same external force as compared to that of the basic resonator. The theoretical analysis described in the previous section does not take into account the amplification of the resonator deformation due to the lateral resonance of the structure. There are two resonance modes associated with the resonator. One is the tuning-fork mode which is the vibration of the resonator beam due to input stimulus resulting into the output signal called resonator "carrier" frequency, which is approximately 1.3 MHz for spring mounted resonator. The other one is the lateral-mode which is the vibration of the entire resonant structure including the springs, which is

approximately 45 KHz. In this section, we will discuss about the lateral-mode vibration and its effect on the resonator deformation.

To identify the region of vibration isolation, we need to find the magnitude of the force transmitted. A plot of transmissibility versus ratio of forcing frequency to resonant frequency of the resonator structure is shown in Fig. 5.13 [98], [102]. The transmissibility is defined as the ratio of transmitted force to the impressed force.

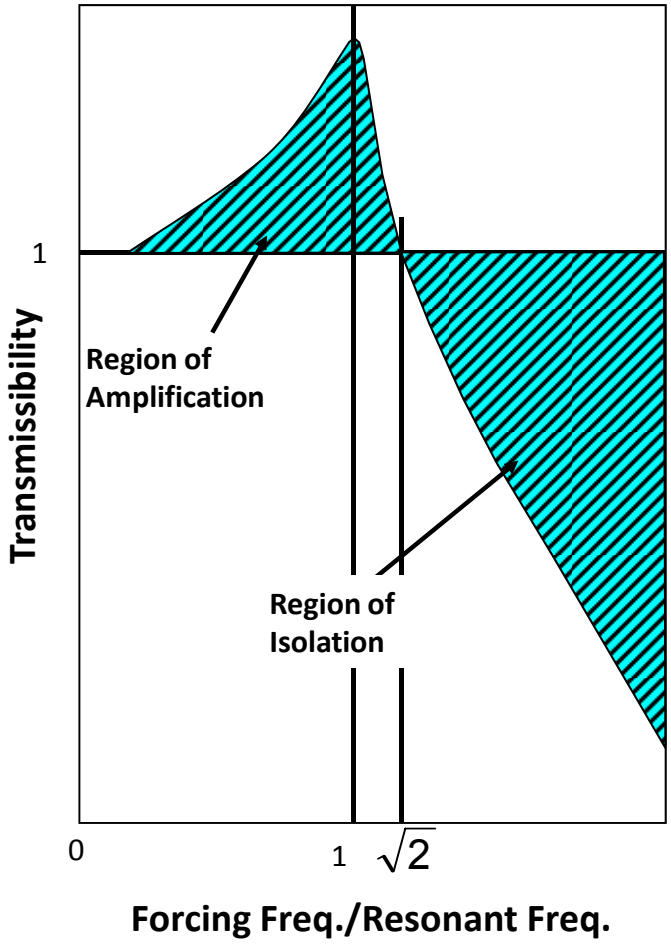

Fig. 5.13: Vibration isolation frequency response (courtesy: John Vig).

As can be seen in Fig. 5.13, there is a region of vibration amplification where the forcing frequency is less than the resonant frequency of the structure. The region of vibration isolation is shown on the right where the forcing frequency is larger than the resonant frequency. However, in reality it is difficult to design a structure falling in the region of vibration isolation, particularly MEMS structure where the resonant frequency of the device tends to increase with the decrease in size. For example, the spring mounted resonator has a lateral mode resonant frequency of 45KHz compared to a sub-KHz frequency range of ambient vibration generally experienced in nature. This means, we need to focus on the left region of the above figure and try to design a device with large resonant frequency to increase vibration isolation. Analytically we can represent the transmissibility in terms of the deformation by evaluating the transfer function of the lateral-mode vibration, which can be represented by Fig. 5.14 and is given by equation (5.23).

$$H(j\omega) = \frac{X(jw)}{F_{ext}(jw)} = \frac{1}{(\mathrm{j}w)^2\mathrm{m} + (\mathrm{j}w)b + k} \tag{5.23}$$

$$where, \quad m\ddot{x} + b\dot{x} + kx = f_{ext}(t)$$

where m is the mass, b is the damping and k is the stiffness of the structure, whereas f_{ext} is the external.

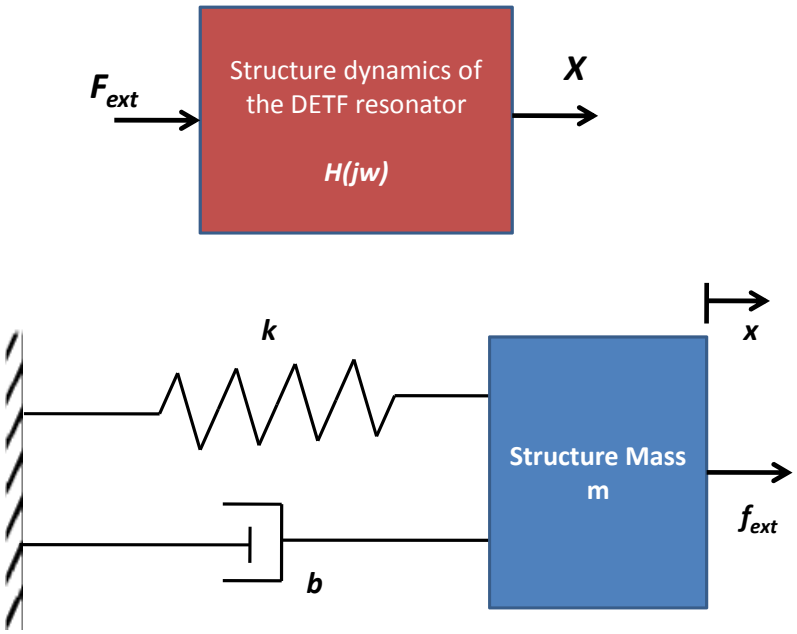

Fig. 5.14: Modeling of the structure dynamics of the DETF resonator (top). Spring mass model of the resonator (bottom).

The quality factor Q and the resonant frequency w_r are given by [59]

$$Q = \frac{\sqrt{km}}{b} \tag{5.24}$$

$$w_r = \sqrt{\frac{k}{m}} \tag{5.25}$$

The transfer function represented by equation (5.23) is shown in Fig. 5.15.

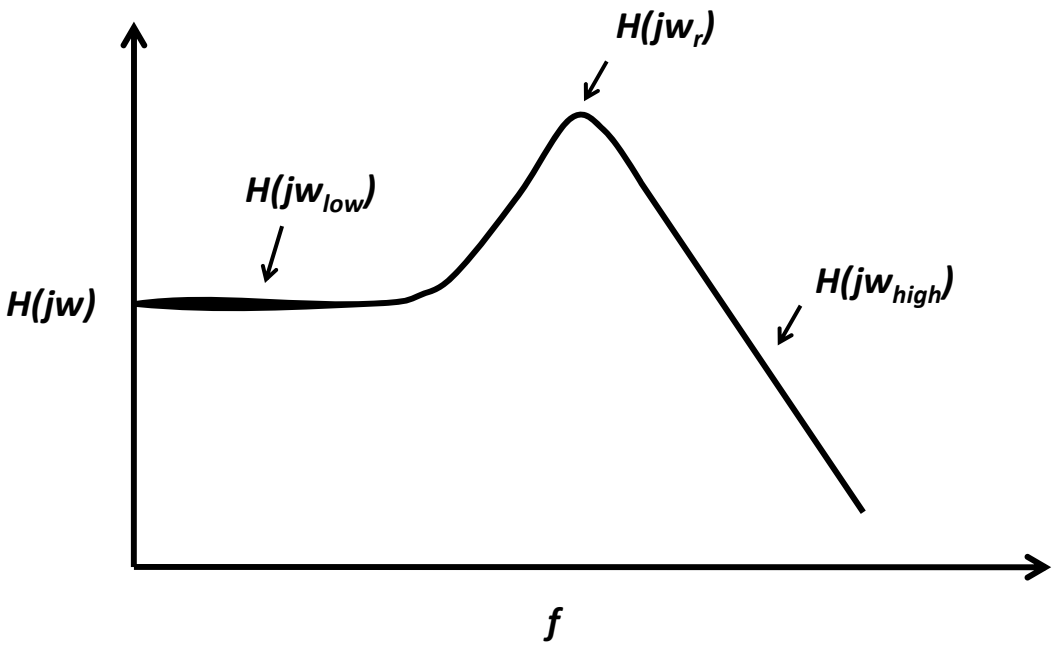

Fig. 5.15: Transfer function of the resonator structure with respect to the frequency. At low frequency it is constant and high frequency it is decreasing with frequency.

At low frequency, equation (5.23) can be rewritten as

$$H(j\omega_{low}) = \frac{X(j\omega_{low})}{F_{ext}(j\omega_{low})} \approx \frac{1}{k} \tag{5.26}$$

From Fig. 5.15 and equation (5.26), we can conclude that the deformation of the resonant structure is constant and inversely proportional to the stiffness of the structure when the ratio of the forcing frequency and the resonant frequency (lateral-mode) is low. In other words, the vibration amplification can be reduced if the resonant frequency of the supporting springs of the spring mounted resonator is large.

5.4 Conclusions

Acceleration sensitivity and vibration-induced phase noise are significant problems in resonator applications. The dominant mechanism of the acceleration sensitivity is axial stress. A DETF resonator with flexible suspension on both sides exhibits reduced acceleration and vibration sensitivity, approximately 1000x smaller than the previously published single anchored DETF micromechanical resonator and 10x smaller than the SC-cut quartz resonator [87], [97], [98]. One possible disadvantage of this spring mounted DETF resonator could be the increased flexibility of the structure resulting in a substantial change in capacitive gap of the electrostatically actuated resonator and possible damage of the device by snapping the resonator beam into the electrode, under impact. Also the increased flexibility of this suspension reduces the lateral mode resonant frequency which is disadvantageous from the vibration isolation point of view. However, this problem can potentially be mitigated by optimizing the design of the resonator structure.

Chapter 6

Design Improvement Using Topology Optimization

This chapter describes the design improvement of the MEMS resonator to provide simultaneous thermal and mechanical isolation. For thermal isolation a design with high thermal resistance is required while for mechanical isolation a design with high stiffness is required. As explained in previous chapters, achieving simultaneous thermal and mechanical isolation is challenging, and difficult to design intuitively. A topology optimization technique is used here to increase the stiffness of the resonator support, and then a micro-serpentine structure is designed on the resulting stiff support of the resonator to increase the thermal resistance of the in-built heater, without reducing its stiffness below the desired value. The combined effect of high stiffness and large thermal resistance leads to a resonator design with simultaneous thermal and mechanical isolation.

Sizing, shape and topology optimization problems address different aspects of the structural design problem. In a typical sizing problem, the goal may be to find the cross-section of a truss structure given the shape and topology of the structure as shown in Fig. 6.1. Similarly, shape optimization may be to find the shape of a hole in a structure given its topology (Fig. 6.1). Topology optimization of solid structures involves the

determination of features such as the number, location and shape of holes and the connectivity of the domain; and hence is more fundamental to size and shape.

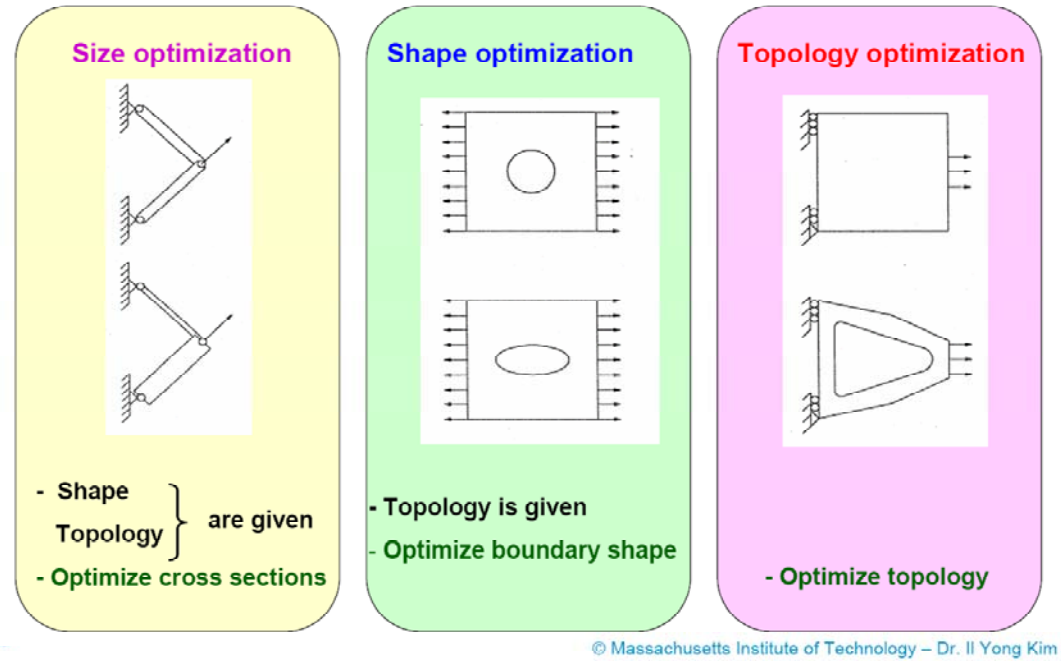

Fig. 6.1: Structural optimization categorized into size, shape and topology optimization. (Courtesy: Dr. I. Y. Kim)

6.1 Topology Optimization

In this section, we will discuss the finite element method (FEM) based stiffness optimization technique. We will first formulate a general stiffness problem in a mathematical form and then describe a solution method using an optimality criteria method. This technique is then used to find the shape of the resonator support for the heater design.

6.1.1 Problem Formulation

The purpose of topology optimization is to find the optimal layout of a structure by distributing the materials in a given region. We will restrict our discussion to the maximum global stiffness formulation, in other words minimum compliance formulation. First a general mathematical representation of the minimum compliance problem will be discussed, and then its discrete form will be presented. We will then represent the discrete form into a "0 – 1" form which is the backbone of the topology optimization technique described here. Finally this "0 – 1" form will be modified into a penalty form to convert the integer variable, 0 and 1, into a continuous variable, making the problem easier to solve.

6.1.1.1 Minimum Compliance Formulation

To design a structure with maximum global stiffness, we need to design for minimum compliance or minimum strain energy. The optimum design problem can be defined as the problem of finding the optimal choice of stiffness tensor $E_{ijkl}(x)$ [103] which is a variable over the chosen domain. Introducing the energy bilinear form (i.e., the internal virtual work of an elastic body at the equilibrium u and for an arbitrary virtual displacement v):

$$a(u,v) = \int E_{ijkl}(x)\ \varepsilon_{ij}(u)\varepsilon_{kl}(v)d\Omega \qquad (6.1)$$

with linearized strains

$$\varepsilon_{ij}(u) = \frac{1}{2}\left(\frac{\partial u_i}{\partial x_j} + \frac{\partial u_j}{\partial x_i}\right) \tag{6.2}$$

and the load linear form in the absence of any traction force is

$$l(u) = \int f u d\Omega \tag{6.3}$$

where f is the body force.

The minimum compliance (maximum global stiffness) problem takes the mathematical form [103] – [105]

$$\begin{aligned} &\min\ l(u), \quad for\ all\ \ u\ \in\ U, E \\ &s.t.:\ a_E(u,v) = l(v), \quad for\ all\ \ v\ \in U \\ &\qquad E\ \in\ E_{ad} \end{aligned} \tag{6.4}$$

Here U denotes the space of kinematically admissible displacement fields, E_{ad} denotes the set of admissible stiffness tensors for our design problem. When solving problems of the form (6.4) computationally, we will discretize the problem domain using finite elements. There are two fields of interest here, namely the displacement u and the stiffness E.

We can write the discrete form of (6.4) as

$$\min \; f^T u \tag{6.5}$$

$$s.t.: \; K(E_e)u \; = \; f,$$

$$E_e \; \in \; E_{ad}$$

Here u and f are the displacement and load vectors, respectively. The global stiffness matrix K depends on the stiffness E_e in element e, numbered as e = 1,….,N.

The stiffness matrix K is given as

$$K = \sum_{e=1}^{N} K_e \, (E_e) \tag{6.6}$$

where K_e is the element stiffness matrix.

6.1.1.2 The "0 – 1" Approach

We are interested in the determination of the optimal placement of a given isotropic material in space, i.e., we need to know which points of space plays an important role in taking the load and should be material points, and which points are not required and should remain void (no material). That is, we need to come up with a geometric representation of a structure with black-white rendering of an image. In discrete form this means a black-white representation of the geometry, with pixels given by the finite

element discretization [103] – [105]. This implies that the set E_{ad} of admissible stiffness tensors consists of those tensors for which [103] – [105]:

$$E_{ijkl}(x) = \rho(x)E^0_{ijkl}\,, \qquad \rho(x) = \begin{cases} 1 \;\; if \; x \in \Omega^{opt} \\ 0 \;\; if \; x \in \Omega \backslash \Omega^{opt} \end{cases} \tag{6.7}$$

$$\int \rho(x)\, d\Omega = Vol(\,\Omega^{opt}) \leq V'$$

Here $\rho(x)$ is called the density function and is the design variable for the minimum compliance problem. The volume inequality in (6.7) puts a limit, *V*, on the amount of the material available, so that the minimum compliance design is for a fixed volume. The tensor E^0_{ijkl} is the stiffness tensor for the given isotropic material, in this case Silicon. Using equation (6.7), we can now write the "0 – 1" form of (6.5) as

$$\min \;\; f^T u \tag{6.8}$$

$$s.t.: \left(\sum_{e=1}^{N} \rho_e K_e\right) u = f,$$

$$E_e = \rho_e E^0_e\,, \qquad \rho_e = \begin{cases} 1 \;\; if \; e \in \Omega^{opt} \\ 0 \;\; if \; e \in \Omega \backslash \Omega^{opt} \end{cases}$$

$$\sum_{e=1}^{N} v_e \rho_e = Vol(\,\Omega^{opt}) \leq V'$$

where ρ_e is the density of the element, and v_e is the volume of that particular element.

6.1.1.3 Penalized Density Form

The most commonly used approach to solve the above problem is to replace the integer variables with continuous variables and then introduce some form of penalty that steers the solution to discrete 0-1 values. The design problem for the fixed domain is formulated by modifying the stiffness matrix so that it depends continuously on the density of the material [103], [106] – [108]. This density function is the design variable. The requirement is that the optimization results in designs consisting almost entirely of regions of material or no material. That means the intermediate values of the density function should be penalized in a manner analogous to the continuous optimization approximations of 0-1 problems. The penalty form of (6.8) can be written as

$$\min \; f^T u \tag{6.9}$$

$$s.t.: \left(\sum_{e=1}^{N} \rho_e^p K_e\right) u = f, \qquad E_e = \rho_e^p E_e^0, \quad p > 1$$

$$\sum_{e=1}^{N} v_e \rho_e \leq V', \qquad 0 \leq \rho_e \leq 1$$

The density interpolates between the material properties 0 and E_e^0 such that

$$E_e\,(\rho_e = 0) = 0, \qquad E_e\,(\rho_e = 1) = E_e^0$$

6.1.2 Optimality Conditions

In this section, we will find the necessary conditions of optimality for the density ρ of the minimum compliance design problem, using Optimality Criteria (OC) method. The OC method has been used in the literature [103], [109] – [113] to solve several structural optimization problems. We will consider a simple continuum structure with single load problem. To proceed, we first recapitulate the mathematical form described in (6.4) with density interpolation function as

$$\min \; l(u), \qquad for\ all \;\; u \in U, E \tag{6.10}$$

$$s.t.: \; a_E(u,v) = l(v), \qquad for\ all \;\; v \in U$$

$$E_{ijkl}(x) = \rho(x)^p E^0_{ijkl},$$

$$\int \rho(x)\, d\Omega \leq V', \qquad 0 < \rho_{min} \leq \rho_e \leq 1$$

Note that a lower bound ρ_{min} is introduced on the density in order to prevent any possible singularity of the equilibrium problem. For the problems considered here, we set a typical value of $\rho_{min} = 10^{-3}$.

Assuming Lagrange multipliers $\Lambda, \lambda^{-}, \lambda^{+}$ for the constraints of (6.10), the Lagrange function is given as [103] – [108]

$$\begin{aligned}\mathcal{L} = l(u) + \{a_E(u,\ \bar{u}) - l(\bar{u})\} \\ + \Lambda\left(\int \rho(x)d\Omega - V'\right) \\ + \int \lambda^{-}\left(\rho_{min} - \rho(x)\right)d\Omega \\ + \int \lambda^{+}(\rho(x) - 1)d\Omega \end{aligned} \tag{6.11}$$

where $\bar{u}$ is the Lagrange multiplier for the equilibrium constraint [103] – [108]. Note that the $\bar{u}$ belongs to the set *U* of kinematically admissible displacement fields. Under the equilibrium and with unique displacement fields, the conditions for optimality with respect to variations of the displacement field *u* give that $u = \bar{u}$. The conditions for optimality with respect to variations of the density ρ, can be found by taking the derivative of the Lagrange function $\mathcal{L}$ with respect to the design variable ρ and equating it to zero, shown as

$$-\frac{\partial E_{ijkl}}{\partial \rho}\,\varepsilon_{ij}(u)\varepsilon_{kl}(u) = \Lambda + \lambda^{-} - \lambda^{+} \tag{6.12}$$

with the switching conditions

$$\lambda^- \geq 0, \qquad \lambda^+ \geq 0, \quad \lambda^-\big(\rho_{min} - \rho(x)\big) = 0, \quad \lambda^+(\rho(x) - 1) = 0 \tag{6.13}$$

Equation (6.13) can be interpreted as follows. When the value of $\rho(x)$ is at the lower limit, ρ_{min}, then the equation, $\lambda^-\big(\rho_{min} - \rho(x)\big) = 0$, holds true, because $\lambda^- \geq 0$. Similar explanation can be provided for $\lambda^+(\rho(x) - 1) = 0$. However, when the value of $\rho(x)$ is in between the lower and upper limit, that is $\rho_{min} < \rho(x) < 1$, then λ^- and λ^+ have to be equal to zero to hold the equation (6.13) true. That means, for intermediate densities, ($\rho_{min} < \rho(x) < 1$), the optimality conditions (6.12), can be written as

$$-\frac{\partial E_{ijkl}}{\partial \rho}\, \varepsilon_{ij}(u)\varepsilon_{kl}(u) = \Lambda \tag{6.14}$$

Or,

$$-p\rho(x)^{p-1}\, E^0_{ijkl}\varepsilon_{ij}(u)\varepsilon_{kl}(u) = \Lambda \tag{6.15}$$

The equation (6.15) can be written in the discrete form as

$$-\sum_{e=1}^{N} p\rho_e^{p-1}\, u^T K_e u = \Lambda \tag{6.16}$$

To solve the minimum compliance problem by a mathematical programming algorithm, we rewrite the problem in the design variables only:

$$\min \quad c(\rho_e)$$

$$s.t.: \sum_{e=1}^{N} v_e \rho_e \leq V', \qquad 0 < \rho_{min} \leq \rho_e \leq 1 \tag{6.17}$$

$$where, \quad c(\rho_e) = f^T u = \sum_{e=1}^{N} \rho_e^p \, u^T K_e u \tag{6.18}$$

$$where, \quad u \; solves: \qquad \sum_{e=1}^{N} \rho_e^p \, K_e u = f \tag{6.19}$$

Or,

$$\min \quad \sum_{e=1}^{N} \rho_e^p \, u^T K_e u \qquad where, \quad u \; solves: \qquad \sum_{e=1}^{N} \rho_e^p \, K_e u = f$$

$$s.t.: \sum_{e=1}^{N} v_e \rho_e \leq V', \qquad 0 < \rho_{min} \leq \rho_e \leq 1 \tag{6.20}$$

The formulation given in equation (6.20) will be considered in the rest of the chapter as a form for solving topology optimization problem.

A fixed-point type density update scheme for the minimum compliance problem has been devised by Bendsoe and Sigmund [103], [104] and is given as

$$\rho_{k+1} = \begin{cases} \max\{(1-\zeta)\rho_k, \rho_{min}\} & if \;\; \rho_k B_k^{\eta} \;\leq\; \max\{(1-\zeta)\rho_k, \rho_{min}\} \\ \min\{(1-\zeta)\rho_k, 1\} & if \;\; \min\{(1+\zeta)\rho_k, 1\} \;\leq\; \rho_k B_k^{\eta} \\ \rho_k B_k^{\eta} & Otherwise \end{cases} \tag{6.21}$$

Here ρ_k denotes the value of the density variable at iteration step k, and B_k is given by the expression (6.22) [103], [104]

$$B_k \Lambda = -\sum_{e=1}^{N} p\rho_e^{p-1} u^T K_e u \tag{6.22}$$

The update scheme (6.21) adds material to areas with a specific strain energy that is higher than Λ (that is, when $B_k > 1$) and removes it if the energy is below this value, while keeping the bound constraint of the density ρ intact. The variable η in (6.21) is a tuning parameter and ζ a move limit. Both controls the changes that can happen at each iteration step and they can be adjusted for efficiency of the method. The values of η and ζ are chosen by experiment [103], [104], in order to obtain a suitable rapid and stable convergence of the iteration scheme. A typical value of η and ζ is 0.5 and 0.2 respectively.

6.1.3 Implementation Steps

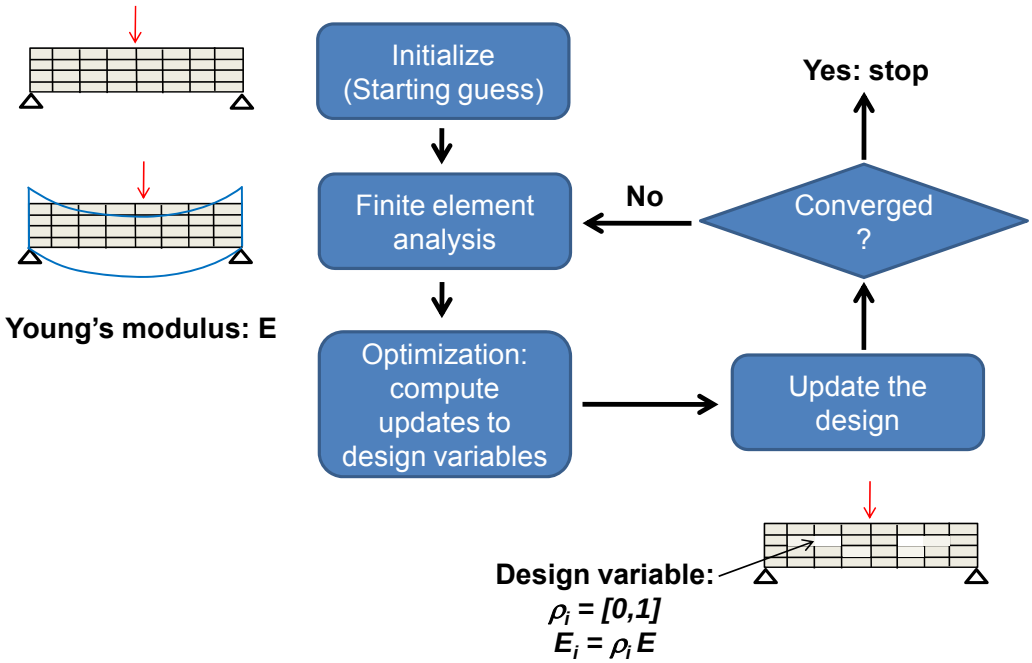

Fig. 6.2: Flow chart for the implementation of the topology optimization.

1. Guess a suitable initial reference domain which can encompass the final desired shape. The material of the domain is assumed to be homogeneously distributed.
2. Discretize the domain into finite elements and apply the load and boundary conditions as per the design requirements. The finite element mesh should be fine enough in order to describe the structure in a reasonable resolution bit-map representation. The mesh is unchanged through-out the design process.
3. The iterative part of the algorithm is then:

4. For the initial homogenous distribution of density, compute by the finite element method the resulting displacements and strain energy.
5. Compute the compliance of the design. If only marginal improvement (in compliance) over the last design, stop the iterations. Else, continue.
6. Compute the update of the density variable, based on the update scheme shown in equation (6.21). This step also consists of an inner loop for finding the value of the Lagrange multiplier Λ for the volume constraint. The density update makes sure that the meshed element is converted to void $\rho = 0$ where the material is not required and to $\rho = 1$ where the material is required. The density vector stores the density values of all the elements of the discretized structure.
7. Repeat the iteration loop.
8. Interpret the distribution of material to define the final shape from the black-white representation of the bit-map image.

The above implementation steps were used to do the stiffness optimization for a short cantilever. We started with a square starting domain as shown in Fig. 6.3, and then applied a single vertical load at the center of the cantilever. We then performed the topology optimization procedure outlined in the above implementation steps with the volume condition of 60%. That means the density vector of the structure will be changed while removing 40% of the material and keeping the volume at around 60% of the initial volume. Fig. 6.3 shows the resulting change in shapes with increasing iterations. The initial domain must be larger than the final shape so that there is a room to play around with the density vector in the algorithm. If the volume condition is set at

100%, then the algorithm will assign the density $\rho = 1$ to the every element, and since it meets the volume constraint of 100% no element (pixel) will be changed to any other density leading to a deadlock and resulting in no-change in the shape for subsequent iterations.

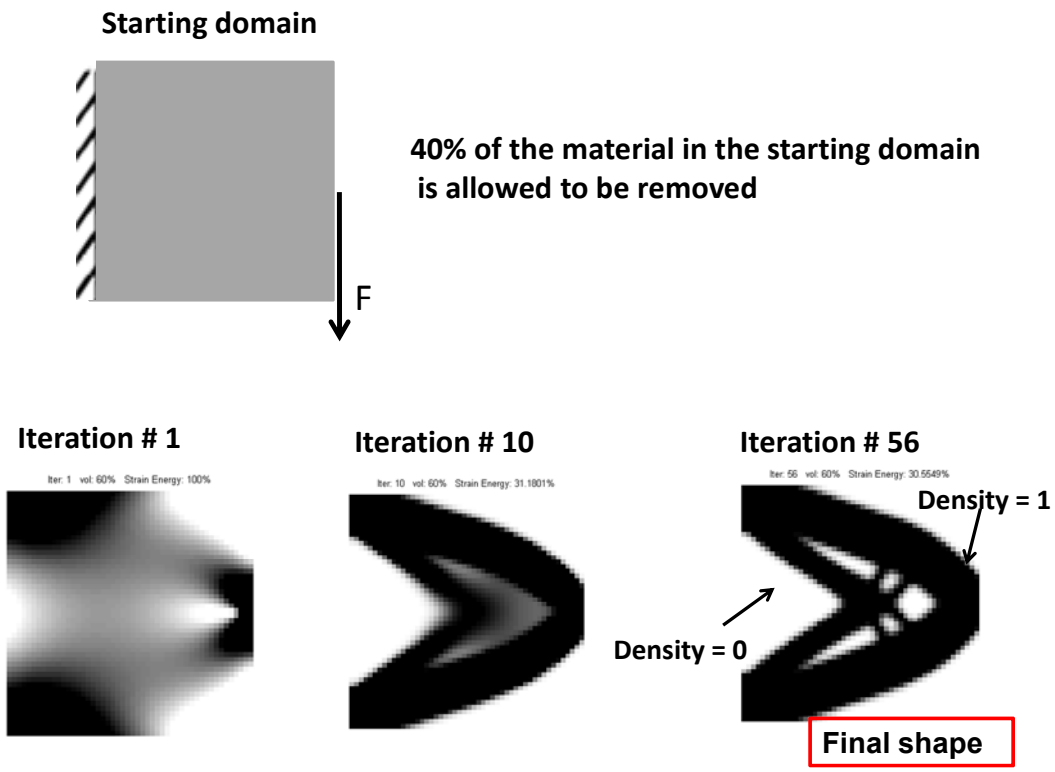

Fig. 6.3: The starting domain (top) which is based on a clever guess on the assumption that the final shape is enclosed in it. The change in the distribution of the black-white pattern is shown (bottom) after iteration number 1, 10 and 56 leading to the final shape.

It has been shown in the literature [107], [113], [115] – [118] that the above optimization technique may provide global optimum solution for a simple cantilever beam under certain circumstances where the error due to discretization and FEM is small.

It is also very simple to extend the algorithm to account for multiple load cases. In fact, this can done by just modifying the objective function as the sum of multiple compliances [103], [104], [114], as shown in equation (6.23).

$$c(x) = \sum_{i=1}^{n} u_i^T K u_i \qquad (6.23)$$

where *n* denotes the total number of loads applied to the structure.

We will now use this technique to design the support of the resonator for better mechanical isolation.

6.2 Resonator Support Design

We need to design the support of the resonator in such a way that it can overcome the external impact. The effect of the impact can be modeled as the forces experienced by the resonator as shown in Fig. 6.4. Reaction forces and local moments are created at the support anchors on both sides (double anchored) of the resonator to counter balance the

impact forces (Fig. 6.4). These reaction forces can then be used in the optimization algorithm to find the stiffer shape of the support structure for better mechanical isolation.

We start with a rectangular domain as a guess as shown in Fig. 6.5 assuming that the final structure will lie within this domain, and then apply the reaction forces. The topology optimization algorithm results into the final shape which is similar to the 2-bar frame with 90° angle (Fig. 6.5) which has been analytically proven to be optimally stiff [107], [113], [115] – [118]. The reason behind the 2-bar frame being optimally stiff, is its ability to decompose the applied load into two perpendicular components, i.e., either tension or compression in this case. The load bearing capacity of any structure increases if it is either on tension or on compression compared to that of bending.

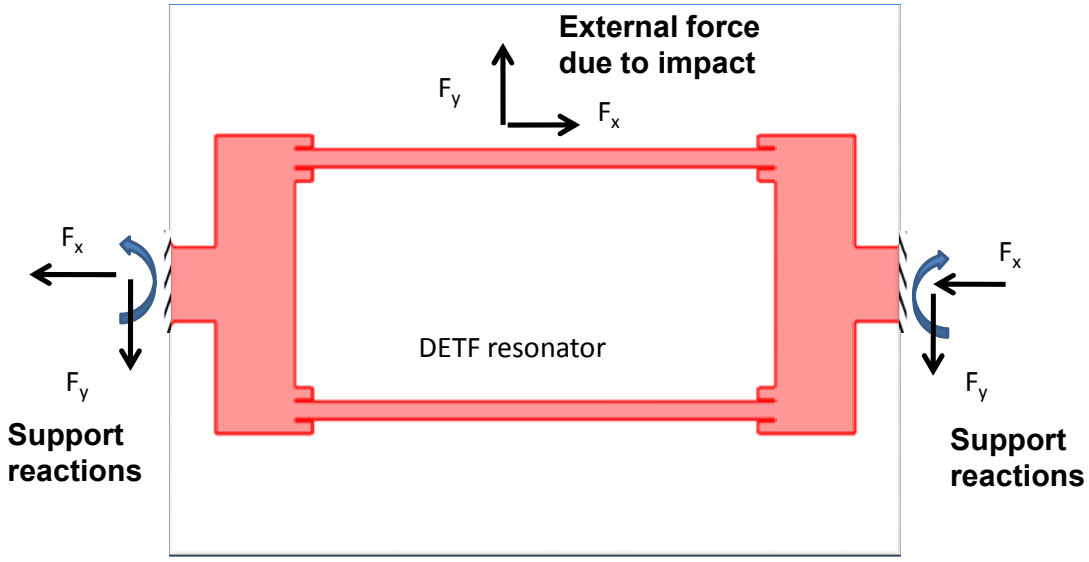

Fig. 6.4: Modeling of the external impact forces and the resulting reaction forces at the support anchors.

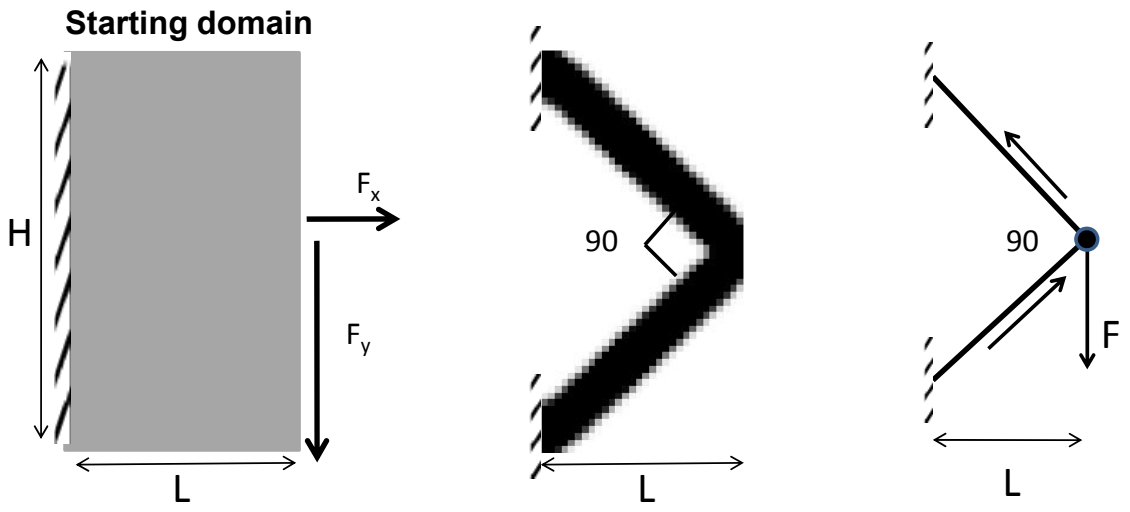

(a) *(b)* *(c)*

Fig. 6.5: (a) Starting domain for the resonator support structure assuming that the final shape of the structure will lie within this domain. (b) Final shape obtained using the topology optimization algorithm. (c) Analytically proven shape of 2-bar frame with 90° angle for optimal stiffness.

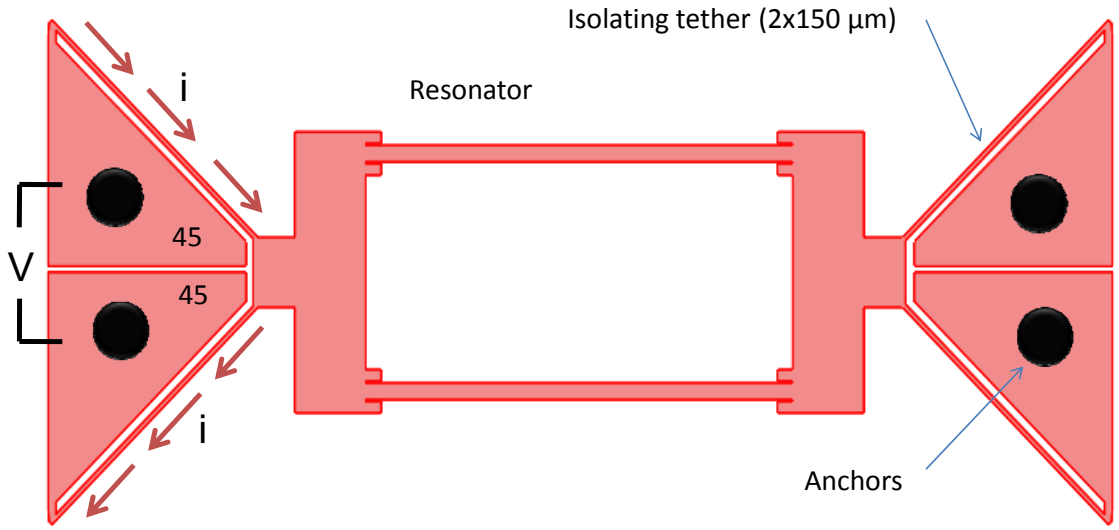

Fig. 6.6: Resonator with 2-bar isolating tether which acts as anchor support with 90° angle between them.

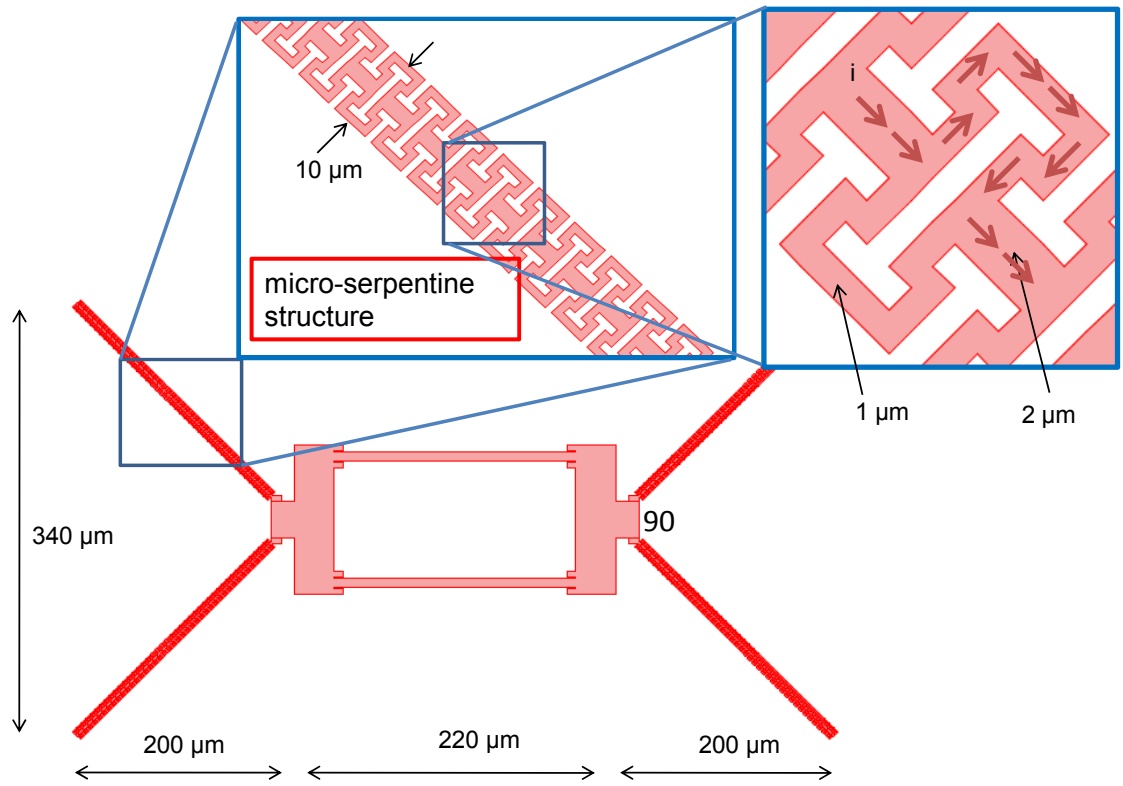

Fig. 6.7: Resonator with 2-bar isolating tether having micro-serpentine structure for increased thermal resistance of approximately 300,000 K/W. (The anchors are not shown in the above figure for better clarity).

We now apply this two bar structure in designing the resonator support as shown in Fig. 6.6. Two thin tethers at 90° angle on either side of the resonator act as support anchors, and one of them can be used as an in-built heater, similar in principle described in chapter 4. However, there is one drawback with this design. The thermal resistance of the in-built heater is too low (60,000 K/W) and is dependent on the length of the tether which is limited by the footprint of the device. Typically, it is desired to have as small

footprint as possible to increase the number count of the device per wafer. In this work, we limit the maximum size of the die to 1mm x 1mm, which in turn limits the footprint size. To increase the thermal resistance of the 2-bar in-built heater, a micro-serpentine structure is created as shown in Fig. 6.7. The micro-serpentine structure increases the length of electric-current-path, thus increasing the thermal resistance, without increasing the overall length of the tether. The thermal resistance of the in-built heater for this improved design is approximately 300,000 K/W.

Table 6.1: Comparison of thermal and mechanical characteristic of different designs

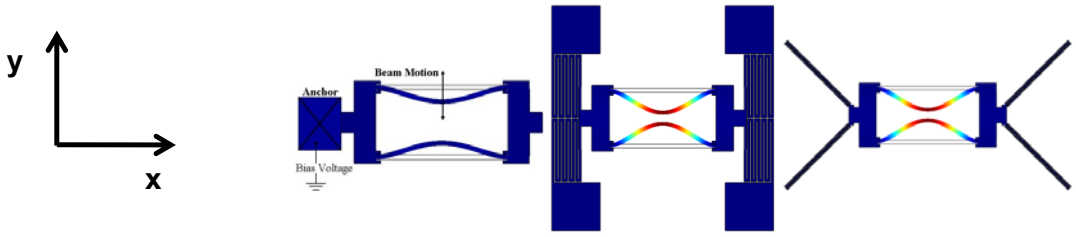

Description	Standard design	Thermally isolated design	Improved * Design
Acceleration sensitivity (Γ_f)	**7.5 ppb / g**	**0.15 ppb / g**	**0.15 ppb / g**
Acceleration sensitivity (Γ_u)	**1.5 x 10^{-11} m/g (z axis)**	**1.5 x 10^{-10} m/g (x axis)**	**2.0 x 10^{-11} m/g**
Vibration induced noise at 100Hz offset	**- 80 dBc**	**- 115 dBc**	**-115 dBc**
Natural frequency	**145 KHz**	**45 KHz**	**110 KHz**
Power consumption	**200 mW**	**12 mW**	**5 mW**
Thermal time constant	**500 mS**	**10 mS**	**15 mS**

* z-axis data not available

With such a high thermal resistance, the power consumption to increase the resonator temperature for 125°C reduces to 5mW; and the thermal time constant marginally increases to 15ms. At the same time, its deformation acceleration sensitivity, Γ_u, has increased by 10x compared to the thermally isolated design. A comparison of thermal and mechanical characteristics for standard DETF resonator, thermally isolated resonator, and the improved design is presented in Table 6.1. As can be seen, the improved design is better than the previously described thermally isolated design (chapter 4) on all counts.

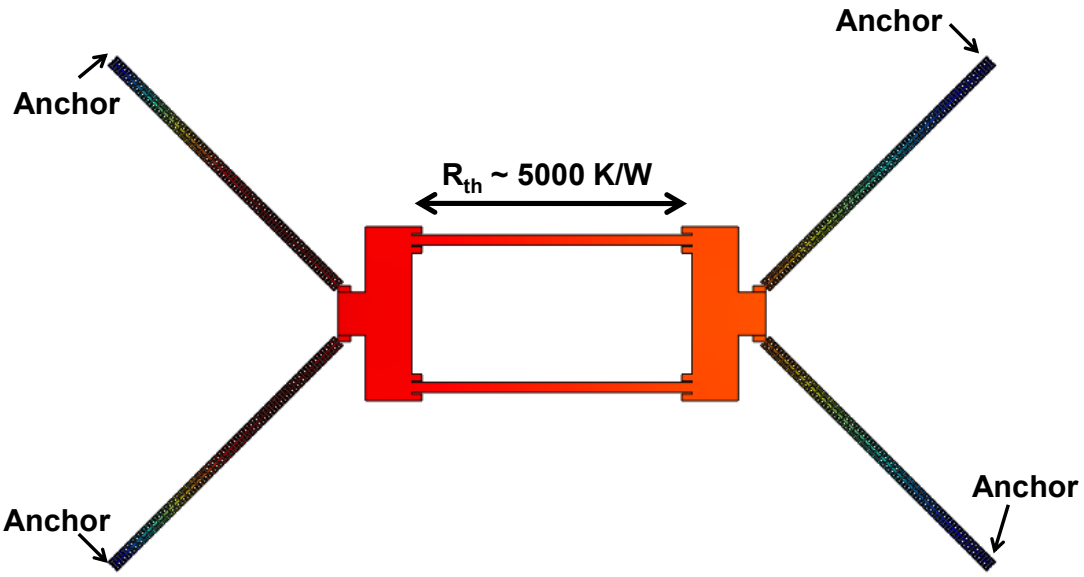

Fig. 6.8: Finite Element simulation of the resonator with improved thermal isolation design showing temperature gradient across the length of the resonator beam. The temperature gradient is proportional to the thermal resistance of the beam and the applied heating voltage across the anchors.

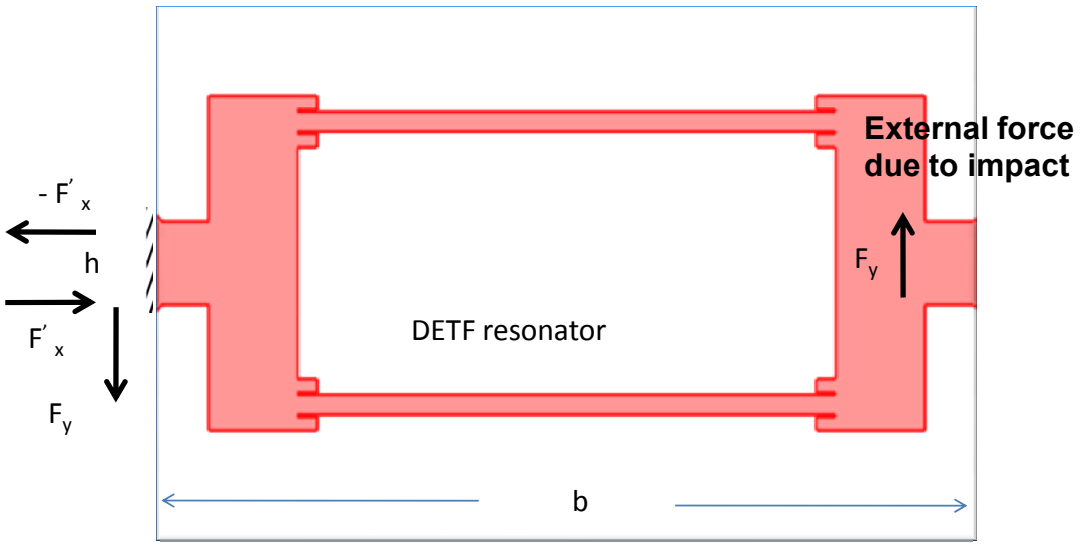

$$F'_x = \frac{b}{h} F_y$$

Fig. 6.9: A schematic of the force balance in the single-anchored resonator due to external impact. A couple, at the anchor, is required to counter balance the impact.

However, there is one disadvantage associated with this type of design. Since the 2-bar tether-based anchor supports are on both sides of the resonator, there is a temperature gradient across the length of the resonator beam as shown in Fig. 6.8, which depends on the thermal resistance of the beam and the applied voltage. The temperature gradient may be undesirable for many frequency reference applications. To solve this problem, we need to design a single-side-anchor resonator. We follow similar steps as in the design of the double-side-anchored resonator described above. A model for the reaction forces due to external impact on the single side anchor resonator is shown in Fig. 6.9. A couple, at the anchor, is required to counter balance the impact. We use these reaction

forces to find the shape of the support structures from the topology optimization algorithm. The resultant shape is implemented into the design of the resonator as shown in Fig. 6.10. In this design, four tether supports are required. Two of them, at 90° angle, are similar to the 2-bar structure described in the previous design. The remaining two tethers (Fig. 6.10) support a couple needed to counter balance the bending force due to the impact on the resonator as explained in Fig. 6.9. The micro-serpentine structure is used to increase the thermal resistance to approximately 300,000 K/W.

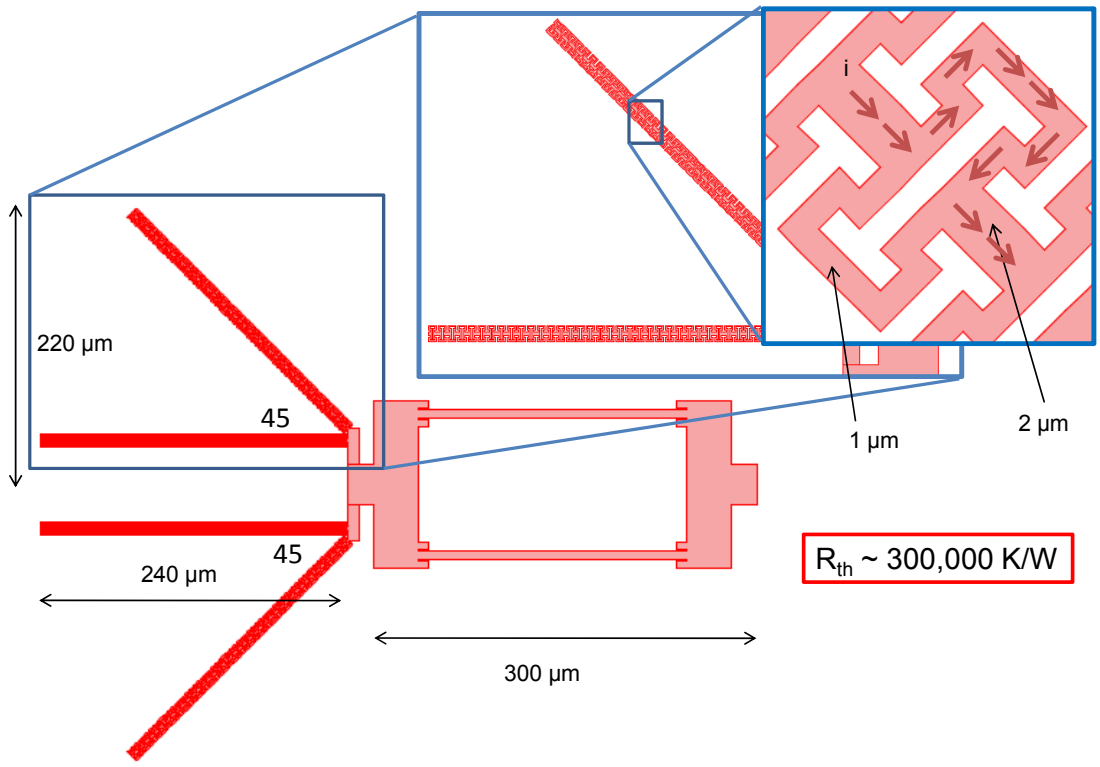

Fig. 6.10: Resonator with single-side anchors with tethers having micro-serpentine structure for increased thermal resistance of approximately 300,000 K/W. (The anchors are not shown in the above figure for better clarity).

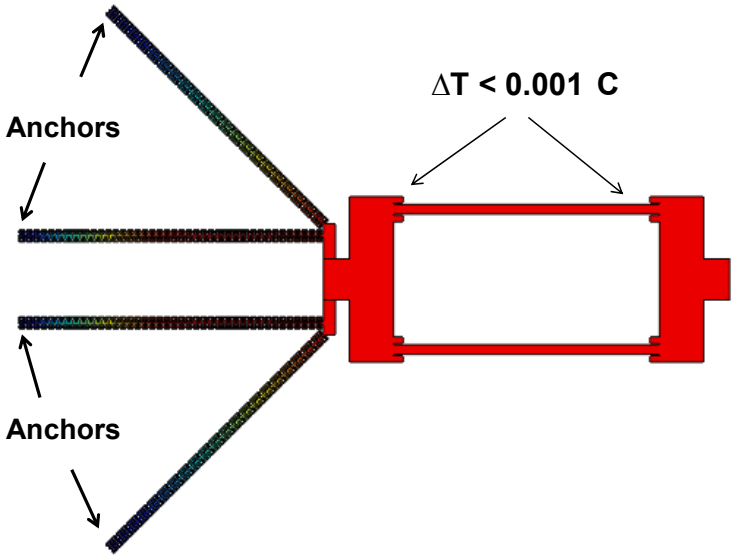

Fig. 6.11: Finite element simulation of the single-sided anchor resonator design showing uniform temperature across the length of the resonator beam.

Table 6.2: Comparison of thermal and mechanical characteristic of all designs

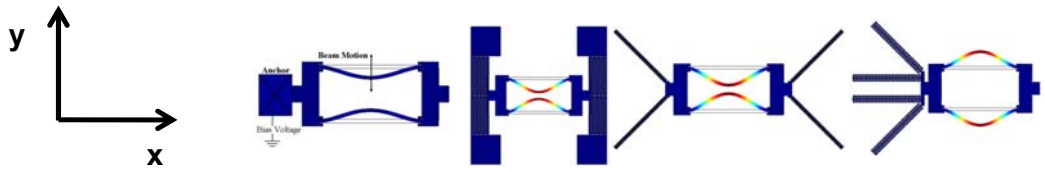

Description	Standard design	Thermally isolated design	Improved * design - 1 (double end)	Improved * design -2 (single end)
Acceleration sensitivity (Γ_f)	**7.5 ppb / g**	**0.15 ppb / g**	**0.15 ppb / g**	**7.5 ppb / g**
Acceleration sensitivity (Γ_u)	**1.5 x 10^{-11} m/g (z axis)**	**1.5 x 10^{-10} m/g (x axis)**	**2.0 x 10^{-11} m/g**	**1.5 x 10^{-10} m/g (y axis)**
Vibration induced noise at 100Hz offset	**- 80 dBc**	**- 115 dBc**	**-115 dBc**	**-80 dBc**
Natural frequency	**145 KHz**	**45 KHz**	**110 KHz**	**40 KHz**
Power consumption	**200 mW**	**12 mW**	**5 mW**	**5 mW**
Thermal time constant	**500 mS**	**10 mS**	**15 mS**	**15 mS**

* z-axis data not available

The purpose of this design is to keep the temperature of the resonator uniform when applying the heating voltage. A finite element simulation (Fig. 6.11) shows that the temperature across the resonator beam is uniform and is within 0.001°C.

However, since the design is single-side anchored, it is more flexible and hence its deformation acceleration sensitivity, Γ_u, has reduced by approximately 10x as compared to the double-side-anchor design. The comparison table 6.2 describes the thermal and mechanical characteristics of all the designs.

It is to be noted here that the topology optimization technique discussed in this chapter has been applied only to find the shape of the structure for maximum stiffness. Our goal was to find the shape of the structure which could optimize both stiffness and thermal resistance simultaneously. However, it is difficult to analytically model both the stiffness and the thermal resistance simultaneously for the topology optimization approach described above, and may require a dedicated research. It is for this reason, the resonator support design was split into two parts namely stiffness design and the micro-serpentine design for the thermal resistance, to improve the design as thermally and mechanically isolated.

Chapter 7

Conclusions and Future Directions

7.1 Conclusions

In this dissertation, we have presented a technique for high resolution digital temperature sensor [121], and thermal as well as mechanical isolation of the resonator [56], [99]. Temperature sensing, thermal isolation and mechanical isolation play important role in the design of the ovenized silicon micro-mechanical resonator. The digital temperature sensing technique, described in this work, removes the thermal lag between the temperature sensor and the resonator. This is crucial in achieving high precision oven control of the resonator. At the same this sensor can be used as a general purpose CMOS digital temperature sensor. Thermal isolation is required to reduce the power consumption and improve the dynamic thermal response of the ovenized resonator. An overall improvement of approximately 40x and 50x in the power consumption and the thermal time constant, respectively, have been achieved. An analysis and improvement of the mechanical isolation of the resonator has also been described. Topology optimization was used for simultaneous improvement of the mechanical and thermal isolation of the resonator.

7.2 Future Directions

The topology optimization technique, described in this work, can also be used for various other applications. MEMS vibration energy scavenging device is one such field where we tried to investigate the opportunity of using design optimization to improve the performance. It has been shown in the past [119] that sufficient power (upto 200 $\mu W/cm^3$) can be generated from ambient vibrations to power micro-sensors. For example, a micro pressure sensor requires as low power as 2μW [120].

We take a look at the vibrations in a running car. The hypothesis is to power sensors in a typical mid-size car from its vibration. We measured the vibration of the car using three different accelerometers (Fig. 7.1) attached at different locations of the car. Among all the locations measured, we found the vibration of engine cover to be useful from the energy scavenging point of view (Fig. 7.2 and 7.3), where it is possible to tap the vibration energy using a MEMS scavenger and power the micro-sensors.

Fig. 7.1: Vibration measurement of a running (engine turned on) car by attaching accelerometers at various locations.

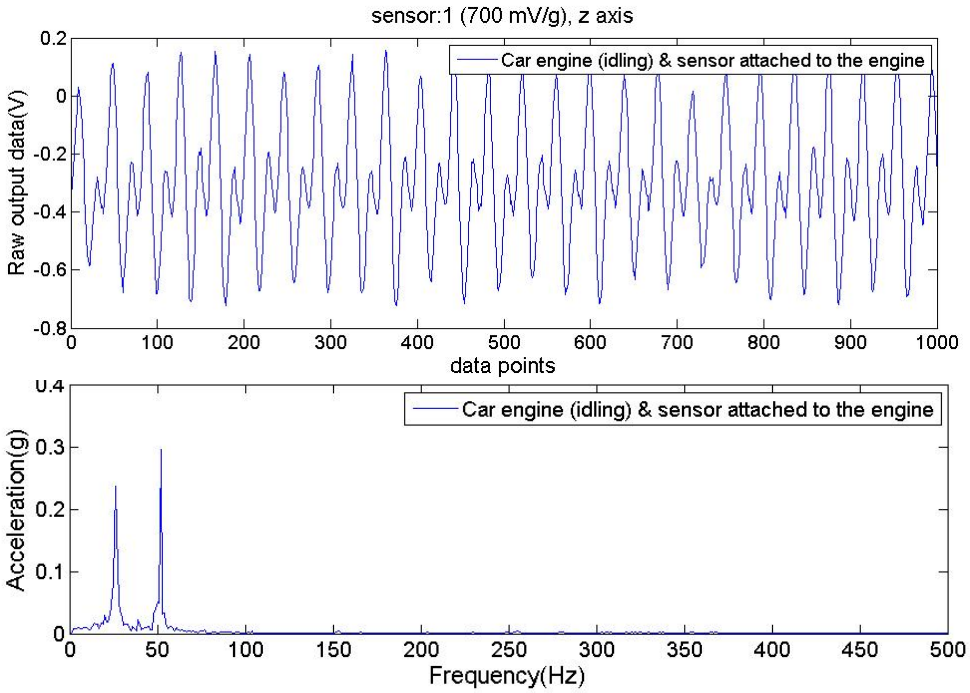

Fig. 7.2: Vibration spectrum output when the engine was idling and the accelerometers were attached at the engine cover.

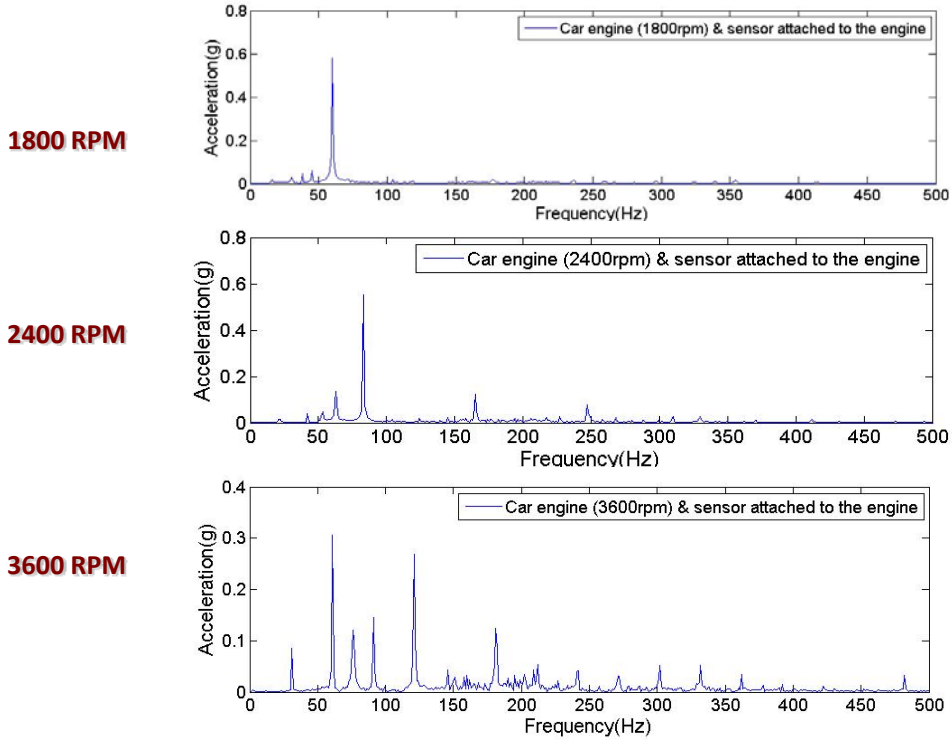

Fig. 7.3: Vibration spectrum output at different engine speeds (rpm).

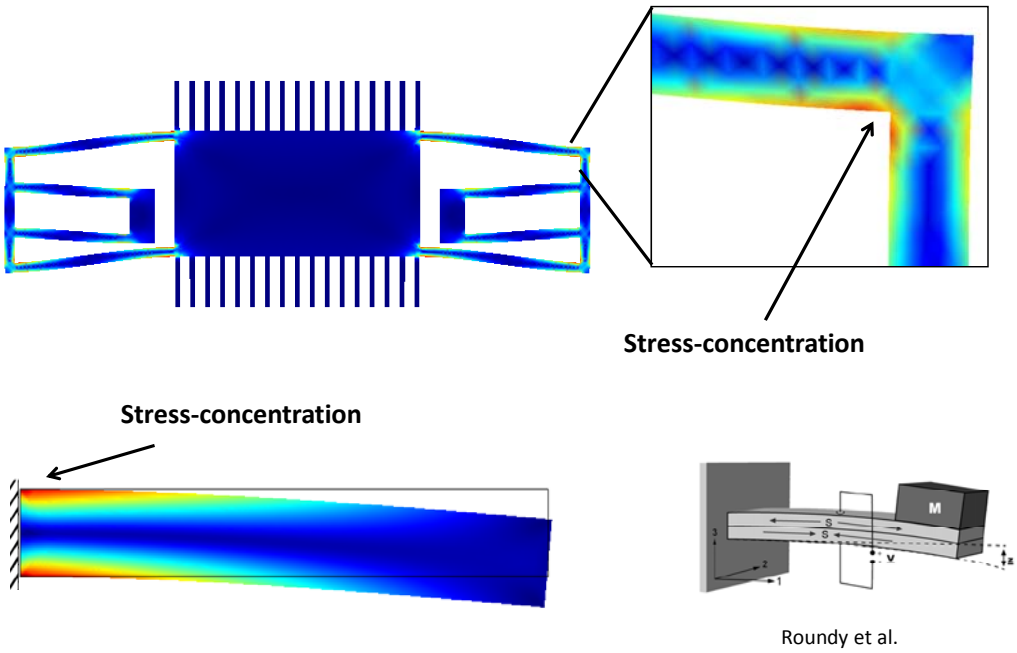

Fig. 7.4: FEM simulation showing stress concentration on the designs normally used for energy scavenging.

A finite element simulation of some of the typical designs normally used in the literature [119] are shown in Fig. 7.4. These designs are rectangular in nature and are more likely to fail due to stress concentration. Since vibration energy scavenging device are meant to operate continuously for long period of time (10 – 15 years) without failure, it becomes very important to design the device free from any stress concentration.

At the same time, the efficiency of the piezoelectric vibration energy scavenger depends on the stress generated in the beam due to the vibration, and hence there has to be an optimal stress for a given design of the energy scavenging device. Design (Topology) optimization can be used to improve the reliability and efficiency of such devices and hence can be a meaningful future direction.

References

[1] J. James, and J. Fitz-Randolph, “From Sundials to Atomic Clocks: Understanding Time and Frequency,” 2nd (revised) edition, Mineola, New York: Dover Publications, 1999.

[2] A NIST Physics Laboratory http://physics.nist.gov/time

[3] J. James, B. E. Blair, and L. E. Gatterer, “Characterization and Concepts of Time-Frequency Dissemination,” Proceedings of the IEEE, vol.60, no. 5, May 1972.

[4] W. A. Marrison, and J.W. Horton, "Precision determination of frequency," I.R.E. Proc. 16, 137–154, February, 1928.

[5] W. A. Marrison, “The Evolution of the Quartz Crystal Clock," Bell System Technical Journal 27, 510–588, AT&T, 1948.

[6] M. E. Frerking, Crystal Oscillator Design and Temperature Compensation, New York, Van Nostrand, 1978.

[7] R. L. Filler, and J. R. Vig, "Resonators for the Microcomputer Compensated Crystal Oscillator," 43rd Annual Symposium on Frequency Control, 1989.

[8] E. Jackson, and B. Rose, "The Microprocessor Compensated Crystal Oscillator – New Developments," IEEE, IFCS, 1999.

[9] M. Bloch, M. Meirs, and J. Ho, "The Microcomputer Compensated Crystal Oscillator (MCXO)," 43rd Annual Symposium on Frequency control, 1989.

[10] A. Benjaminson, and S. C. Stallings, "A Microcomputer-Compensated Crystal Oscillator using a Dual-Mode Resonator," 43rd Annual Symposium on Frequency control, 1989.

[11] J. R. Vig, “Temperature-insensitive dual-mode resonant sensors—A review,” IEEE Sensors J., vol. 1, no. 1, pp. 62–68, Jun. 2001.

[12] R. L. Filler, and J. R. Vig, “Resonators for the microcomputer compensated crystal oscillator,” in Proc. 43rd Annu. Freq. Control Symp., pp. 8–15, 1989.

[13] J. R. Vig, “Temperature stable crystal oscillator,” IEEE Trans. Ultrason., Ferroelectr., Freq. Control, vol. 42, no. 4, pp. 797–799, Jul. 1995.

[14] A. Ballato, and J. R. Vig, “Static and dynamic frequency-temperature behavior of singly and doubly rotated, oven-controlled quartz resonators,” in Proc. 32nd FCS, pp. 180–188, AD-A955 718, 1978.

[15] I. Balaz, and M. Minarik, “Towards an OCXO with infrared heater,” in Proc. IEEE Int. FCS, pp. 674–680, 1996.

[16] M. Vaish, “A high precision quartz oscillator with performance comparable to rubidium oscillators in many respects,” in Proc. IEEE Int. FCS, pp. 752–760, 1996.

[17] Vectron International, C4550 OCXO. http://www.vectron.com

[18] F. G. Major, The Quantum Beat – The Physical Principles of Atomic Clocks, Springer, Verlag, 1998.

[19] J. Vanier, and C. Audoin, The Quantum Physics of Atomic Frequency Standards, ISBN, 0-85274-434-X, Adam Hilger, 1978.

[20] L. L. Lewis, “An Introduction to Frequency Standards,” Proc. IEEE, vol. 79, pp. 927-935, 1991.

[21] P. Forman, "Atomichron: The Atomic Clock from Concept to Commercial Product," Proc. of the IEEE, Vol. 73, No. 7, pp. 1181-1204, July 1985.

[22] C. T.-C. Nguyen, “MEMS technology for timing and frequency control,” IEEE Trans. Ultrason., Ferroelectr., Freq. Control, vol. 54, no. 2, pp. 251–270, Feb. 2007.

[23] V. Kaajakari, J. Kiihamaki, A. Oja, S. Pietikainen, V. Kokkala, and H. Kuisma, “Stability of wafer level vacuum encapsulated single-crystal silicon resonators,” Sens. Actuators A, Phys., vol. 130/131, pp. 42–47, Aug. 2006.

[24] C. T.-C. Nguyen, and R. T. Howe, “An integrated CMOS micromechanical resonator high-Q oscillator,” IEEE J. Solid-State Circuits, vol. 34, no. 4, pp. 440–455, Apr. 1999.

[25] D. Sparks, S. Massoud-Ansari, and N. Najafi, “Chip-level vacuum packaging of micromachines using nanogetters,” IEEE Trans. Adv. Packag., vol. 26, no. 3, pp. 277–282, Aug. 2003.

[26] W.-T. Hsu, and C. T.-C. Nguyen, “Stiffness-compensated temperature insensitive micromechanical resonators,” in Proc. IEEE MEMS, pp. 731–734, 2002.

[27] E. P. Quevy, and R. T. Howe, “Redundant MEMS resonators for precise reference oscillators,” in Proc. IEEE Radio Freq. Integr. Circuits Symp., pp. 113–116, 2005.

[28] M. A. Hopcroft, M. Agarwal, K. K. Park, B. Kim, C. M. Jha, R. N. Candler, G. Yama, B. Murmann, and T. W. Kenny, “Temperature compensation of a MEMS resonator using quality factor as a thermometer,” in Proc. 19th IEEE Int. Conf. MEMS, pp. 222–225, Jan. 2006.

[29] C. T.-C. Nguyen, "Frequency-selective MEMS for miniaturized low-power communication devices," IEEE Transactions on Microwave Theory and Techniques, vol. 47, pp. 1486-1503, 1999.

[30] J. W. Weigold, A.-C. Wong, C. T.-C. Nguyen, and S. W. Pang, "A merged process for thick single-crystal Si resonators and BiCMOS circuitry," IEEE Journal of Microelectromechanical Systems, vol. 8, pp. 221-228, 1999.

[31] R. A. Buser, and N. F. de Rooij, "Resonant silicon structures," Sensors and Actuators, vol. 17, pp. 145-154, 1989.

[32] G. Stemme, "Resonant silicon sensors," Journal of Micromechanics and Microengineering, vol. 1, pp. 113, 1991.

[33] R. N. Kleiman, G. K. Kaminsky, J. D. Reppy, R. Pindak, and D. J. Bishop, "Single-crystal silicon high-Q torsional oscillators," Review of Scientific Instruments, vol. 56, pp. 2088-2091, 1985.

[34] R. T. Howe, and R. S. Muller, "Resonant-microbridge vapor sensor," IEEE Transactions on Electron Devices, vol. 33, pp. 499-506, 1986.

[35] T. P. Burg, A. R. Mirza, N. Milovic, C. H. Tsau, G. A. Popescu, J. S. Foster, and S. R. Manalis, "Vacuum-Packaged Suspended Microchannel Resonant Mass Sensor for Biomolecular Detection," Journal Microelectromechanical Systems, vol. 15, pp. 1466-1476, 2006.

[36] P. Parsons, A. Glendinning, and D. Angelidis, "Resonant sensors for high accuracy pressure measurement using silicon technology," presented at National Aerospace and Electronics Conference, NAECON., Proceedings of the IEEE 1992.

[37] E. Stemme, and G. Stemme, "A Balanced Resonant Pressure Sensor," Sensors and Actuators A: Physical, vol. 21, pp. 336-341, 1990.

[38] J. C. Greenwood, "Silicon in mechanical sensors," Journal of Physics E: Scientific Instruments, pp. 1114-1128, 1988.

[39] T. A. W. Roessig, Integrated MEMS Tuning Fork Oscillators for Sensor Applications, thesis in Mechanical Engineering at University of California, Berkeley, 1998.

[40] W. Yun, R. T. Howe, and P. R. Gray, "Surface micromachined, digitally force-balanced accelerometer with integrated CMOS detection circuitry," presented at Hilton Head, the IEEE Solid-State Sensor and Actuator Workshop, Hilton Head, SC USA, 1992.

[41] H. C. Kim, S. Seok, I. Kim, S.-D. Choi, and K. Chun, "Inertial-Grade Out-of-Plane and In-Plane Differential Resonant Silicon Accelerometers (DRXLs)," presented at TRANSDUCERS '05, Solid-State Sensors, Actuators and Microsystems, Seoul, 2005.

[42] W.-T. Hsu, J. R. Clark, and C. T.-C. Nguyen, "A resonant temperature sensor based on electrical spring softening," presented at TRANSDUCERS '01 / Eurosensors XV, The 11th International Conference on Solid-State Sensors and Actuators, Munich, Germany, 2001.

[43] L. Lin, R. T. Howe, and A. P. Pisano, "Microelectromechanical filters for signal processing," Journal of Microelectromechanical Systems, vol. 7, pp. 286-294, 1998.

[44] C. T.-C. Nguyen, "Microelectromechanical devices for wireless communications," MEMS '98, 11th Annual International Workshop on Micro Electro Mechanical Systems, Heidelberg, Germany, 1998.

[45] Q. Zhong, D. Inniss, K. Kjoller, and V. B. Elings, "Fractured polymer/silica fiber surface studied by tapping mode atomic force microscopy," Surface Science, vol. 290, pp. 688-692, 1993.

[46] B. Kim, M. Hopcroft, C. M. Jha, R. Melamud, S. A. Chandorkar, M. Agarwal, K. L. Chen, W. T. Park, R. Candler, G. Yama, A. Partridge, M. Lutz, and T. W. Kenny, "Using MEMS to build the device and the package," presented at Transducers & Eurosensors Lyon, France, 2007.

[47] B. Kim, M. A. Hopcroft, R. Melamud, C. M. Jha, M. Agarwal, S. A. Chandorkar and T. W. Kenny, "CMOS Compatible Wafer-Scale Encapsulation with MEMS resonators" ASME InterPACK, Vancouver, Canada, Jul 2007.

[48] B. Kim, R. N. Candler, M. Hopcroft, M. Agarwal, W.-T Park, and T. W. Kenny, “Frequency Stability of Encapsulated MEMS Resonator,” Sensors and Actuators A, 136, 125 – 131, 2007.

[49] B. Kim, R. N. Candler, M. Hopcroft, M. Agarwal, W.-T. Park, T. W. Kenny, "Frequency Stability of Wafer-Scale Encapsulated MEMS Resonators," Transducers '05, vol. 2, pp. 1965-1968, 2005.

[50] B. Kim, R. N. Candler, M. Hopcroft, M. Agarwal, W.-T Park, J. Li, and T. W. Kenny, “Investigation of MEMS Resonators Characteristics for Long-Term Operation and Wide Temperature Variation Condition,” ASME International Mechanical Engineering Congress and RD&D Expo, 2004.

[51] M. A. Hopcroft, H. K. Lee, B. Kim, R. Melamud, S. Chandorkar, M. Agarwal, C. M. Jha, J. Salvia, G. Bahl, H. Mehta, and T. W. Kenny, "A High-Stability MEMS Frequency Reference", TRANSDUCERS '07 / Eurosensors XXI, the 14th International Conference on Solid-State Sensors, Actuators and Microsystems Lyon, France, 10-14 June 2007.

[52] M. A. Hopcroft, "Silicon Micromechanical Resonators for Frequency References", Ph.D. thesis in Mechanical Engineering, Stanford University, 2007.

[53] C. T.-C. Nguyen, and R. Howe, “Microresonator frequency control and stabilization using an integrated micro oven,” in Proc. Transducers, Yokohama, Japan, pp. 1040–1043, 1993.

[54] C. T.-C. Nguyen, “Micromechanical resonators for oscillators and filters,” in Proc. IEEE Ultrason. Symp., vol. 1, pp. 489–499, 1995.

[55] M. A. Huff, S. D. Senturia, and R. T. Howe, “Thermally isolated microstructure suitable for gas sensing applications,” in Tech. Dig. IEEE Solid-State Sens., Actuator Workshop, Hilton Head, SC, pp. 47–50, Jun. 6–9, 1988.

[56] C. M. Jha, M. A. Hopcroft, S. A. Chandorkar, J. C. Salvia, M. Agarwal, R. N. Candler, R. Melamud, B. Kim, and T. W. Kenny, “Thermal Isolation of Encapsulated MEMS Resonators”, Journal of Microelectromechanical Systems, vol. 17, no. 1, Feb 2008.

[57] R. N. Candler, M. A. Hopcroft, B. Kim, W. T. Park, R. Melamud, M. Agarwal, G. Yama, A. Partridge, M. Lutz, and T. W. Kenny, “Longterm and accelerated life testing of a novel single-wafer vacuum encapsulation for MEMS

resonators," J. Microelectromech. Syst., vol. 15, no. 6, pp. 1446–1456, Dec. 2006.

[58] R. N. Candler, W.-T. Park, H. Li, G. Yama, A. Partridge, M. Lutz, and T. W. Kenny, "Single wafer encapsulation of MEMS devices," IEEE Trans. Adv. Packag., vol. 26, no. 3, pp. 227–232, Aug. 2003.

[59] M. Agarwal, "Nonlinearities and Phase Noise in Electrostatically Transduced MEMS Resonator based Oscillators", Ph.D. thesis in Electrical Engineering, Stanford University, 2007.

[60] C. Bourgeois, E. Steinsland, N. Blanc, and N. F. de Rooij, "Design of resonators for the determination of the temperature coefficients of elastic constants of monocrystalline silicon," IEEE, The International Frequency Control Symposium, 1997.

[61] J.-h. Jeong, S.-h. Chung, S.-H. Lee, and D. Kwon, "Evaluation of elastic properties and temperature effects in Si thin films using an electrostatic microresonator," Journal of Microelectromechanical Systems, vol. 12, pp. 524-530, 2003.

[62] S. Nikanorov, Y. A. Burenkov, and A. Stepanov, "Elastic Properties of Silicon," Fizika Tverdogo Tela (Soviet Physics Solid State), vol. 13, pp. 3001-4, 1971.

[63] Y. A. Burenkov, and S. Nikanorov, "Temperature dependence of the elastic constants of silicon," Fizika Tverdogo Tela (Soviet Physics Solid State), vol. 16, pp. 1496-8, 1974.

[64] R. Melamud, M. Hopcroft, C. M. Jha, B. Kim, S. Chandorkar, R. Candler, and T. W. Kenny, "Effects of Stress on the Temperature Coefficient of Frequency in Double Clamped Resonators," Transducers '05, vol. 1, pp. 392-395, 2005.

[65] J. C. Greenwood, "Silicon in mechanical sensors," Journal of Physics E: Scientific Instruments, pp. 1114-1128, 1988.

[66] K. G. Lyon, G. L. Salinger, C. A. Swenson, and G. K. White, "Linear thermal expansion measurements on silicon from 6 to 340 K," Journal of Applied Physics, vol. 48, pp. 865-868, 1977.

[67] Y. Okada, and Y. Tokumaru, "Precise determination of lattice parameter and thermal expansion coefficient of silicon between 300 and 1500 K," Journal of Applied Physics, vol. 56, pp. 314-320, 1984.

[68] M. J. Madou, Fundamentals of Microfabrication, 2nd ed. (CRC, New York, 1997), pp. 204–207.

[69] R. Melamud, B. Kim, M.A. Hopcroft, S. Chandorkar, M. Agarwal, C.M. Jha, and T.W. Kenny, "Composite Flexural-Mode Resonator with Controllable Turnover Temperature," Proceedings of International Conference on MEMS, Kobe, Japan, 2007.

[70] R. Melamud, B. Kim, S. Chandorkar, M. A. Hopcroft, M. Agarwal, C. M. Jha, and T. W. Kenny, “Temperature Compensated High Stability Silicon Resonators,” Appl. Phys. Lett. 90, 1 (2007).

[71] S. S. Schodowski, "Resonator Self-Temperature Sensing Using a Dual-Harmonic-Mode Crystal Oscillator," Proceedings of the 43rd Annual Symposium on Frequency Control (IEEE, New York, 1989).

[72] J. R. Vig, "Temperature Insensitive Dual-Mode Resonant Sensors – A Review," IEEE Sens. J. 1, 1, Jun. 2001.

[73] A. Barzilai, T. VanZandt, and T. W. Kenny, "Technique for measurement of the noise of a sensor in the presence of large background signals," Rev. Sci. Instrum. 69, 7, Jul. 1998.

[74] J. S. Bendat and A. G. Piersol, Random Data: Analysis and Measurement Procedures, 2nd ed. (Wiley, New York, 1986), pp. 117–120 and 534–536.

[75] J. S. Bendat and A. G. Piersol, Engineering Applications of Correlation and Spectral Analysis (Wiley, New York, 1980), pp. 43–48 and 154–159.

[76] D. A. Howe, D. W. Allan, and J. A. Barnes, "Properties of Signal Sources and Measurement Methods," Proceedings of the 35th Annual Symposium on Frequency Control, pp. 1–47, 1981.

[77] M. E. Frerking, Crystal Oscillator Design and Temperature Compensation, New York: Van Nostrand, 1978.

[78] F. P. Incropera and D. P. Dewitt, Fundamentals of Heat and Mass Transfer, 5th ed. New York: Wiley, 2002.

[79] M. N. Ozisik, Heat Conduction, 2nd ed. New York: Wiley, 1993.

[80] J. D. Plummer, M. Deal, and P. B. Griffin, Silicon VLSI Technology: Fundamentals, Practice, and Modeling. Englewood Cliffs, NJ: Prentice-Hall, 2000.

[81] A. D. McConnell, U. Srinivasan, and K. E. Goodson, "Thermal conductivity of doped polysilicon layers," J. Microelectromech. Syst., vol. 10, no. 3, pp. 360–369, Sep. 2001.

[82] M. Asheghi, K. Kurabayashi, R. Kasnavi, and K. E. Goodson, "Thermal conduction in doped single crystal silicon films," J. Appl. Phys., vol. 91, no. 8, pp. 5079–5088, Apr. 2002.

[83] W. G. Vincenti and C. H. Kruger, Jr., Introduction to Physical Gas Dynamics. New York: Wiley, 1975.

[84] V. Kaajakari, T. Mattila, A. Oja, and H. Seppa, "Nonlinear limits for single-crystal silicon microresonators," J. Microelectromech. Syst., vol. 13, no. 5, pp. 715–724, Oct. 2004.

[85] R. D. Blevins, Formulas for Natural Frequency and Mode Shape. Malabar, FL: Krieger, 2000.

[86] S. A. Chandorkar, H. Mehta, M. Agarwal, M. A. Hopcroft, C. M. Jha, R. N. Candler, G. Yama, G. Bahl, B. Kim, R. Melamud, K. E. Goodson, and T.W. Kenny, "Non-isothermal micromechanical resonators," in Proc. MEMS, Kobe, Japan, 2007.

[87] R. L. Filler, "The acceleration sensitivity of quartz crystal oscillators: a review," IEEE transactions on ultrasonic, ferroelectrics and frequency control, vol. 35, no.3, may 1988.

[88] A. W. Warner and W. L. Smith, "Quartz crystal units and precision oscillators for operation in severe mechanical environments," 14th Annu. Symp. Freq. Contr., 1960, pp. 200-216.

[89] W. L. Smith, “An ultra-precise standard of frequency,” Final Report, Contract DA 36-039 sc-73078, U.S. Army, 1960.

[90] W. J. Spencer and W. L. Smith, “Precision crystal frequency standards,” 15th Annu. Symp. Freq. Contr., 1961, pp. 139-155.

[91] W. L. Smith and W. J. Spencer, “Quartz crystal controlled oscillators,” Final Report, Contract DA 36-039 sc-85373, U.S. Army, 1963.

[92] D. B. Leeson, “Aerospace crystal environmental requirements,” 19th Annu. Symp. Freq. Contr., 1965, pp. 49-57.

[93] D. B. Leeson and G. F. Johnson, “Short-term stability for a Doppler radar: Requirements, measurements, and techniques,” in Proc. IEEE, 54, 1966, pp. 244-248.

[94] G. F. Johnson, “Vibration characteristics of crystal oscillators.” 21st Annu. Symp. Freq. Contr., 1967, pp. 287-293.

[95] J. Moses. “NAVSTAR global positioning system oscillator requirements for the GPS manpack,” 30th Annu. Symp. Freq. Contr., 1967, pp. 390-400.

[96] J. M. Przyjemski and P. L. Konop, “Limitations on GPS receiver performance imposed by crystal-oscillator g-sensitivity,” NAECON ’77, 1977.

[97] R. Beeson, J. J. Gagnepain, D. Janiaud, and M. Valdois, “Design of a bulk wave quartz resonator insensitive to acceleration,” Proceedings Freq. Control Symposium, 1979, p. 337.

[98] J. R. Vig, C. Audoin, L. S. Cutler, M. M. Driscoll, E. P. EerNisse, R. L. Filler, R. M. Garvey, W. J. Riley, R. C. Smythe, and R. D. Weglein, “Acceleration,

Vibration and Shock Effects – IEEE Standards Project P1193," Proceeding of the Frequency Control Symposium, 1992, p. 763.

[99] C. M. Jha, J. Salvia, S. A. Chandorkar, R. Melamud, E. Kuhl and T. W. Kenny, "Acceleration insensitive encapsulated silicon microresonator," in press APL, 2008.

[100] M. Agarwal, K. K. Park, S. A. Chandorkar, R. N. Candler, B. Kim, M. A. Hopcroft, R. Melamud, and T. W. Kenny, "Acceleration sensitivity in beam type electrostatic microresonator," APL, 90, 014103 (2007).

[101] S. D. Senturia, Microsystem Design, Kluwer academic publishers, Boston, 2001.

[102] J. P. Den Hartog, Mechanical vibrations, Dover publications, Inc. New York, 1985.

[103] M. P. Bendsoe, and O. Sigmund, Topology optimization – theory, methods and applications, Springer, New York, 2003.

[104] M. P. Bendsoe, and N. Kikuchi, "Generating optimal topologies in structural design using a homogenization method," Computers Methods in Applied Mechanics and Engineering, 71(2), 197 – 224, 1988.

[105] A. Zochowski, "The design of a two dimensional domain," J. Struct. Mech. 16, 17 – 34, 1988.

[106] M. P. Bendsoe, "Optimal shape design as a material distribution problem," Structural Optimization, 1, 193 – 202, 1989.

[107] G. I. N. Rozvany, M. Zhou, and O. Sigmund, "Topology optimization in structural design," in H. Adeli (ed.), Advances in Design Optimization, Chapman and Hall, London, chapter 10, pp. 340 – 399, 1994.

[108] R. J. Yang, and C. -H. Chuang, "Optimal topology design using linear programming," Computers and Structures, 52(2), 265 – 276, 1994.

[109] W. Prager, and J. E. Taylor, "Problems of optimal structural design," J. Applied Mechs., 35, 102 – 106, 1968.

[110] J. E. Taylor, "Maximum strength elastic structural design," Proc. ASCE, 95, 653 – 663, 1969.

[111] E. F. Masur, "Optimum stiffness and strength of elastic structures," Journal of Engineering Mechanics, 96, 621 – 640, 1970.

[112] G. D. Cheng, and N. Olhoff, "Regularized formulation for optimal design of axisymmetric plates," International Journal of Solids and Structures, 18(2), 153 – 169, 1982.

[113] G. I. N. Rozvany, and M. Zhou, "The COC algorithm part I: Cross-section optimization or sizing," Computer Methods in Applied Mechanics and Engineering, 89, 281 – 308, 1991.

[114] A. R. Diaz, and M. P. Bendsoe, "Shape optimization of structures for multiple loading situations using a homogenization method," Structural Optimization, 4, 17 – 22, 1992.

[115] Y.M.Xie, and G.P.Steven, Evolutionary structural optimization, Springer, New York 1997.

[116] G. I. N. Rozvany, Optimal design of flexural systems, Pergamon press, Oxford, 1976.

[117] G. I. N. Rozvany, Structural design via optimality criteria, Kluwer Academic Publishers Group, Dordrecht, Boston, 1989.

[118] G. I. N. Rozvany, M. P. Bendsoe, and U. Krisch, “Layout optimization of structures,” Applied Mechanics Reviews, 48(2), 41 – 119, 1995.

[119] S. J. Roundy, Energy scavenging for wireless sensor nodes with a focus on vibration to electricity conversion, Thesis, University of California, Berkeley, 2003.

[120] C. Kolle, W. Scherr, D. Hammerschmidt, G. Pichler, M. Motz, B. Schaffer, B. Forster, and U. Ausserlechner, “Ultra Low-Power Monolithically Integrated Capacitive Pressure Sensor for Tire Pressure Monitoring,” IEEE, 2004.

[121] C. M. Jha, G. Bahl, R. Melamud, S. A. Chandorkar, M. A. Hopcroft, B. Kim, M. Agarwal, J. Salvia, H. Mehta, and T. W. Kenny, “High resolution microresonator based digital temperature sensor,” APL, 91, 7, 2007.